NTNU

Norwegian University of
Science and Technology

A Simulation Study of the Barents Sea Alta Discovery

Investigation of Optimal Recovery Method

Ida Nikoline Lie Sirevaag

Petroleum Geoscience and Engineering
Submission date: June 2018
Supervisor: Jon Kleppe, IGP

Norwegian University of Science and Technology
Department of Geoscience and Petroleum

Abstract

A re-occurring topic in the petroleum industry is to enhance the oil and gas recovery while optimizing the return of investment. Decisions related to field development are critical because most of the investments are made during the stage when the uncertainties are greatest. This thesis presents an optimization analysis of different development strategies for the Alta West discovery in the Barents Sea. Three development strategies are investigated: gas injection, water injection and pressure depletion. The Alta West is an oil discovery with a significant gas cap. The oil zone is 44-meter with an underlying aquifer. The reservoir is highly heterogeneous with clastic sandstones and conglomerates.

The study is performed using the Eclipse Black Oil Simulator. The reservoir properties with inherent uncertainty are investigated. The most influential parameters for fluid production, relative to a deterministic reference case, are carried forward to an uncertainty risk analysis. The risk analysis is performed by using Monte Carlo Simulations. Each recovery method is evaluated and optimal recovery strategy is established, based on numerical simulations and other aspects of the field development process.

The most influential parameters are permeability, degree of reservoir heterogeneity and the size of the underlying aquifer. Pressure depletion is regarded as the safest choice of development strategy taking into account the great uncertainties in the Alta West discovery. Gas cap expansion is considered a dominating drive mechanism. The results demonstrate that the gas cap displacement efficiency has a potential for high oil recovery without additional water- or gas injection. However, due to lack of infrastructure in the Barents Sea, gas re-injection or gas deposition might be required.

Sammendrag

Et gjennomgående tema i petroleumsindustrien er å øke olje- og gassutvinningen samtidig som å optimalisere invisteringsavkastningene. Valg av utviklingsstrategi er avgjørende da de største invisteingene skjer i startfasen når usikkerhetene er størst. Denne oppgaven beskriver en optimaliseringsanalyse av forskjellige utvinningsstrategier for Alta Vest-funnet i Barentshavet. De tre utvinningsstrategiene som skal undersøkes er: gassinjeksjon, vanninjeksjon og trykkavlastning. Alta Vest-funnet består av en 44 meter tykk oljesone med en stor gasskappe og en underliggende akvifer. Reservoaret har stor reservoarheterogenitet og består av klastiske sandsteiner og konglomerater.

Oppgaven gjennomføres ved hjelp av Eclipse Black Oil Simulator. Reservoaregenskapene som forventes å ha stor usikkerhet skal undersøkes og egenskapene med størst innflytelse på væskeproduksjon i forhold til en deterministiske modell blir inkludert i en usikkerhetsanalyse. Usikkerhetsanalysen utføres ved hjelp av Monte Carlo simuleringer. Hver utviklingsstrategi analyseres og den optimale strategien er basert på numeriske simuleringer og andre aspekter ved utviklingsprosessen.

De mest innflytelsesrike parameterne er permeabilitet, grad av reservoarheterogenitet og størrelsen av akviferen. Så lenge det er knyttet usikkerhet til disse parameterne i Alta Vest-reservoaret, er trykkavlastning den sikreste utvinningsstrategien. En dominerende drivmekanisme er antatt å være ekspanderende kasskappe. Resultatene antyder at gasskappens fortrengningseffektivitet har et stort potensiale for å gi høy oljeutvinning uten bruk av vann- eller gassinjeksjon. På den andre siden er begrenset med infrastruktur i Barentshavet som kan medføre problemer knyttet til transport av gassproduksjon.

Preface

This Master's thesis is written at the Department of Geoscience and Petroleum (IGP) at the Norwegian University of Science and Technology (NTNU) in Trondheim. It is the final product of the MSc program in Petroleum Geosciences and Engineering, with specialization in Reservoir Engineering and Petrophysics. The thesis is written during the spring of 2018 and in cooperation with the Norwegian oil company, Lundin Norway AS.

I would like to thank Lundin for the opportunity to use their confidential data and for great guidance during the work of this thesis. A special thanks goes to Lars Sundal for his role as academic advisor, and to Paul Tijink for his insight and assistance in reservoir simulation. Further, a thank goes to Alister MacDonald and Ingrid Piene Gianotten for constructing the full-scale reservoir model used in this thesis, and to Per Øyvind Seljebotn for giving me the opportunity to write this thesis in cooperation with Lundin.

I would also like to thank my supervisor Professor Jon Kleppe for his guidance during the course of this thesis. His insight and knowledge within reservoir technology and simulation has been of great use.

Trondheim, June 2018

Ida Sirevaag

Contents

List of Figures

List of Tables

Nomenclature

Symbols

α	Dip angle
ΔP	Pressure difference
$\Delta\rho$	Density difference
λ	Power function constant for water saturation modelling
μ	Viscosity
$\overline{S}_w$	Average saturation behind the fluid front
ϕ	Porosity
ρ	density
σ	Surface tension
θ	Contact angle of the system
A	Cross sectional area
a	Power function constant for water saturation modelling
B	Formation volume factor
b	Power function constant for water saturation modelling
C_r	Pore compressibility

C_w Water compressibility

F Scaling factor

F_A Archie's formation factor

f_w Fractional flow of water

G Gravity forces

g Acceleration due to gravity

G_i Cumulative gas injected

H Height above free water level

h_c Capillary height

I Resistivity index

J Leverett j-function

k Rock permeability

k_h Horizontal permeability

$k_r^{'}$ End-point relative permeability

k_v Vertical permeability

k_{rn} Non-wetting relative permeability

k_{ro}^x Oil relative permeability at irreducible water saturation and zero gas saturation

k_{rw}^o Water relative permeability at residual oil saturation

k_r Relative permeability

L_g^o, E_g^o, T_g^o Empirical LET-parameters for gas phase with associated oil phase

L_o^g, E_o^g, T_o^g Empirical LET-parameters for oil phase with associated gas phase

L_o^w, E_o^w, T_o^w Empirical LET-parameters for oil phase with associated water phase

L_w^o, E_w^o, T_w^o Empirical LET-parameters for water phase with associated oil phase

M Mobility ratio

m Initial gas cap size

m_A Archie's cementation factor

N Original oil in place

n Archie's saturation factor and an empirical constant

N_g Corey exponent for gas

N_o Corey exponent for oil

N_p Cumulative oil produced

N_w Corey exponent for water

P Pressure

P_c Capillary pressure

P_d Displacement pressure

P_i Initial pressure

P_{cd} Drainage capillary pressure

P_{ci} Imbibition capillary pressure

P_{cw} Water capillary pressure

P_{pb} Bubble point pressure

q Volumetric flow rate

q_{inj} Volumetric injection rate

R_o Brine saturated rock resistivity

R_p Cumulative producing gas-oil ratio

R_t	Partially brine-saturated rock resistivity
R_w	Brine resistivity
R_{soi}	Initial solution gas-oil ratio
R_{so}	Solution gas-oil ratio
S	Saturation
S_{gcr}	Critical gas saturation
S_{hg}	Mercury saturation
S_{ncrd}	Drainage non-wetting critical saturation
S_{ncri}	Imbibition non-wetting critical saturation
S_{ncrt}	Non-wetting trapped critical saturation
S_{nmax}	Non-wetting maximum saturation
S_{on}	Normalized oil saturation
S_{or}	Residual oil saturation
S_{swir}	Irreducible water saturation
S_{wcr}	Critical water saturation
S_{wf}	Water saturation at the front at water breakthrough
S_{why}	Water saturation at the hysteresis reversal point
S_{wi}	Initial water saturation
S_{wma}	Maximum attainable water saturation
S_{wn}	Normalized water saturation
t	time
U	Constant in J-leverett function

v Velocity

W_e Cumulative aquifer influx

W_i Cumulative water injected

W_p Cumulative water produced

x_f Postion of the fluid front

Subscripts

i, j, k Directions

o, g, w oil, gas, water

x, y, z Dimensions

Abbreviations

BHP Bottom Hole Pressure

CCA Conventional Core Analysis

DST Drill Stem Test

FWL Free Water Level

GOC Gas-Oil Contact

GOR Gas-Oil Ratio

LWD Logging While Drilling

MD_RKB Measured Depth below Rotary Kelly Bushing

MDT Modular Formation Dynamics Tester

MWD Measurements While Drilling

OWC Oil-Water Contact

REF Reference Case

RF Recovery Factor

$SCAL$ Special Core Analysis

SEM Scanning Electron Microscope

$STOOIP$ Stock Tank Oil Originally In Place

TVD True Vertical Depth

WC Water-Cut

Chapter 1

Introduction

In 2014, Lundin Norway AS proved oil in the Alta exploration project located on the southern part of the Loppa High Structure in the Barents Sea (Figure 1.2). The discovery is divided into an eastern flank dominated by carbonate rocks, and a western flank dominated by siliclastic sands and conglomerates. The eastern flank has the greatest potential for creating positive return on investment of the Alta project. Bjerga (2017) studied the reservoir mechanisms in the eastern flank reservoir in her master thesis. The conclusion for optimal recovery strategy for the eastern flank is gas injection.

In this thesis, reservoir simulations have been used to investigate reservoir behavior and optimization of different development strategies. Several modifications affecting the sensitivity for a clastic oil reservoir are studied including operational sensitivities, rock- and fluid properties.

Three development strategies are studied; gas injection, water injection and pressure depletion. The motivation is to detect the dominating drive mechanisms in the reservoir and investigate the parameters most critical for fluid production. An uncertainty risk analysis performed by using Monte Carlo Simulations are conducted to give a recommendation of optimal recovery method. Other aspects of the field development process related to water handling and gas handling are also discussed.

The reservoir studied in this thesis is the Alta West reservoir. The geology is complex and the depositional environment of the reservoir rocks is not fully understood. One exploration well has been drilled in Alta West. A drill stem test was planned, but not succeeded due to tight reservoir rocks. A sidetrack well was drilled, and a successful drill stem test was performed. The reservoir quality was poor to moderate.

The beginning of this thesis introduces the Alta West Discovery, followed by a literature study on basic reservoir properties and the processes affecting oil recovery. Chapter 3 is a technical description of Eclipse reservoir modeling, including the specific functions and techniques related to the work of this thesis. Chapter 4 describes the Alta reservoir simulation model where the Black Oil simulator (Eclipse 100) is used to run the simulations. The simulation model is a full-scale section of Lundin's Alta model. The results from the sensitivity study and the uncertainty risk analysis are summarized in Chapter 5, followed by a discussion and a conclusions.

1.1 The Alta Discovery

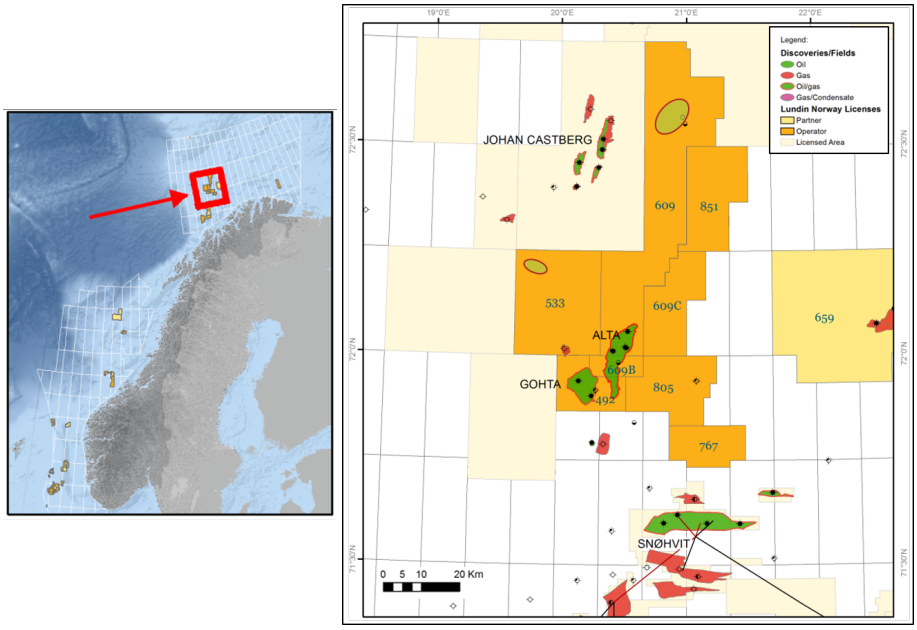

Figure 1.1: Location of the Alta Discovery.

The Alta Discovery is located on the southern part of the Loppa High in the Barents Sea. It is approximately 200 km north-west of Hammerfest, 60 km south of the Johan Castberg Field and 20 km northeast of the Gotha Discovery. Figure 1.1 shows the location of the discovery. The discovery was made by well 7220/11-1 in September 2014 in production license PL609. Since then, Six additional appraisal wells (including three sidetracks) have been drilled.

Figure 1.2 shows the Loppa High structure. The Alta discovery, marked on the southern part of the structure, is a four-way dip closure on the Basal Triassic unconformity. An east-west dip closure of the structure with its main reservoir units and fluid contacts is shown in Figure 1.3. The main reservoirs include both Palaeozoic carbonates and basal Triassic clastics. The structure is divided into Alta East Flank and Alta West Flank. The East Flank are carbonate reservoirs and belong to the Ørn and Falk formations while

the West Flank consist of mainly the Triassic clastic reservoirs including both dolomitic and siliclastic sands and conglomerates.

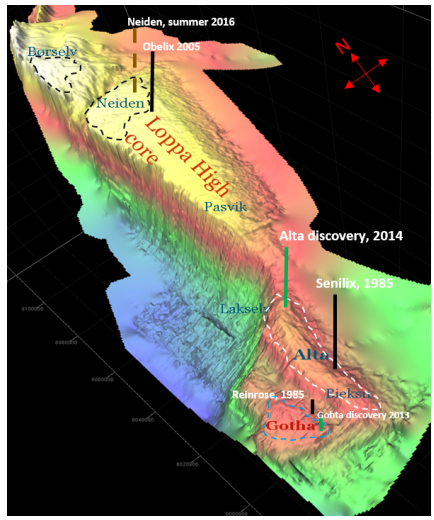

Figure 1.2: The Loppa High structure illustrating the location of the Alta discovery.

The area of the Alta field extends approximately 5 km from east to west and 20 km from south to north. It has a 44-meter tick oil column, a large aquifer and a significant gas-cap. The 5 reservoir penetrations drilled on the East Flank have good pressure communication with the same fluid contacts. The gas-oil contact (GOC) is estimated at 1880 mTVD and the free water level (FWL) at 1924 mTVD. The East Flank reservoirs are classified as high quality reservoirs. The exploration well with one sidetrack drilled on the West Flank is classified as poor quality reservoirs and the pressure communication with the other wells is limited due to the poor reservoir quality. However, pressure measurements indicate common fluid contacts.

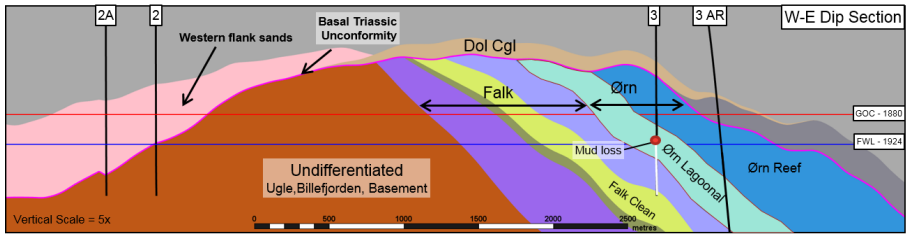

Figure 1.3: East-west dip section of Alta East and Alta West including main reservoir units and fluid contacts.

1.2 Alta West

In 2015, the exploration well, 7220/11-2, with sidetrack, 7220/11-2A, was drilled to investigate reservoir quality and confirm the presence of an oil leg on the western flank of the Alta structure. See Figure 1.4 for well location. The exploration well encountered a 50-meter gas column in reservoir rocks and a tight oil section while the sidetrack encountered both oil and gas in reservoir rocks. The name of the exploration well and the sidetrack are characterized as well 2 and sidetrack 2A in this thesis. A total of 10 conventional cores were cut to analyze the geology and determine reservoir properties of the West Flank.

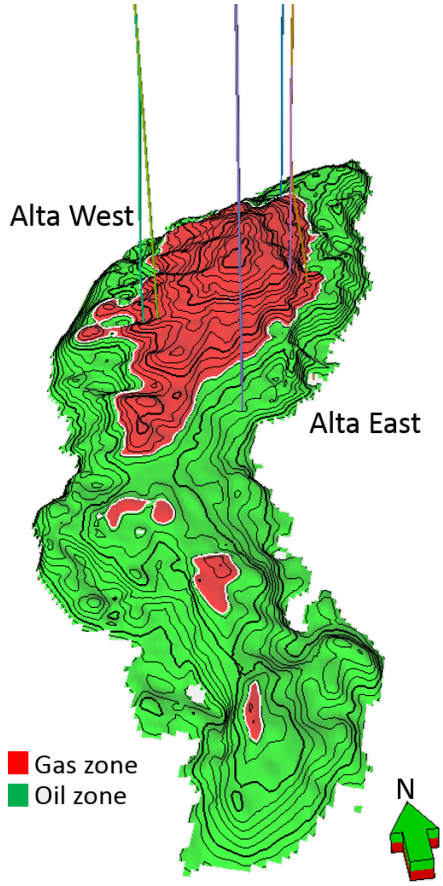

Figure 1.4: Full-field illustration of the Alta structure including the locations of the exploration wells. The gas-cap is red and the oil phase is green.

Geology

The geology of Alta West is highly complex and difficult to interpret. The West Sands are clearly shallow marine, but there are great uncertainties related to the depositional environment. Two possible interpretations are a fan delta or a tide influenced shelf.

Figure 1.5 presents a large-scale subdivision of the entire reservoir section including the overlaying Kobbe formation and underlying Basement. In the middle of the figure is the interpreted subdivision of the Alta West, supported by well logs from well 2 (right side) and sidetrack 2A (left side). They are penetrated 340 meters apart and there are significant lateral changes within the short distance. A distinct alternation is the tight shale and silt that is present in sidetrack 2A, but absent in well 2. The reservoir rocks are divided into West Sand Upper and West Sand Lower. The division is derived from differences in mineralogy, indicating that the rocks was formed by deposition of different source rocks.

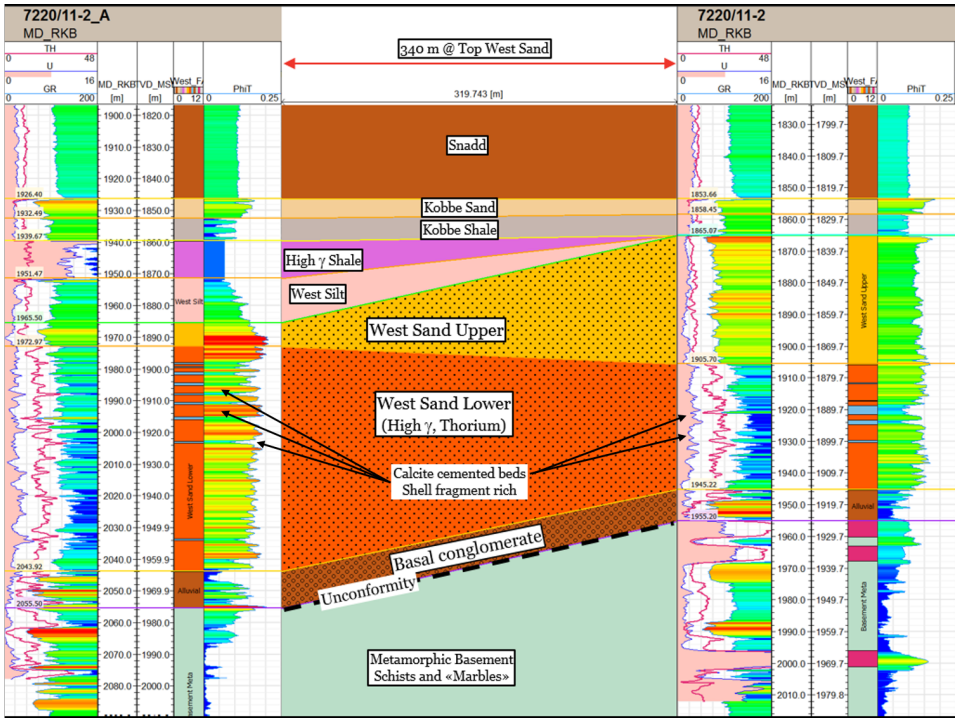

Figure 1.5: Large-scale subdivision of the Alta West.

West Sand Upper

The West Sand Upper consists of fine-grained sandstone and conglomerates. The sedimentary fragments are mainly dolostone grains, indicating that carbonate rocks dominated the source area. A significant proportion of these dolostone grains is likely to have been dissolved, creating secondary pores that have been refilled with dolomite cement. The high content of dolostone grains and dolomite cement is consistent with the low gamma ray from the gamma ray logs (first column in well logs in Figure 1.5).

Figure 1.6 illustrates two core photos from the same reservoir interval from well 2. The core interval is cut from 1889-1894 meter (MD-RKB). This interval corresponds to the middle part of the West Sand Upper (the location can be found in depth log (MD-RKB) in Figure 1.5). Figure 1.6a represents a core photo with white light, and Figure 1.6b represents a core photo with ultraviolet (UV) light. UV light is used to trigger minerals with fluorescence. Fluorescence is known as when a small amount of energy is released in the form of light (King, 2018).

The color change of fluorescent minerals can be used to interpret the mineralogy of different rocks, but it is often difficult to recognize the distinct minerals. However, the small white grains in the conglomeratic layers in Figure 1.6b are likely to be dolostone/dolomite. The layers without white grains are fine-grained sandstone. This trend follows throughout the entire section of West Sand Upper and the core photos clearly illustrate that the reservoir is shifting from fine-grained sandstone to conglomerates.

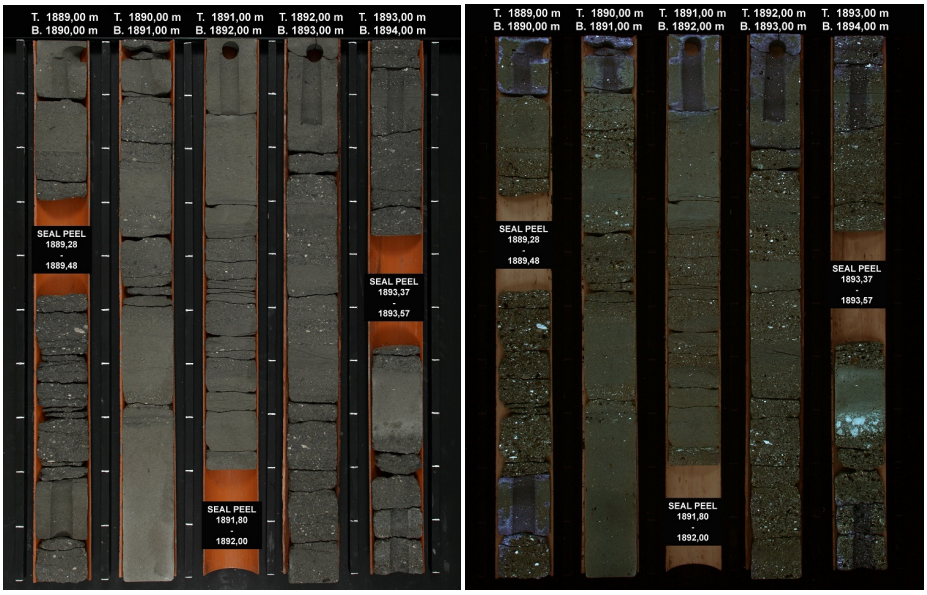

(a) White light (b) Ultraviolet (UV) light

Figure 1.6: Core photos of West Sand Upper. Cored in well 2.

West Sand Lower

West Sand Lower consists of fine-grained sandstones and conglomerates with interbedded calcite cemented layers. Figure 1.7 is a core photo interval from 1917-1922 meter (MD-RKB) illustrating the typical structure of the Alta West Lower. The interval represents the tight oil section that was penetrated in well 2. Hydrocarbons show different color in UV light and causes the shiny layers in Figure 1.7b. A layer in the middle of interval 1919-1920 meter in Figure 1.7a is a typical calcite cemented layer. It is difficult to identify the layer with white light, but easy to detect with UV light by its dark color. The dark color is due to less hydrocarbons caused by the high content of cement resulting in almost impermeable conditions.

Compared to West Sand Upper, Lower has more metamorphic minerals and weathered feldspar, suggesting a source area that includes crystalline and volcanic basement rocks. Whereas thorium is absent in the West Sand Upper, Lower contains this radioactive mineral, resulting in a sudden increase in gamma ray from West Sand Upper to Lower.

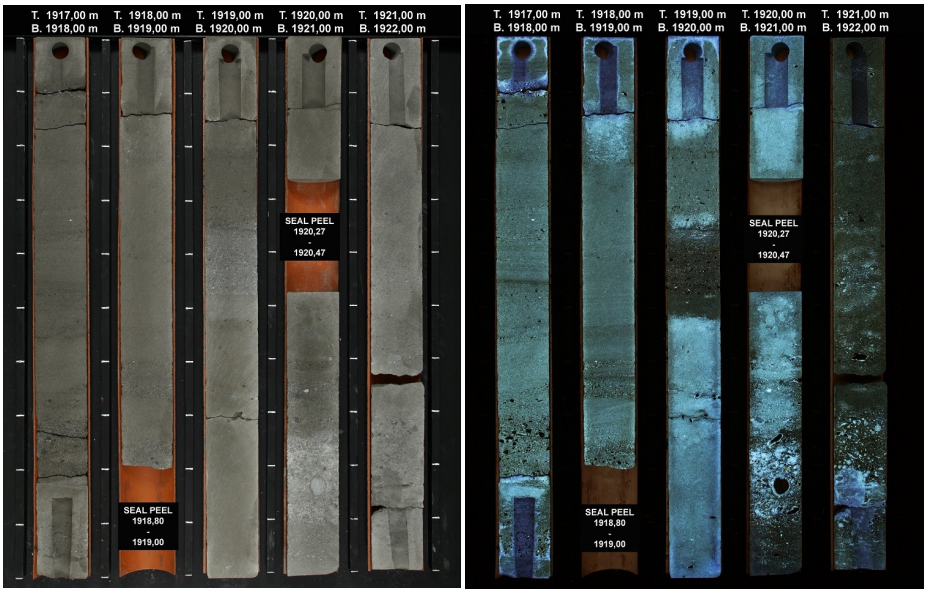

(a) Wight light (b) Ultraviolet (UV) light

Figure 1.7: Core photos of West Sand Lower. Cored in well 2.

Reservoir Properties and Quality

An extensive logging acquisition program was performed in well 2 and sidetrack 2A. It included measurements while drilling (MWD)/logging while drilling (LWD), wireline logging, conventional coring and fluid sampling. In addition, a production drill stem test (DST) was performed in sidetrack 2A. Conventional core analysis (CCA) studies have also been performed. However, special core analysis (SCAL) are not yet available.

Reservoir quality of the West Sands is poor to moderate at its best. The best reservoir interval has an average permeability of 22.1 mD and porosity of 18 % measured by CCA. CCA and DST data together with well logs are shown in Figure 1.9. The blue dots are CCA data for permeability and porosity. The light red line in column two from right is the DST interval with permeability interpretation of 10 mD. The dark red line is the CCA interval average permeability. The best interval are marked as a yellow box, indicating that the best reservoir zone contains West Sand Upper and the upper part of West Sand Lower.

However, Figure 1.9 does not illustrate data from the Modular Formation Dynamics Tester (MDT). The MDT wireline tool can measure accurate real-time pressure and vertical and horizontal permeability by collecting several fluid samples from one single wireline run. The tester makes real-time flow-line resistivity measurements at the probe module to discriminate between formation fluids and filtrate from water- and oil-based mud (Schlumberger, 2018a). The MDT test from well 2 measured permeability of 10 mD over the best interval and mostly tight or under 1 mD in the lower intervals. The MDT, CCA and DST data are generally consistent.

Figure 1.8 summarizes the porosity-permeability plot from core plug measurements. Both CCA and Amott tests were conducted. The CCA tests are brutal core "dried" tests and may give optimistic permeability measurements as it may damage small pore-filling particles. The Amott core tests are more gentle and may provide more realistic measurements. There is a wide range of permeability over the porosity interval. However, it is believed that the very low measurements, ranging from approximately 0.15-0.25 % and 0.01-0.1 mD, are special exceptions and not representative for the reservoir.

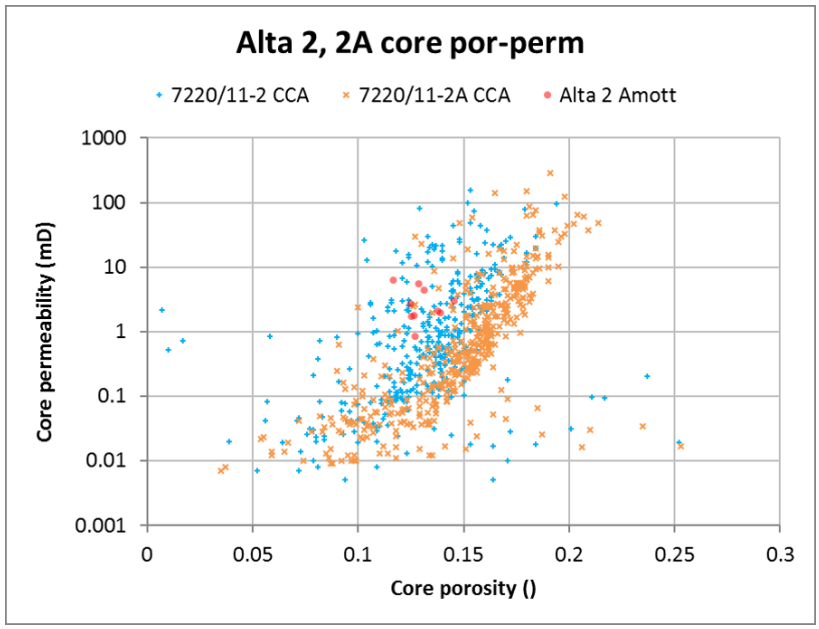

Figure 1.8: porosity-permeability plot from CCA and Amott tests from well 2 and 2A.

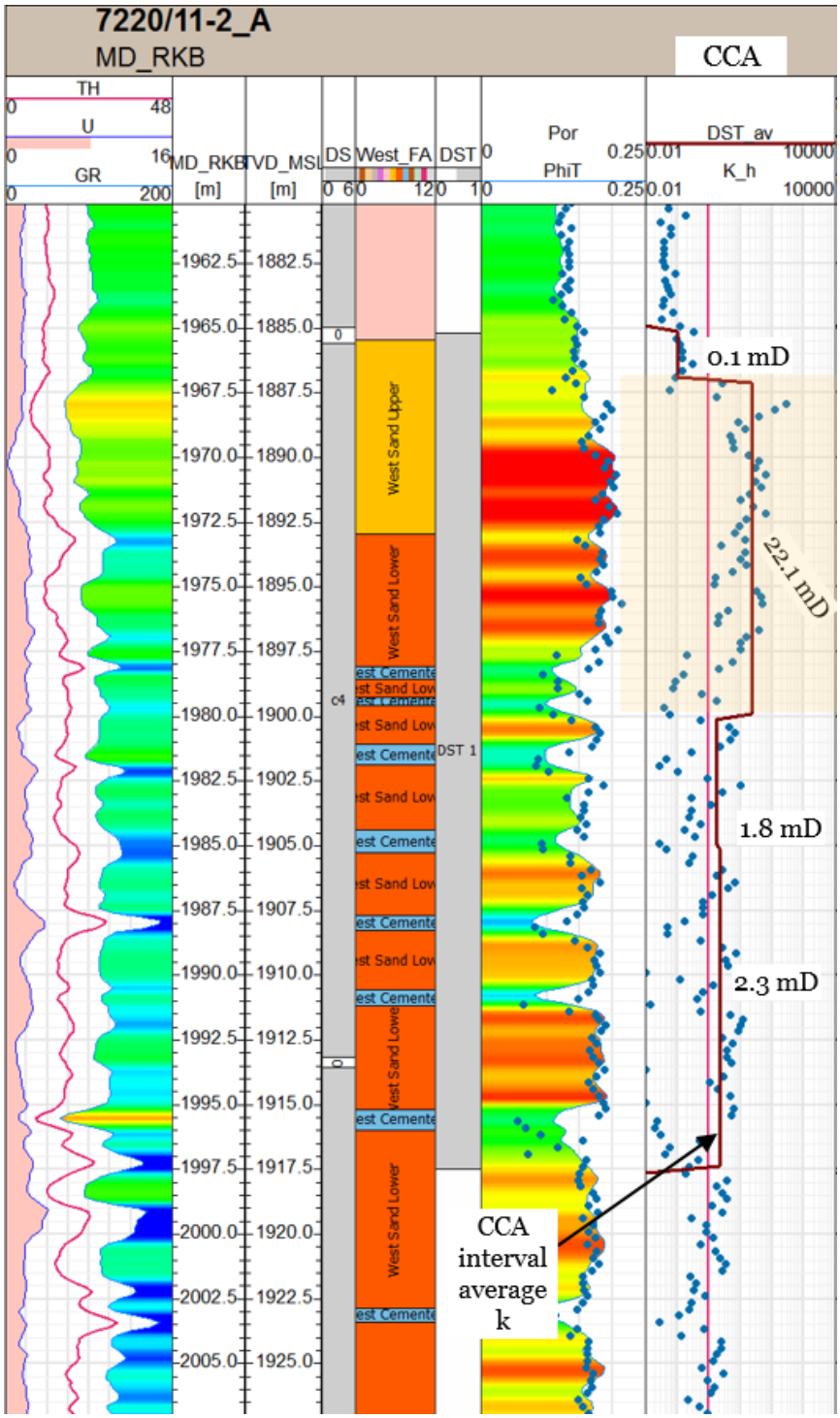

Figure 1.9: Well logs, DST and CCA data from sidetrack 2A illustrating permeability consistency.

Well 2 has slightly higher permeability than sidetrack 2A, which contains a greater interval of West Sands Lower. It is believed that the low permeability are partly because of the interbedded calcite cemented layers. Figure 1.10 illustrates the detrimental effects of a calcite cemented layer. It is a core photo from reservoir interval 1997-1998 m from sidetrack 2A. Figure 1.10a is with white light, and Figure 1.10b is with UV-light. Core plugs and thin sections are cut from the top of both columns. The core plug interval in the first column contains 20.5% cement where 16.6% are dolomite. The measured permeability is 5 mD and the porosity is 18.2%. In contrast, the core plug interval in the second column contains 50 % cement where 46% is calcite. The measured permeability is 0.36 mD and porosity is 12.1%. Due to frequently observed cemented layers is it reasonable to believe that permeability variation is a function of cementation and insignificant dependent on grain size.

(a) White light

(b) Ultraviolet (UV) light

Figure 1.10: Dolomite (first column) and calcite (second column) intervals from West Sand Lower reservoir rock in sidetrack 2A.

Another contributing factor to low permeability in the West Sand Lower can be due to the minor discrete fibrous illite that has been formed within the pores. Fibrous illite has high surface area, a pore-bridging texture, and significant microporosity. Because fibrous illite tend to grow as independent strands that extend far into the pore space they increase the flow-path tortuosity and can reduce permeability. (Lander and Bonnell, 2010). It can be difficult to determine its influence on permeability because fibrous illite has insignificant or minor impact on porosity and can be damaged after the core plugs are dried and prepared for permeability measurements.

Figure 1.11 shows two scanning electron microscope (SEM) images from the West Sand Lower. The first image shows the crystalline structure of one single pore, and the second image is a close-up image of the same pore, demonstrating how fibrous strands occupy the pore space.

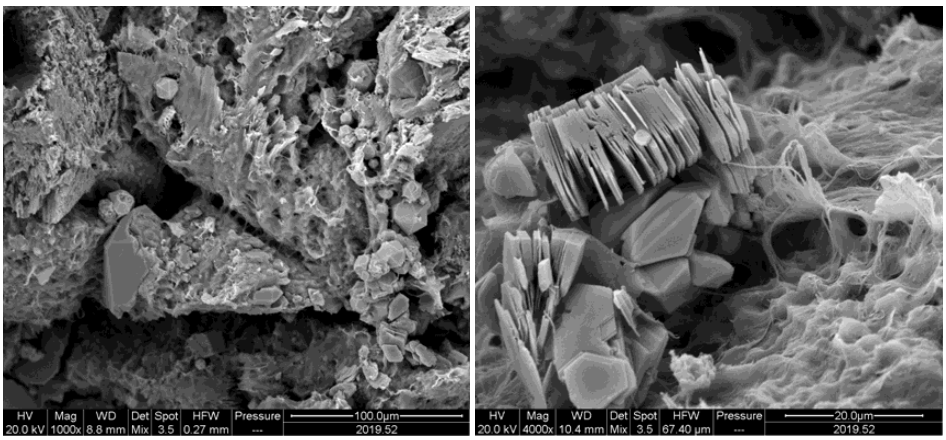

Figure 1.11: Scanning electron microscope (SEM) images. Pore-scale of the Lower West Sands illustrating fibrous illite.

Illite generally develops at temperatures above 120°C (Lander and Bonnell, 2010). The temperature of the Alta West reservoir is approximately 73°C, which is too low for fibrous illite to grow. However, the maximum burial depths in the Barents Sea are often greater than the present burial depth and the presence of minor fibrous illite is therefore not unexpected (Henriksen et al., 2011). Dolomite, which is present in the West Sand

Upper, prevents the formation of fibrous illite. A combination of thorium, kaolinite and feldspar, which is found in the West Sand Lower, may provide formation of fibrous illite.

The log-log plot of pressure vs time (Figure 1.12) from DST test performed in sidetrack 2A may provide promising data for reservoir potential. The pre acid permeability thickness, Kh, was estimated to 160 mDm. With a perforated interval of 32 meters, the average permeability becomes 5 mD. At the end of build-up, the derivative extrapolates to a lower level and the Kh increases to 280 mDm. The post acid derivative also decreases at end of build-up with a resulting Kh of 350 mDm. The high Kh are possibly effects from acidizing. However, the fact that both derivatives decreases with time may indicate better permeability away from wellbore.

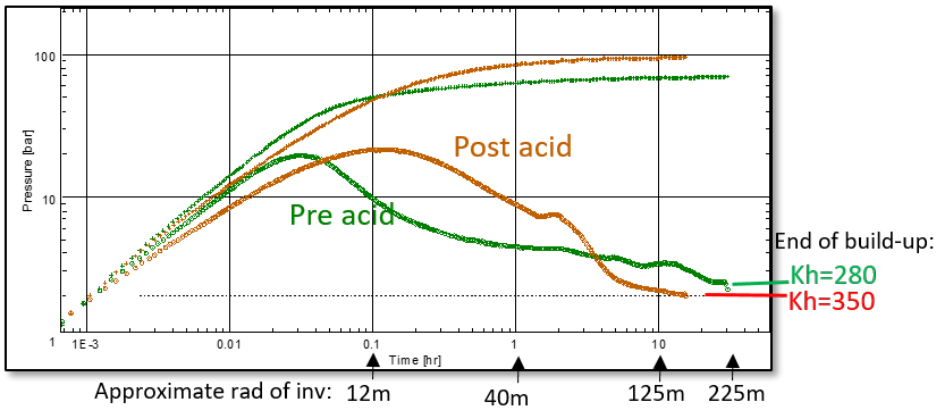

Figure 1.12: Log-log plot of pressure vs time. Pressure build-up data from drill stem test performed in sidetrack 2A.

Chapter 2

Fundamental Theory of Clastic Reservoirs With Saturated Oil

Clastic sedimentary rocks are mainly classified by grain type and grain size. They are formed by weathering of pre-existing rocks and the depositional environment commonly controls the resulting pore structure. Saturated oil reservoirs have reservoir pressure above bubble point pressure and an initial gas-cap above the oil zone.

In this chapter, the fundamental theory of a clastic oil reservoir will be described. It includes basic reservoir properties such as capillary pressure, relative permeability and wettability, followed by typical primary drive mechanisms of a saturated oil reservoir. Finally, characteristics of saturation function models and fluid displacement methods will be discussed.

2.1 Basic Reservoir Properties

It is highly important for a reservoir engineer to have knowledge about the essential reservoir properties and their influence on original oil in place and production performance. Saturation dependent functions such as the relative permeability and the capillary pressure are key factors for prediction of oil production. Misinterpretations of such properties can be detrimental for the project's economy.

2.1.1 Capillary Pressure

Capillary pressures (P_c) determine the saturation distribution in a reservoir, and hence the total in-situ volumes of oil, gas and water. Exact estimates of the capillary pressure distribution is essential in the calculations of hydrocarbon reserves. The size of the capillary pressure in a reservoir is dependent on rock texture, wettability, fluid properties, and formation saturation history. Since heterogeneity has a great impact on capillary pressure, the process of up-scaling from core-scale laboratory measurements must be carefully considered to better understand the reservoir fluid distribution (McPhee et al., 2015).

Capillary pressure is defined as the pressure difference between the non-wetting phase and the wetting phase as a function of the wetting-phase saturation. Figure 2.1b illustrates the fluid distribution in a homogeneous water-wet reservoir. There are three zones with respect to the pore fluids (Schön, 2015):

1. Water zone with 100% water saturation.
2. Transition zone with changing saturations
3. Above transition zone with irreducible (immobile) water saturation

Note that 100 % water saturation is above free water level at the displacement pressure (P_d). Displacement pressure is the minimum pressure required for the non-wetting fluid to displace the wetting fluid and enter the largest pores.

The saturation distribution vs height above free water level is best explained through the surfaces in a capillary tube. Figure 2.1a illustrates the concept of a capillary tube, which is designed to represent pore throats in a porous formation. The fluids are in equilibrium between gravity forces and capillary forces. At the fluid-solid interface, a surface tension causes water to rise in the tube (Schön, 2015). The capillary height (h_c) is hence a function of the density difference and the balance of capillary and gravity forces. In equilibrium, the capillary pressure in a porous media is:

$$P_c = \Delta\rho \cdot g \cdot h_c$$

where

$\Delta\rho$ = fluid density difference

g = acceleration due to gravity

h_c = capillary height

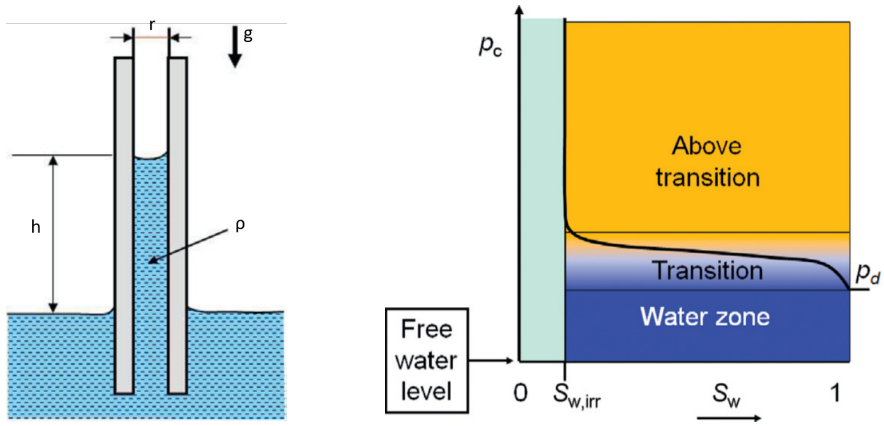

(a) Capillary tube

(b) Capillary pressure vs water saturation

Figure 2.1: Capillary tube used to calculate capillary pressure (left). Capillary pressure above free water level vs water saturation (right). Figure from Schön (2015)

The saturation for capillary pressures of equal magnitude depends on saturation history, or the direction of the saturation (McPhee et al., 2015). There are two directions of saturation change: 1) Increasing non-wetting saturation known as drainage. It is displacement of a wetting phase by a non-wetting phase. 2) Decreasing non-wetting phase known as imbibition. It is the displacement of a non-wetting phase by a wetting phase.

Figure 2.2 illustrates drainage and imbibition capillary pressure cycles for a water wet rock. The primary drainage curve refers to the migration of oil where the rock is 100 % water saturated prior to oil migration. The pressure between the oil and water phase must exceed the required displacement pressure for the oil to displace the in-situ water to irreducible water saturation (S_{wirr}). When production starts and if the rock is exposed to water at S_{wir}, it will be spontaneously imbibed and water saturation will increase until zero capillary pressure is reached. The saturation at zero capillary pressure is referred to non-wetting hydrocarbon phase saturation ($S_{p_{n-w}}$) in Figure 2.2. For the water to displace oil to residual oil saturation ($S_{r_{n-w}}$) pressure must be applied to the water phase. This process is called forced imbibition (McPhee et al., 2015).

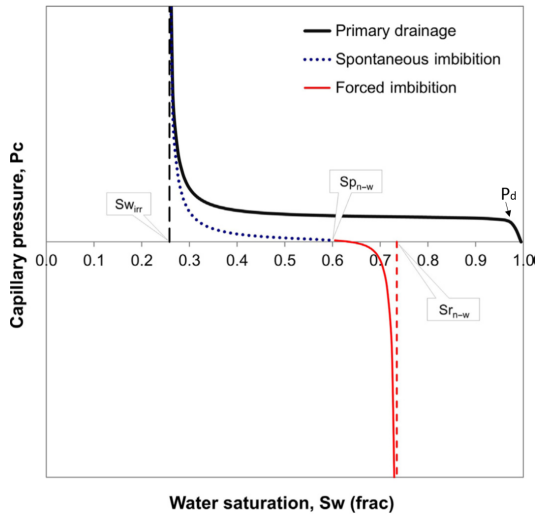

Figure 2.2: Primary drainage and imbibition capillary pressure curves for a water wet rock. Figure from McPhee et al. (2015).

2.1.2 Wettability

Wettability describes the preference of a solid to be in contact with one fluid rather than another. It influences the hydrocarbon reservoir behavior, productivity and oil recovery. Water and gas injection are frequently used to displace oil and when multiple phases are flowing in the reservoir, understanding wettability becomes highly important. Failure to understand wettability and its complications can be damaging for the

project economics (Abdallah et al., 2007).

There are several indicators and measurements to determine the wettability of a reservoir rock. Two frequently used laboratory wettability tests is known as the Amott test and the USBM index. The purpose of these tests is to reestablish the in-situ wettability by core samples. However, it must be mentioned that the methods are time consuming and expensive and may not be prioritized (McPhee et al., 2015).

Wettability methods usually involve measurements of the contact angle between a solid and a fluid. Figure 2.3 illustrates an oil drop surrounded by water on a rock surface. When the contact angle is small ($\ll 90°$) the oil forms a bead and corresponds to a water-wet surface. When the contact angle is large ($\gg 90°$), the drop spreads and the surface is characterized as oil-wet. If the surface is neither strongly water-wet or strongly oil-wet, the condition is an intermediate-wet surface where the contact angle is $\sim 90°$(Yuan and Lee, 2013). Some reservoirs have a mixed-wetting due to a variety of minerals. For example, clean sandstones tend to be more water-wet while carbonates tend to be more oil wet (Abdallah et al., 2007).

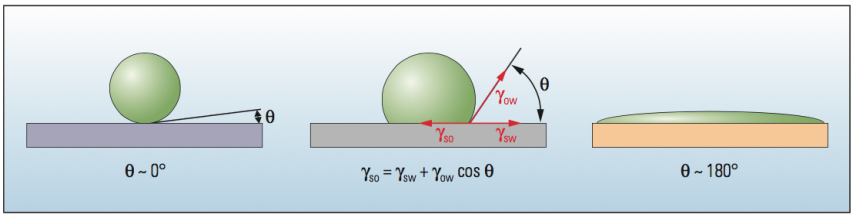

Figure 2.3: Contact angle measurement by oil drop in water phase. Left to right shows typical water-wet, intermediate-wet and oil-wet surfaces. γ is interfacial tension between oil and water, and θ is the measured contact angle. Figure from Abdallah et al. (2007)

Wettability depends on saturation history. Multiple phases of oil migration, leakage of oil and development of gas-cap are processes that can change the in-situ saturation distribution, and hence alter the wettability.

Generally, most reservoirs are water-wet prior to oil migration. These reservoirs are characterized by a long transition zone. Figure 2.4 (left) illustrates a typical transition

zone for a homogeneous water-wet reservoir. The saturation distribution along the transition zone are divided into oil and irreducible water saturation at the top of the reservoir with gradually increasing water saturation until 100 % water is reached at the bottom. In an oil-wet reservoir, the transition zone is much shorter, as illustrated to the right in Figure 2.4.

A water-wet reservoir has the oil-water contact (OWC) above free water level (FWL), indicating that pressure must be applied to force oil into the largest pores. In contrast, in an oil-wet reservoir, the OWC are below FWL, which indicates that pressure must be applied to force water into the largest pores. The capillary tubes in Figure 2.4 illustrates the two scenarios. In the capillary tube with water-wet surface, water-wetting surface forces cause water to rise and displaces oil. In the capillary tube with oil-wet surface, oil will push the water down. (Abdallah et al., 2007).

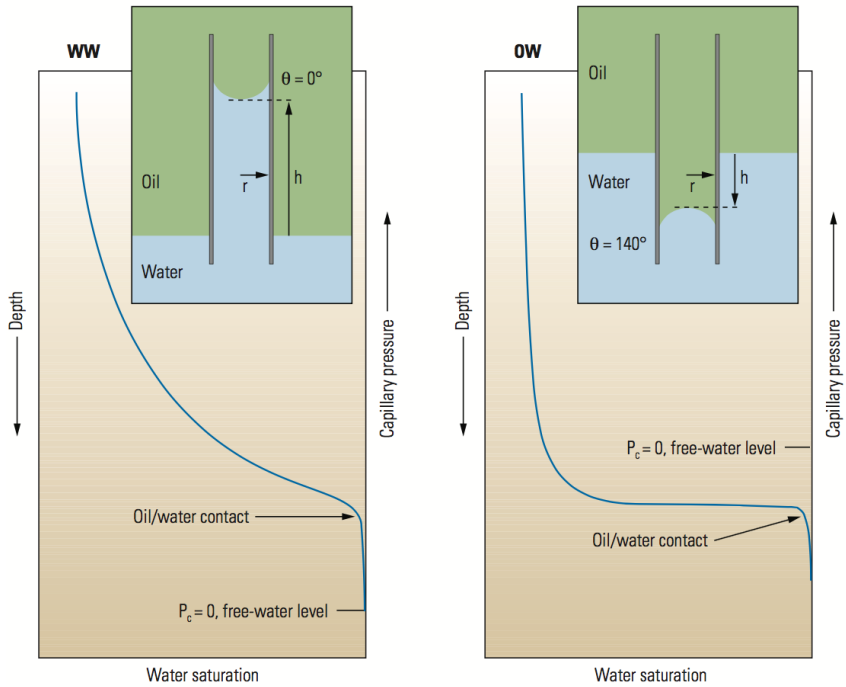

Figure 2.4: Capillary pressure curves illustrating the transition zone for a homogeneous water-wet reservoir (left) and oil-wet reservoir (right). In a capillary tube, water-wetting surface forces cause water to rise (left), displacing oil. If the tube inner surface is oil-wetting, the oil will push water down (right). h describes the height of the capillary rise (hc). Figure from Abdallah et al. (2007).

Wettability Alterations

The wettability can vary with depth along the transition zone. In the upper part of the oil column, the buoyancy of oil in water provides greater capillary pressure and forces water out of the larger pores. The wettability of the reservoir can vary from water-wetting preference at the bottom to more oil-wet at the top (Abdallah et al., 2007). At the top of the oil column where the capillary pressure is greatest, the water film along the surface becomes thinner. If surface-active component is present in the oil phase, the component can destabilize the water film and contact the surface (Abdallah et al., 2007).

For this reason, oil composition is crucial to change the wettability of an initially water-wet reservoir. Asphaltenes include the heaviest and the most polar components in crude oil and are the components with greatest influence on wettability. The effects of the asphaltenes on wettability are complex and is strongly dependent on the environment in the reservoir (Buckley, 1998).

Wettability Dependent Petrophysical Logs

Understanding the wetting condition at an early stage is crucial for selecting best development strategy. Fortunately, some petrophysical logging tools can provide fast and inexpensive wettability indications. Logging while drilling (LWD) and wireline logging provide continuous logs along the entire reservoir section and consequently bring information of mixed wettability in cases of inhomogeneous reservoirs.

Resistivity logs are useful tools for saturation determination. Brine is the only conductive fluid in a porous medium while mineral grains and hydrocarbons are non-conductive. The contrast between the conductivity (or resistivity) in a water bearing formation and an oil bearing formation followed by Archie's equation is the basis for a resistivity log interpretation (Dunlap et al., 1991). Archie's Equation can be written as:

$$F_A = \frac{R_o}{R_w} = \frac{a}{\phi^{m_A}}$$

and

$$I = \frac{R_t}{R_o} = S_w^{-n}$$

where

F_A = formation factor

R_o = resistivity of the brine saturated rock

R_w = resistivity of the brine

I = resistivity index

R_t = resistivity of the partially brine-saturated rock

m_A = cementation factor

n = saturation factor and an empirical constant

ϕ = porosity

The saturation factor must be determined from laboratory core experiments and is controlled by the brine distribution in the pore space. In a water-wet rock, water adheres to the rock surface and form a continuous phase in the rock. Many water-wet sandstone reservoirs have a saturation factor range between 1.8 and 2. In oil-wet rocks, the non-conductive oil is the continuous phase and water are located in the smaller pores as isolated droplets. The resistivity is therefore higher in an oil-wet rock and the saturation factor becomes higher than 2. However, even though the value of the n factor provide information about the wetting preference of the reservoir rock, Archie's equation is dependent on several factors, including rock texture and saturation history. The value of the n factor is therefore only an indication of the wettability (Dunlap et al., 1991).

2.1.3 Permeability

Permeability is a rock's ability to transmit fluids and it connects the fluid flow rate with the applied pressure gradient and the fluid viscosity. Once pressure is applied to a porous media, fluid will start to flow (Schön, 2015). Permeability is divided in 3 terms, depending on the fluids present in the rock:

1. Absolute permeability

2. Effective permeability

3. Relative permeability

Effective permeability describes the flow of one fluid in the presence of another fluid when the fluids are immiscible (Schön, 2015). Effective permeability is not included in the sensitivity analysis in this thesis and will not be discussed any further.

Absolute Permeability

There are different methods to determine absolute permeability. Some frequently measurements at an early stage are direct drill stem tests and a number of wireline logs. However, permeability determination is difficult and often inaccurate. The most reliable methods are laboratory core flooding experiments. The calculations from the core flooding experiments are based on Darcy's law:

$$q = \frac{kA}{\mu}\frac{dp}{dx} \tag{2.1}$$

where
q = volumetric flow rate
k = rock permeability
A = cross sectional area of the core plug
μ = fluid viscosity
dp = pressure gradient
dx = length of core plug

The different core samples require a specific preparation dependent on the type of core experiment. All core plugs need to be cleaned and dried to remove native oil, mud filtrates, evaporated salts and connate water. Some of the core cleaning and drying methods are more damaging to the core plugs. As a result, some in-situ reservoir properties may alter during preparations and result in misinterpretation of reservoir properties (McPhee et al., 2015). Therefore, the method used to clean and dry the core plug must be carefully considered when analyzing core properties.

Textural Properties Affecting Permeability

The textural properties controlling absolute permeability is porosity, pore size/grain size, pore shape, tortuosity and pore-throat to pore-body ratio (Schön, 2015). However, porosity and pore size have the greatest influence on permeability. Graphically plots of permeability vs. porosity and permeability vs. grain size are usually strongly correlated.

Figure 2.5 is a semi-log plot of permeability vs. porosity together with a linear plot of permeability vs. grain size. The plots illustrate that permeability is strongly dependent on both porosity and grain size. The plots are helpful tools to generate derivation of regression equations, which is often used to implement permeability in reservoir simulation (Schön, 2015).

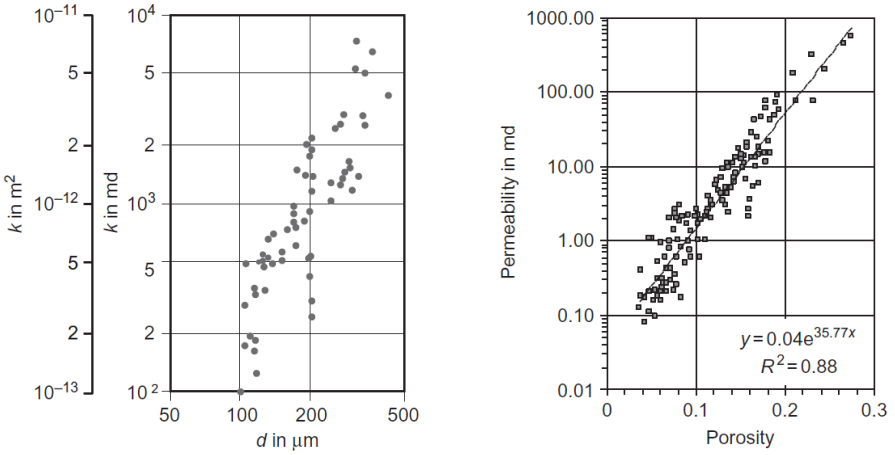

(a) Permeability vs. grain size

(b) Permeability vs. porosity

Figure 2.5: Plot of permeability vs. grain size (left) and permeability vs. porosity (right), illustrating permeability dependency. Figure from Schön (2015).

k_v/k_h-ratio

Permeability are directional dependent and its influence on field performance is important to consider in reservoir simulation. For sedimentary rocks, the ratio of vertical permeability to horizontal permeability (k_v/k_h) is usually defined. Vertical permeability is flow perpendicular to lamination while horizontal permeability is flow parallel to lamination (Schön, 2015).

Variations in permeability in different layers or directions is known as anisotropic permeability and is caused by sedimentation. Finely laminated reservoirs, with alternating change of permeability between coarse and fine sand layers, cause great anisotropy. The difference between k_h and k_v can be extreme if the reservoir has laminated shaly sands. Shale has very low permeability and can act as impermeable layers (Schön, 2015). Therefore, in reservoirs with high shale content, the effect of shale must be considered in oil recovery estimations.

Photos of core plugs provide good information about shale content and lamination and is a useful tool for k_v/k_h-ratio predictions (Schön, 2015). On the other hand, predictions from core plugs may result in misinterpretations since anisotropy may alter with scale. Figure 2.6 illustrates the anisotropy dependency on scale. It shows how a single crystal can have an anisotropic structure, but a rock formed from randomly packed crystals, like a cure plug, can be isotropic. At lager scales, a reservoir with isotropic layers may be anisotropic (Ayan et al., 1994).

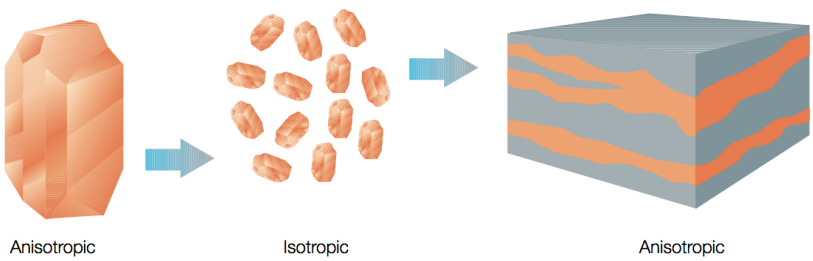

Figure 2.6: Anisotropy dependency on scale. Crystals can have an anisotropic structure, but a rock formed from randomly packed crystals can be isotropic. At lager scales, a reservoir with isotropic layers may be anisotropic. Figure from Ayan et al. (1994).

Permeability anisotropy affects the development strategy and the decision whether to drill vertical or horizontal wells. For example, in a reservoir with gas-cap and thin oil zone, a low vertical permeability compared to the horizontal permeability is beneficial with respect to coning. In this case, a long horizontal well is advantageous. Completion strategies must also consider anisotropy when deciding to place perforations near oil-water or gas-oil contacts.

2.1.4 Relative Permeability

Relative permeability is a fundamental rock property in reservoir simulation for prediction of production performance and ultimate recovery. Relative permeability describes the simultaneous flow of more than one fluid and is a dimensionless ratio between the effective permeability of a phase at a specific saturation normalized either to the absolute permeability, or to the effective permeability of the oil phase at initial water saturation (S_{wi}) (McPhee et al., 2015).

Relative permeability is a function of several properties. Some of the properties are wettability, pore-scale geometry, pore distribution (heterogeneity) and initial fluid saturation distribution. Relative permeability is also dependent on saturation history and results in different drainage and imbibition processes due to hysteresis effects (McPhee et al., 2015).

Figure 2.7 illustrates relative permeability and capillary pressure for water-wet and mixed-wet conditions for both drainage and imbibition processes. In a water-wet reservoir, oil will be in the larger pores and water will be in the smaller pores that were not invaded by oil after oil migration. Both phases are initially continuous and will start to flow under natural water drive or induced water injection. The oil relative permeability is high in the beginning of production because it flows through the larger pores and decreases with increasing water saturation. The water relative permeability is low at the beginning and increases as water saturation increases. The process will initially be a spontaneous imbibition process where water preferentially enters the smallest pores due to wetting forces. Later, water will start to enter larger pores and eventually be the only continuous phase and the final oil relative permeability becomes zero. The final water relative permeability is lower than the initially oil relative permeability because some oil will be trapped in the larger pores and prevent water to flow through these pores (Abdallah et al., 2007). Figure 2.7(left) illustrates this process for a water-wet reservoir. The dashed curves are the imbibition process (increasing water saturation), described above. The solid lines are the drainage process (increasing oil saturation). The drainage curves are always above the imbibition curves.

The processes and initial saturation distribution is similar in a mixed-wet reservoir because oil has probably migrated into a water-wet formation. The difference is that the oil fully occupying the largest pores has altered the wettability and made the surface oil-wet. Consequently, in a mixed-wet condition, water will flow through the largest pores at the start of production and remain in the center of the pores. It causes a more rapid decline in the oil relative permeability because the water occupies the most permeable paths. Figure 2.7(right) illustrates the process for a mixed-wet reservoir. Notice the greater water relative permeability for higher water saturation in the mixed-wet case. In a mixed-wet case, the oil will not be trapped because oil can flow through oil films along the surface. As a result, the water recovery at water breakthrough is lower in an oil-wet case, but the production will continue for a long period (Abdallah et al., 2007).

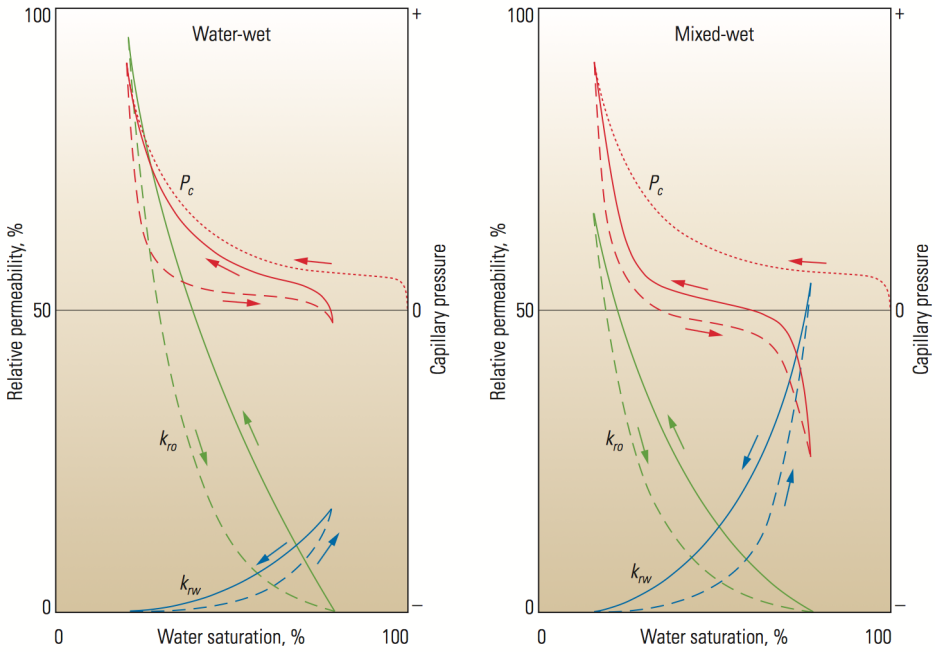

Figure 2.7: Capillary pressure and relative permeability for water-wet and mixed-wet conditions. Solid lines indicate the imbibition process, and dashed lines drainage. Figure from Abdallah et al. (2007)

2.1.5 Hysteresis

Relative permeability and capillary pressure curves are functions of water saturation, but they depend on the direction of saturation change i.e. different in drainage and imbibition processes. This is known as hysteresis and the path dependent curves are shown in Figure 2.7. The hysteresis effects on reservoir performance can be significant for processes with variable directions of saturation change (Braun and Holland, 1995). For example, when water coning occurs in an oil-producing well, the water saturation increases, but if the production rate is reduced or set to zero the water saturation can consequently switch to decreasing.

The hysteresis in drainage and imbibition capillary pressure and relative permeability also depends on the initial saturation at different height in the transition zone. Therefore, hysteresis between the primary drainage and imbibition can be represented by a series of scanning curves. Each scanning curve represents a specific starting saturation point on the drainage or imbibition curve and correspond to different heights in the transition zone (Abdallah et al., 2007).

Figure 2.8 and 2.9 illustrate scanning curves for hysteresis predictions in reservoir simulation. Figure 2.8 shows relative permeability hysteresis for a non-wetting phase and Figure 2.9 is water capillary pressure hysteresis. The complete drainage curve are Curve 1 to 2 and the complete imbibition curve are Curve 2 to 3. If the drainage or imbibition process is reversed at some point, the data used does not follow the previous values, but runs along a scanning curve (Schlumberger, 2015b). The scanning curve is Curve 4 to 5 in Figure 2.8 and Figure 2.9.

Representation of hysteresis behaviour in porous media is of particular interest in reservoir simulation. The simulator often require the complete drainage and imbibition curves for input data (Schlumberger, 2015b). Application of hysteresis is computational consuming and its effect on reservoir performance should therefore be considered.

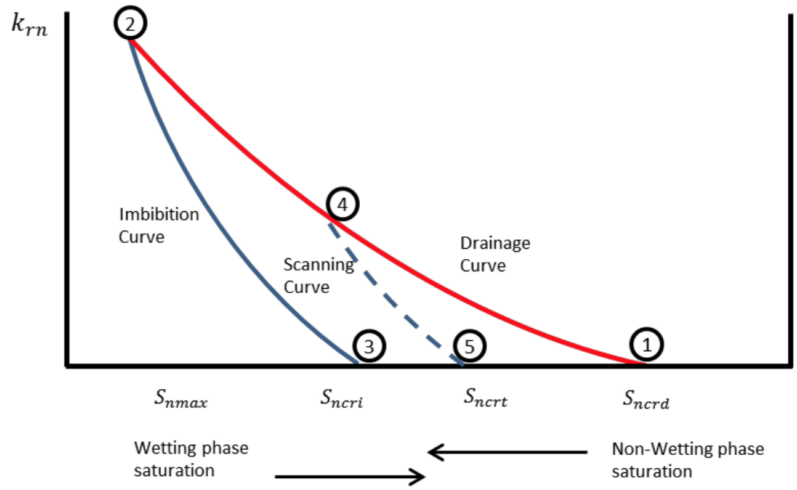

Figure 2.8: Drainage, imbibition and scanning relative permeability curves for an oil-water system. Figure from Schlumberger (2015b).

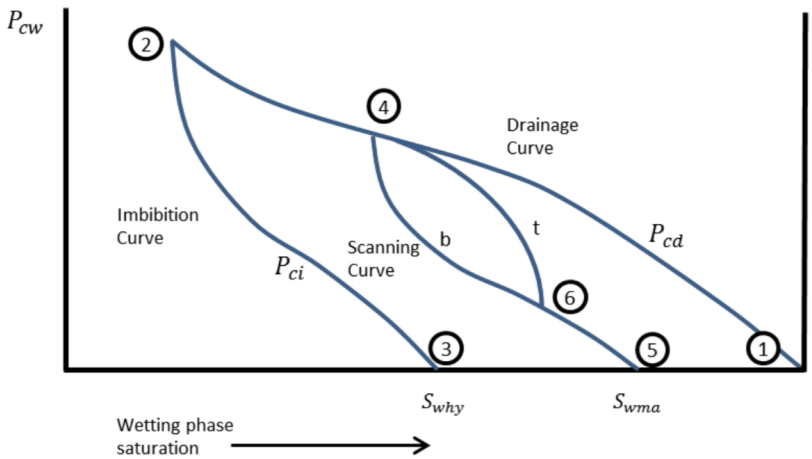

Figure 2.9: Drainage, imbibition and scanning capillary pressure curves for an oil-water system. Figure from Schlumberger (2015b).

2.2 Primary Recovery Mechanisms

Application of numerical simulation modelling is widely used for predicting oilfield performance. The confidence in the geological model and its predictions may result in lack of reservoir understanding and performance. By defining an average pressure decline for a reservoir, a material balance can be applied using simply production and pressure history together with fluid PVT properties. The material balance model is a useful tool to investigate reservoirs. It can be used to calculate hydrocarbons in place and define drive mechanisms. It is the simplest model for analysis of reservoir behavior, but perhaps the safest technique since no geological model is needed (Dake, 1994).

Primary drive mechanisms such as solution gas drive, gas-cap drive, natural water drive and compaction drive may contribute to production of an unconsolidated sandstone reservoir. In addition, secondary recovery mechanisms such as water injection and gas injection can be applied to increase the oil recovery. All these terms must be included in the material balance equation presented by Kleppe (2017b):

$$F = N(E_o + mE_g + E_{f,w}) + (W_i + W_e)B_w + G_i B_g \tag{2.2}$$

where production terms are:

$$F = N_p[B_o + (R_p - R_{So})B_o] + W_p B_w$$

oil expansion and solution gas expansion terms are:

$$E_o = (B_o - B_{oi}) + (R_{soi} - R_{so})B_g$$

gas-cap expansion terms are:

$$E_g = B_{oi}(\frac{B_g}{B_{gi}} - 1)$$

and rock compaction and water expansion terms are:

$$E_{f,w} = -(1+m)B_{oi}\frac{c_r + c_w S_{wi}}{1 - S_{wi}}\Delta P$$

Definitions of the symbols are listed in Appendix A and the terms are described in the following sections. The dominating primary drive mechanisms in Alta West are likely to be solution gas drive, gas-cap drive and natural water drive. These mechanisms are the once to be discussed. Excluding rock compaction, water expansion and water- and gas injection, the volume balance can be evaluated in reservoir barrels as:

Underground withdrawal = Expansion of the system + Cumulative water influx

Underground withdrawal is the observed surface production of oil and gas. Right hand side is expansion of oil and its originally dissolved gas plus gas-cap expansion plus aquifer influx. Equation 2.2 can be reduced to:

$$F = N(E_o + mE_g) + W_e B_w \tag{2.3}$$

2.2.1 Solution Gas Drive

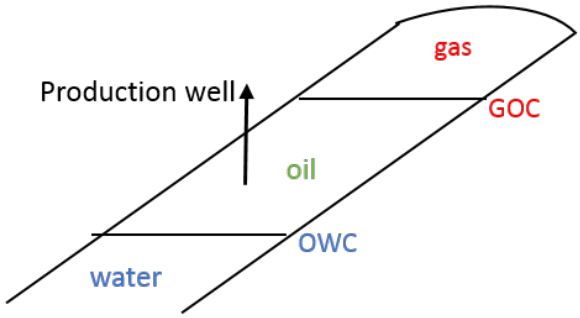

Figure 2.10: Saturated reservoir at bubble point pressure and initial gas-cap.

Solution gas drive occurs once the pressure falls below the bubble point pressure (P_{bp}). A saturated oil reservoir with gas-cap, as shown in Figure 2.10, has initial pressure at bubble point pressure. As pressure declines, gas will be liberated from the saturated oil and free gas will develop and expand in the oil column. The release of gas results in shrinkage of oil. The total change in volume (expansion) of the oil column becomes:

$$E_o = N[(B_o - B_{oi}) + (R_{soi} - R_{so})B_g] \tag{2.4}$$

Where the first term is shrinkage of oil and the last term is the amount of liberated gas.

When gas is liberated, the pressure decline dampens. Figure 2.11 shows a schematic production history of a solution gas drive with initial reservoir pressure above bubble point. When pressure reaches bubble point pressure, immobile free gas saturation develops. At a certain pressure below bubble point, the gas saturation increases until free gas becomes mobile. After this point, the producing gas-oil-ratio (GOR) will increase. After a long production period, maximum GOR is reached (Dake, 1978). A considerably amount of production wells are often shut in before maximum GOR is reached and will not experience a decreasing GOR (Petrowiki, 2015b).

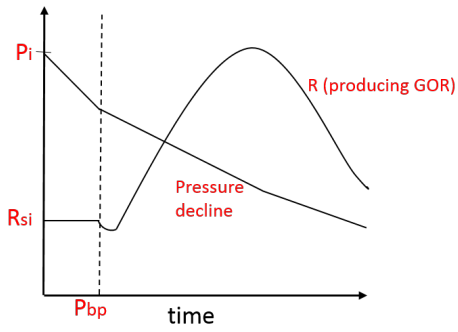

Figure 2.11: Schematic of the production history of a solution gas drive. Initial reservoir pressure above bubble point pressure.

As mentioned, a saturated oil reservoir has $P_i = P_{bp}$ and GOR will increase right after start of production. As much gas as possible should be kept in the reservoir to obtain a high primary recovery. It requires that the GOR is maintained as low as possible (Dake, 1978)

2.2.2 Gas-Cap Drive

Some reservoirs have a segregated-gas zone above the oil column, known as a gas-cap. In addition to the initial free gas, dissolved gas from oil can migrate up to the gas-cap during depletion. When reservoir pressure drops, the gas-cap will expand and displace oil toward to the production well (Dake, 1994). The initially volume of the gas-cap can be expressed in terms of reservoir volume as:

$$mNB_{oi}$$

and, at reduced pressure, p, the volume of the gas-cap can be expressed as:

$$mNB_{oi}\frac{B_g}{B_{gi}}$$

and the gas-cap expansion is therefore:

$$mE_g = mNB_{oi}(\frac{B_g}{B_{gi}} - 1) \tag{2.5}$$

Because of expansion, gas-cap acts to reduce the pressure decline and extend the production period of the reservoir. The pressure decline is less severe than for a solution gas drive and oil recovery is usually greater. The degree of oil recovery improvement is restricted by the size of the gas-cap, the vertical permeability and/or formation dip. Favorable conditions are large gas-cap, steeply dipping reservoirs and high vertical permeability. To avoid early gas breakthrough low production rate is beneficial. To keep the gas in the reservoir and avoid gas disposal problems, the upper part of the wells may need to be shut as the gas-cap expands downward (Dake, 1978).

2.2.3 Natural Water Drive

Natural water drive refers to water influx when a reservoir is connected to an active aquifer. Aquifer influx starts once the pressure decline has travelled to the entire or partially throughout the aquifer's volume. The pressure drop causes the aquifer water to expand and flow into the reservoir (Dake, 1994). The water influx can be expressed as the product of aquifer compressibility, initial water volume and pressure drop:

$$W_e = (c_w + c_r)W_i\Delta P \tag{2.6}$$

The aquifer compressibility is the sum of water (c_w) and pore (c_r) compressibilities. The sum of c_w and c_r is relatively small and the volume of water must be large in order to maintain a dominating natural water drive. If not, its influence as a drive mechanism will be neglected in the material balance equation. For very large aquifers, there will

be a time lag from start of depletion until full response from aquifer influx. The natural water drive is therefor time dependent (Dake, 1994).

The aquifer influx is generally, if not always, a great uncertainty and difficult to determine. Knowledge about the aquifer is limited and its properties are rarely measured since wells are not drilled into the aquifer.

The sum of equation 2.4, 2.5 and 2.6 equals the right hand side of material balance equation 2.3. The sum of the three terms defines the volume change of the reservoir during depletion. The rock compaction and water expansion term, $E_{f,w}$, can often be neglected when assuming a dominating aquifer influx and gas-cap drive. This is reasonable because the effect of c_w and c_r are much smaller compared to the effect of gas compressibility. In addition, natural water drive and gas-cap expansion helps maintain the reservoir pressure resulting in less pressure drop and reduced $E_{f,w}$-term (Dake, 1978).

2.3 Relative Permeability and Fluid Displacement Models

2.3.1 Relative Permeability Models

There are at least two fundamental methods to simulate multiphase flow experiments. One is to estimate the multiphase flow properties from measured data, and the other is the representation of theoretical, analytical and/or empirical correlations for relative permeability. Special core analysis (SCAL) is expensive and time consuming and the number of core plugs used for SCAL are usually limited. As a result, SCAL does not cover all flow zones and may give poor reservoir representation. Instead, reservoir engineers often use quick and easy prediction models as input for the simulation models.

The following relative permeability models included in this section are derived for two phase flow. However, in oil reservoirs with gas-cap drive, solution gas drive and possibly gas injection, such as the Alta West reservoir, a three phase flow will occur. There are several three-phase relative permeability models, but they will not be presented in this thesis because minor attention was given to this topic.

Modified Brooks and Corey Model

The Modified Brooks and Corey model (MBC) is probably the most widely used model to describe two-phase relative permeability relationship. It is also called the power law model because it is a power function with one empirical parameter. The MBC model is explicitly a function of relative permeability end-points. That is, end-point relative permeability to oil at irreducible water saturation and end-point relative permeability to water at residual oil saturation (Behrenbruch and Goda, 2005). The power functions can be expressed by:

$$k_{ro} = k'_{ro}(S_{on})^{N_o} = k'_{ro}(\frac{1 - S_w - S_{or}}{1 - S_{wi} - S_{or}})^{N_o}$$

and

$$k_{rw} = k'_{rw}(S_{wn})^{N_w} = k'_{rw}(\frac{1 - S_w - S_{or}}{1 - S_{wi} - S_{or}})^{N_w}$$

where

k_{ro} = oil relative permeability normalized to absolute plug air permeability

k_{rw} = eater relative permeability normalized to absolute plug air permeability

k'_{ro} = end point relative permeability to oil normalized to absolute plug air permeability

k'_{rw} = end point relative permeability to water normalized to absolute plug air permeability

S_{on} = normalized oil saturation

S_{wn} = normalized water saturation

S_w = water saturation

S_{wi} = irreducible water saturation

S_{or} = reducible oil saturation

N_o = corey exponent to oil

N_w = corey exponent to water

The MBC model is applicable to both water-oil and gas-oil systems. The equations are valuable in interpolating and extrapolating relative permeability curves, generating curves if only end-point-data are available and in assessing the validity of laboratory data (McPhee et al., 2015). The model can also be used to support quantitative data for the wettability of a rock based on the empirical Corey exponents (Behrenbruch and Goda, 2005). N_w and N_o are strongly correlated to wettability and the typically expected range of the exponents are listed in Table 2.1

Table 2.1: Typical oil and water Corey exponents. Values from McPhee et al. (2015).

Wettability	**No,w (k_{ro})**	**Nw (k_{rw})**
Water-wet	2-4	5-8
Intermediate-wet	4-6	3-5
Oil-wet	6-8	2-3

The relationship between the oil ($N_{o,g}$) and gas (N_g) Corey exponents is normally well defined and more predictable compared to N_w and N_o where changes in wettability has greater influence. This is because the oil is always the wetting phase, meaning $N_{o,g}$ is much larger than N_g (McPhee et al., 2015). Typical ranges are listed in Table 2.2.

Table 2.2: Typical gas and oil Corey exponents. Value from McPhee et al. (2015).

Corey Exponent	Values
No,g	4-7
Ng	1.3-3.0

Even though the MBC model is the most used model for prediction of relative permeability curves, there are certain shortcomings. The model is a direct function of the end-points and hardly influenced by the remaining data. With a small saturation range, the model shows limitations to present the flexibility that is required to predict relative permeability for the entire saturation range (Behrenbruch and Goda, 2005).

LET-Correlation

Lomeland et al. (2005) proposed a new relative permeability model to overcome the shortcomings of the MCB and other published correlations. Lomeland et al. (2005) stated that neither of the published correlations were able to describe the relative permeability curves in the entire saturation range from low to high water saturations. They believe that the relative permeability functions need to have sufficient degrees of freedom to model the measured data and still remain simple and easy to communicate with. Therefore, they proposed a new smooth and flexible three parameter analytical correlation that influences different parts of the relative permeability curve. The three parameters to describe the correlation is L, E and T. For a two-phase water-oil system, the functions become:

$$K_{row} = K^x_{ro} \frac{(1 - S_{wn})^{L^w_o}}{(1 - S_{wn})^{L^w_o} + E^w_o S^{T^w_o}_{wn}} \tag{2.7}$$

and

$$K_{rw} = K^o_{rw} \frac{(1 - S_{wn})^{L^o_w}}{(1 - S_{wn})^{L^o_w} + E^o_w S^{T^o_w}_{wn}} \tag{2.8}$$

and

$$S_{wn} = \frac{S_w - S_{wi}}{1 - S_{wi} - S_{orw}}$$

where

S_{wn} = nomalized water saturation

S_w = water saturation

S_{wi} = irreducible water saturation

S_{orw} = reducible water saturation after water injection

K_{row} = oil relative permeability with water injection

K_{ro}^x = oil relative permeability at irreducible water saturation and zero gas saturation

K_{rw} = water relative permeability

K_{rw}^o = water relative permeability at residual oil saturation

L_o^w, E_o^w and T_o^w = empirical parameters for oil phase with associated water phase

L_w^o, E_w^o and T_w^o = empirical parameters for water phase with associated oil phase

Figure 2.12 illustrates oil and water relative permeability curves from the MCB model and the LET correlation. The difference in oil relative permeability is more significant compared to the water relative permeability. The LET correlation is the dashed lines, illustrated as s-shaped curves. Lomeland et al. (2005) believe the s-behaviour is more representative because it is often observed from core flooding experiments. The significant difference in oil relative permeability at low water saturation can give great variations in reservoir simulation.

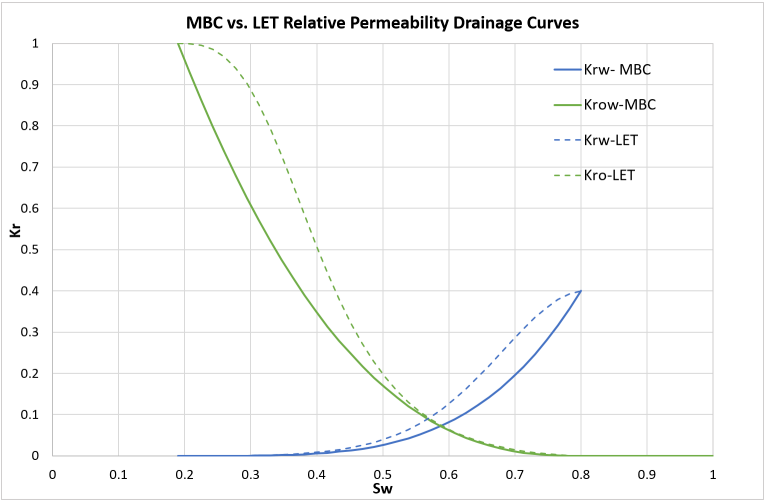

Figure 2.12: Comparion of Modified Brooks and Corey model (MBC) and LET-correlation of water-oil relative permeability drainage curves.

2.3.2 The Buckley-Leverett Solution

The Buckley-Leverett solution is frequently used for describing immiscible displacement in core flooding experiments and reservoir flow predictions. It applies the theory of the Buckley-Leverett frontal advance equation together with the fractional flow equation. The full derivation of the equations will not be described in the thesis. Instead, a discussion of how the Buckley-Leverett solution is used to evaluate displacement efficiency in reservoirs will be given. The Buckley-Leverett solution is derived for the following physical conditions (Dake, 1994):

- One dimensional displacement
- Constant pressure drop
- Immiscible fluids

The fractional flow of water produced from a core or a production well is defined as:

$$f_w = \frac{q_w}{q_w + q_o}$$

where

f_w = fractional flow of water produced

q_w = the volumetric water rate

q_o = the volumetric oil rate

In a dipping reservoir with two fluids flowing in the system, Darcy's law can be expressed as:

$$q_o = \frac{kk_{ro}A}{\mu_o}(\frac{\partial P_o}{\partial x} + \rho_o g sin\alpha)$$

$$q_w = \frac{kk_{rw}A}{\mu_w}(\frac{\partial P_w}{\partial x} + \rho_o g sin\alpha)$$

where

k = absolute permeability

k_{ro}/k_{rw} = relative permeability for oil/water

A = cross sectional area

P_o / P_w = oil/water pressure

μ_o / μ_w= oil/water viscosity

α = the dip angle of the system

Substituting for the rates using Darcy's law, the fractional flow equation can be expressed by equation 2.9. This is the simplest form of the fractional flow equation with negligible capillary pressure and horizontal flow (no dip angle).

$$f_w = \frac{1}{1 + \frac{k_{ro}}{\mu_o} \frac{\mu_w}{k_{rw}}} \tag{2.9}$$

The Buckley-Leverett frontal advance equation was derived to determine an expression for the velocity of a plane of constant water saturation during a displacement process. It is derived by applying the physical principle of mass conservation for displacement at constant pressure (Dake, 1994). The Buckely-Leverett frontal advance equation can be expressed in terms of the position of the fluid front:

$$x_f = \frac{q_{inj} t}{A\phi} (\frac{df_w}{dS_w})_f \tag{2.10}$$

where

x_f = the position of the fluid front

q_{inj} = constant injection rate

t = any given time

A = cross section area

ϕ = porosity

$(\frac{df_w}{dS_w})_f$ = Is the derivative of the fractional flow equation

Equation 2.10 states that the velocity of a plane ($v = \frac{x_f}{t}$) of constant water saturation is proportional to the derivative of the fractional flow curve. The fractional flow is a function of water saturation only and its dependency on relative permeability (Dake, 1994). With a set of water and oil relative permeability curves, the following plot of the fractional flow curve and its derivative can be made:

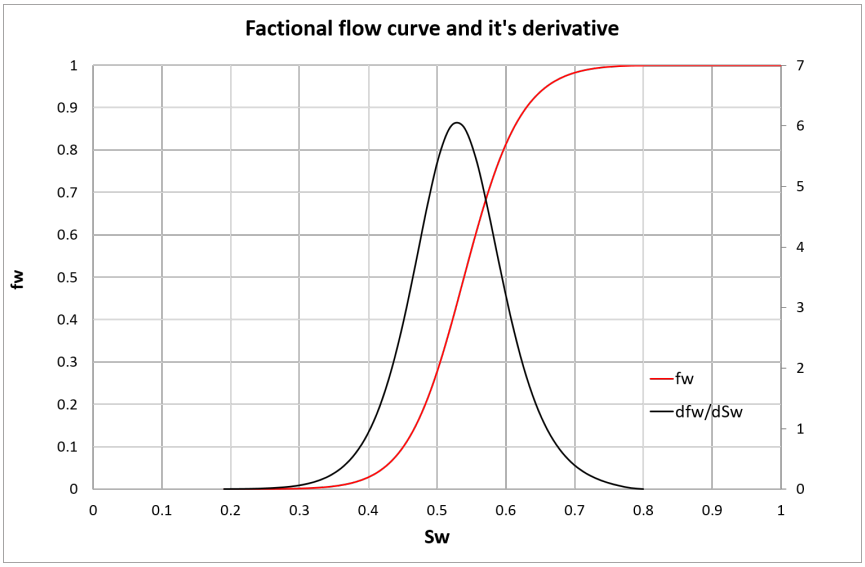

Figure 2.13: Fractional flow curve and its derivative vs. water saturation for a given oil and water relative permeability.

Equation 2.10 can be used to plot water saturation vs. position. Figure 2.14 represents this plot, which illustrates an impossible physical situation because there are two saturations at each x-position. The Buckley-Leverett solution applies a modification to the problem by defining a saturation discontinuity at x_f (Kleppe, 2017a). Two areas are marked in the plot as A1 and A2. x_f is defined as the point on the x-axis where the two areas are equal. Figure 2.14 demonstrates the concept where, in this example, area A1 and A2 are equal at x_f=0.33.

Figure 2.15 shows the resulting water saturation profile. The profile represents the water saturation at the front at water break-through (S_{wf}). S_{wf} is graphically shown in the fractional flow plot in Figure 2.16.

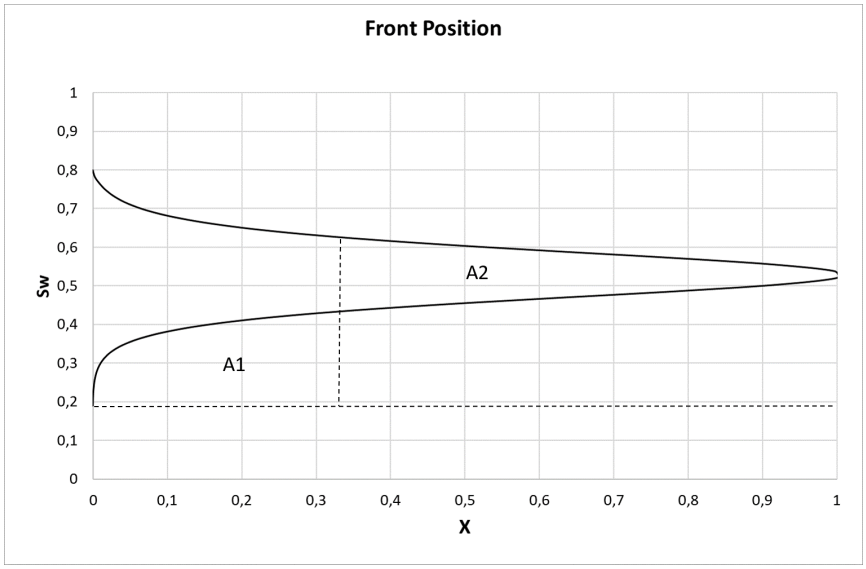

Figure 2.14: Buckley Leverett: Impossible physical front position vs. water saturation.

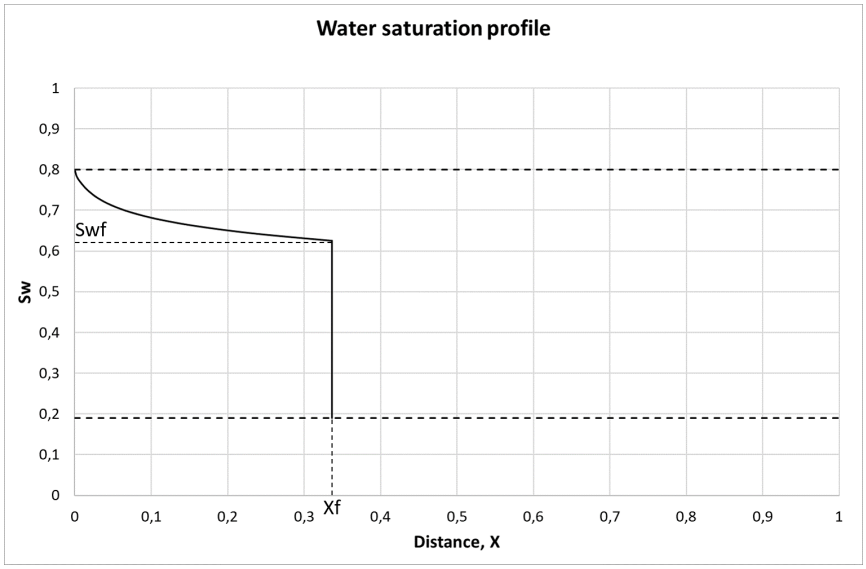

Figure 2.15: Final water saturation profile derived by Buckley-Leverett solution.

The Buckley-Leverett solution can be used to determine the oil recovery and water cut at time of break-trough. The water cut is equal the fractional flow at water break-through which is defined as $f_{wf}(S_{wf})$. The recovery can be defined by (Kleppe, 2017a):

$$RF = \frac{\overline{S}_w - S_{wir}}{1 - S_{wir}}$$

where

$\overline{S}_w$ = average saturation behind the fluid front

S_{wir} = initial water saturation

The average saturation behind the fluid front is determined by extending the tangent line between point ($f_w = 0$, S_{wir}) and (f_{wf},S_{wf}) to intersect the line where $f_w = 1$. The tangent line and the point at where $\overline{S}_w$ intersect $f_w = 1$ is illustrated in Figure 2.16.

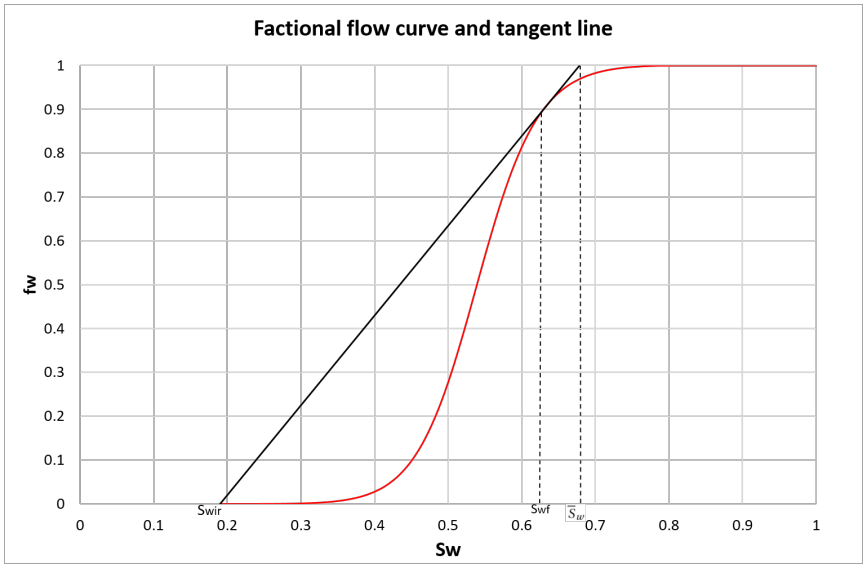

Figure 2.16: Fractional flow curve and the tangent line used to determine average water saturation behind the fluid front.

The Effect of Mobility Ratio on Fractional Flow Curve

The mobility ratio is defined as:

$$M = \frac{k'_{rw}}{\mu_w} / \frac{k'_{ro}}{\mu_o} \tag{2.11}$$

where

k'_{rw} = water relative permeability at residual oil saturation

k'_{ro} = oil relative permeability at initial water saturation

μ_w=water viscosity

μ_o= oil viscosity

The mobility ratio is related to the efficiency of water flooding. The lower mobility ratio, the better displacement efficiency. Thus, low oil viscosity results in favorable mobility ratio (Dake, 1994). The fractional flow equation can be defined in terms of mobility ratio:

$$f_w = \frac{1}{1 + \frac{1}{M}}$$

The fractional flow curve shifts to the right the more efficient displacement. Best recovery is obtained if the mobility is sufficiently low such that the fractional flow curve has no inflection point (Kleppe, 2017a). It occurs if M ≤ 1. The displacement is piston-like, meaning that all movable oil is recovered by the injection of an equivalent volume of water (Dake, 1994). Figure 2.17 shows typical fractional flow curves for high and low oil viscosity together with a piston-like displacement.

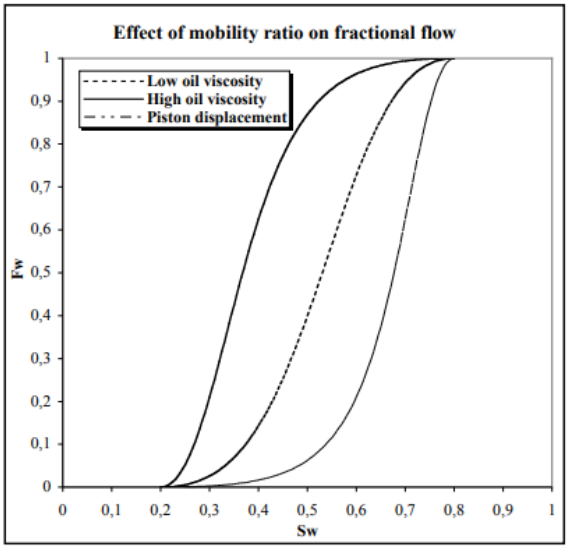

Figure 2.17: Effect of mobility ratio on fractional flow curves for high viscosity, low viscosity and piston-like displacement. Figure from Kleppe (2017a).

The Effect of Gravity on Fractional Flow Curve

The effect of gravity on fractional flow curve is dependent on the dip-angle of the reservoir. In a non-horizontal reservoir with water displacement in the up-dip direction, the gravity forces contributes to higher recovery efficiency. With dip angle α, the fractional flow equation becomes:

$$f_w = \frac{1-G}{1+\frac{1}{M}}$$

where G is the gravity forces defined by:

$$G = \frac{kk_{ro}A}{q_o\mu_o}\Delta\rho g sin\alpha$$

The higher dig angle, the more efficient displacement. The effect of gravity forces is illustrated in Figure 2.18. The fractional flow curve shifts to the right for a vertical flow with injection from the bottom of the reservoir (Kleppe, 2017a).

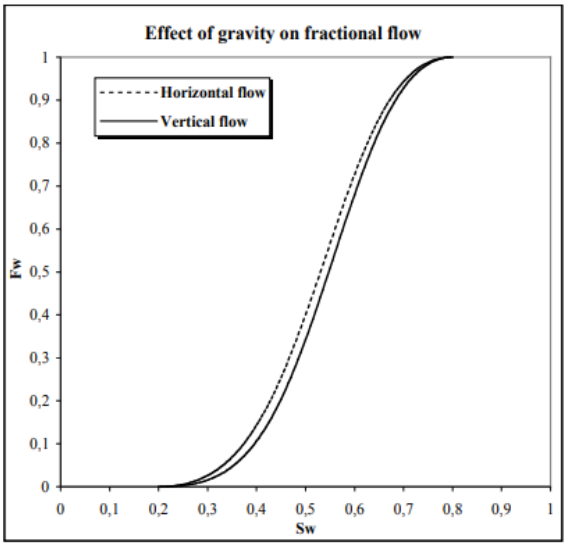

Figure 2.18: Effect of gravity on fractional flow curves for vertical and horizontal flow. Figure from Kleppe (2017a).

The Effect of Heterogeneity on Displacement Efficiency

The Buckley-Leverett solution describes the displacement efficiency for one-dimensional homogeneous systems on the scale of core flooding experiments. Water injection is conducted on macroscopic heterogeneous reservoir sections and the recovery efficiency is therefore influenced by three physical factors; mobility, gravity and heterogeneity. Heterogeneity is a two-dimensional problem and can not be solved by the Buckley-Leverett solution or by the fractional flow curve (Dake, 1994).

The Buckley-Leverett solution is based on the principle of mass conversation, which is independent on absolute permeability. Similarly, in the derivation of the fractional flow equation of horizontal flow and negligible capillary pressure, the permeability is canceled, except if; gravity forces are included for dipping reservoirs. However, increasing or decreasing the absolute permeability will have no effect on the vertical sweep efficiency. The effects of heterogeneity on displacement efficiency are therefore mainly influenced by the vertical permeability distribution. Figure 2.19 illustrates the effect of different permeability distributions across a macroscopic reservoir section (Dake, 1994). It must be mentioned that the average permeability is the same for all cases.

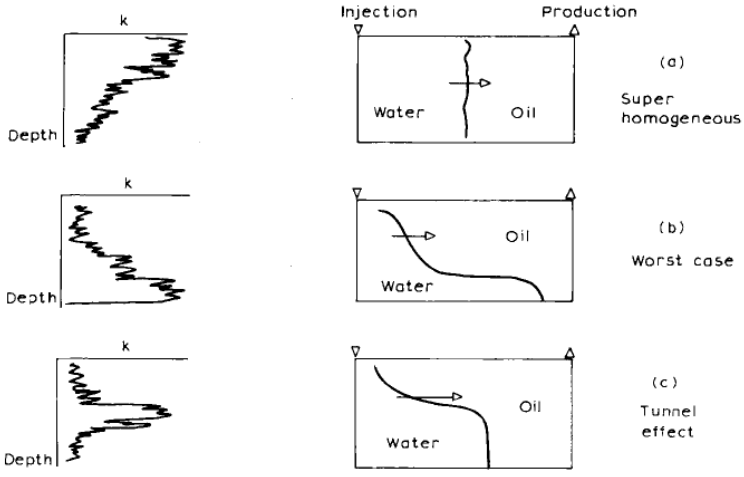

Figure 2.19: Influence from permeability distributions across a macroscopic reservoir section on oil-water displacement efficiency. Figure from Dake (1994).

The favorable situation is Case a with coarsening upwards in permeability. The majority of the injected water enters the top of the reservoir with highest permeability. Further away from the well, the gravity forces dominates and pushes the water toward the reservoir bottom. The result is a piston-like displacement. Case b is the least favorable situation where permeability increase with depth. The majority of the injected water now enters the bottom of the reservoir resulting in early water break-through and poor vertical sweep efficiency. Case c is somewhere between Case a and b (Dake, 1994).

2.3.3 Immiscible Gas Displacement

In immiscible gas displacement, there is no mass transfer between the gas and oil phases. Under these conditions, there will be a surface tension between the two phases, meaning that a residual oil saturation will be trapped in the pores after the pores are flooded with gas. As for water drive, there are mainly three physical factors controlling the gas displacement efficiency; mobility ratio, heterogeneity and gravity (Dake, 1994).

The viscosity difference between oil and gas is usually much larger than between oil and water. It results in a high gas-oil mobility ratio, defined by equation 2.12, where $k_{rg}^{'}$ and $k_{ro}^{'}$ are end-point relative permeabilities for a gas-oil system. The ratio may be highly unfavorable and gas is capable of moving several times faster than oil under a given pressure gradient (Dake, 1994).

$$M = \frac{k_{rg}^{'}}{\mu_g} / \frac{k_{ro}^{'}}{\mu_o} \tag{2.12}$$

Unfavorable mobility ratio causes viscous flow instabilities, known as viscous fingering. It is essential for gas-oil displacement, especially if the displacement is horizontal. In a reservoir, two physical aspects contribute to viscous fingering. The first is permeability heterogeneities. The majority of the injected gas will enter the high permeability layers. The second aspect is that gas is lighter than oil and gravity forces cause the gas to override the oil and initiate a viscous finger (Petrowiki, 2015a).

The heterogeneity and gravity effects on immiscible gas displacement are strongly in-

terrelated and must be treated in conjunction. The gravity difference, $\Delta\rho = \rho_o - \rho_g$, is larger than for water drive, which enhances the significance of gravity forces in immiscible gas displacement. The increased gravity difference together with the low gas viscosity cause more rapid segregation and reduces the capillary transition zone. It results in a sharp interface between the gas and oil phase (Dake, 1994).

Since gas is lighter than oil, the influence of permeability distribution on the stability of displacement is inverse of water drive. Figure 2.20 illustrates that a coarsening upward sequence is the worst condition for gas displacement. This is in contrast with water displacement, where coarsening upward is the favorable condition as illustrated in Figure 2.19.

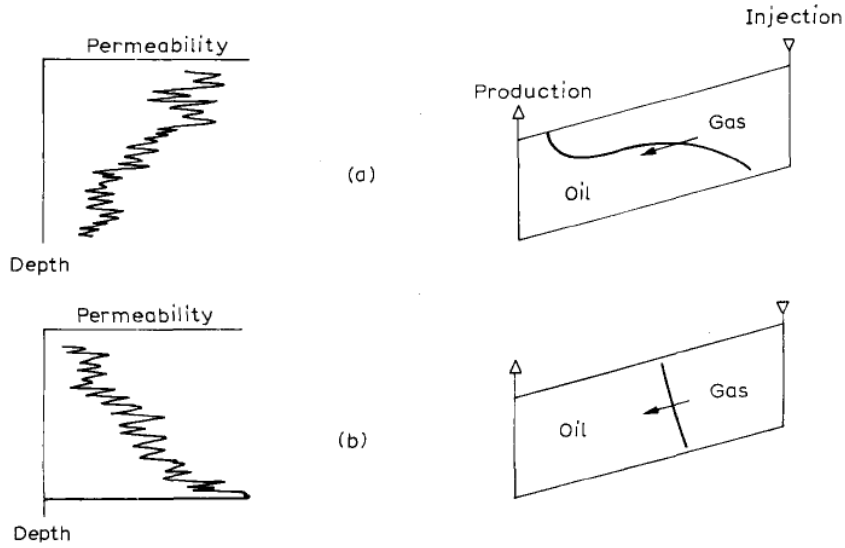

Figure 2.20: Influence from permeability distribution on stability of gas-oil displacement under segregated condition. Figure from Dake (1994).

However, the viscous forces may be neglected if the injection rate is sufficiently low. Because of the increased significance of gravity forces, Case b in Figure 2.20, can achieve a reasonable stable front by reducing the injection rate (Dake, 1994).

Chapter 3

Reservoir Modeling

The Eclipse reservoir simulator with the ECLIPSE 100 Black Oil option is applied to run simulations in this thesis. ECLIPSE 100 can be used to simulate one, two or three phase systems where the oil and gas phases are represented as one component each. The fluid properties are functions of pressure. The composition of oil and gas components are assumed constant with pressure and time to save both computer storage and computer time. In the three phase option, the simulator can also be used to model live oil with dissolved gas and wet gas with vaporized oil (Schlumberger, 2015b).

The user interface for Eclipse is Petrel Reservoir Engineering, which integrates the static and dynamic modeling process into a seamless workflow. Petrel is a useful workspace to provide integration across disciplines. It allows the reservoir engineer, among other options, to construct wells, design development strategies and visualize reservoir simulation results (Schlumberger, 2018b).

In this chapter, a technical description of Eclipse reservoir modeling is given. Only the most critical methods with respect to the simulation outputs are discussed. The Alta reservoir contains an oil leg with a gas-cap and underlying aquifer. The reservoir model must contain three phases to reflect gas- and water displacement. Table 3.1 summarizes the main keywords associated with the modeling.

Table 3.1: Keyword summary from Eclipse Reference Manual (Schlumberger, 2015a).

Keyword	**Section**	**Description**
SWOF	PROPS	Input tables of water relative permeability, oil-in-water relative permeability and water-oil capillary pressure as functions of the water saturation.
SGOF	PROPS	Input tables of gas relative permeability, oil-in-gas relative permeability and gas-oil capillary pressure as functions of the gas saturation.
SWATINIT	PROPS	Initial water saturations for capillary pressure scaling.
ENDSCALE	RUNSPEC	Activates the saturation end-point scaling option
SCALERS	PROPS	Controls the end point scaling method
JFUNK/JFUNCR	GRID	Activates the Leverett J-function option / Activates the Leverett J-function option per saturation table
AQUNUM	GRID	Assigns a numerical aquifer to a block
AQUCON	GRID	Connects a numerical aquifer (declared using the AQUNUM keyword) to one or more reservoir cells.

3.1 Saturation Table Scaling

Capillary pressure and relative permeability functions are crucial for accurate estimation of the fluids in place and prediction of oil recovery. Incorrect use of the saturation functions may cause significant errors in reservoir simulations. The critical water saturation, which is defined as the highest water saturation for which the water is immobile, is held in place by capillary forces. As will be described in details in the following sections, capillary pressure is dependent on pore size distribution, porosity and permeability. Consequently, heterogeneous reservoirs will contain capillary pressure variations that will influence the critical water saturation.

Since the input saturation tables (from SWOF or SGOF) determine the end-point satu-

rations for each grid cell in a reservoir model, scaling of the relative permeability and capillary pressure curves will have a great impact on the reservoir fluid in place. Table 3.2 lists the unscaled saturation end-points taken from the saturation tables defined in the simulator. These end-points will be scaled to the left or right along the x-axis. Figure 3.1 illustrates the unscaled relative permeability curves with the corresponding saturation end-points.

Table 3.2: Saturation table end-points from Eclipse Technical Description (Schlumberger, 2015b).

Keyword	**Description**
SWL	The connate water saturation. This is the smallest water saturation entry table.
SWCR	The critical water saturation. This is the highest water saturation for which the water is immobile.
SWU	The maximum water saturation. This is the largest water saturation entry in a water saturation table.
SGL	The connate gas saturation. This is the smallest gas saturation entry in a gas saturation table.
SGCR	The critical gas saturation. This is the highest gas saturation for which the gas is immobile.
SGU	The maximum gas saturation. This is the largest gas saturation entry in a gas saturation table.
SOWCR	The critical oil-in-water saturation. This is the highest oil saturation for which oil is immobile in an oil-water system.
SOGCR	The critical oil-in-gas saturation. This is the highest oil saturation for which the oil is immobile in an oil-gas-connate water system.
SGWCR	The scaled critical gas-in-water saturation. This is the highest gas saturation which the gas is immobile in a gas-water system.
SWGCR	The scaled critical water-in-gas saturation. This is the highest water saturation for which the water is immobile in a water-gas system.

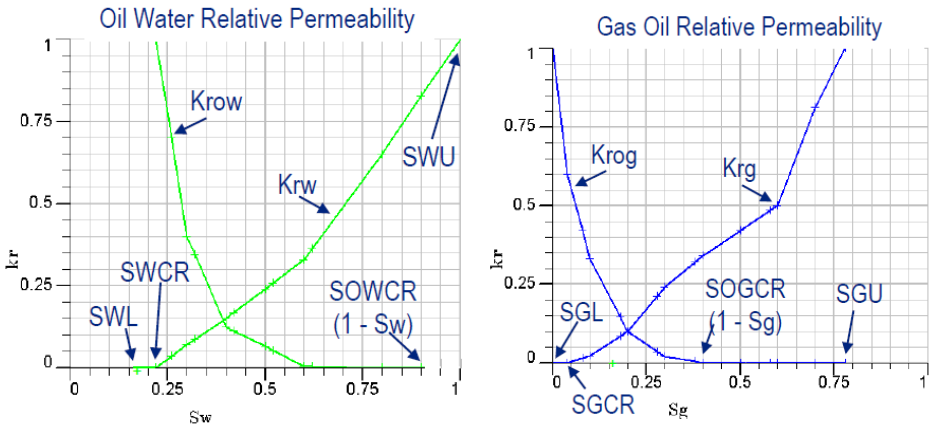

Figure 3.1: Unscaled oil-water (left) and gas-oil (right) relative permeability curves and their saturation end-points. Figure from (Schlumberger, 2015b).

In Eclipse simulator, the end-point scaling option is enabled by the ENDSCALE keyword in the RUNSPEC section. The scaling is applied separately on the relative permeability and capillary pressure curves. The scaling option enables new values to be defined for any of the 10 end-point saturations (Schlumberger, 2015b).

There are two options available for the scaling of relative permeabilities. It is a two-point transformation where the scaling process preserves relative permeabilites at two saturation nodes, or a three-point transformation where scaling preserves the relative permeabilities at three saturation nodes. The preferred scaling option can be activated by using the SCALERS keyword in the PROPS section (Schlumberger, 2015b). In this thesis, the two-point scaling option is used and Figure 3.2 is an example of how the relative permeability for oil-water and gas-oil are scaled by the two-point option.

It is also possible to scale the relative permeability vertically at the maximum phase saturation and the critical saturation of the relevant phase. However, this option was not applied on a block by block basis in this thesis. Since vertical scaling of the relative permeability curves represent the wettability preference of the rock surface it will be included in the relative permeability sensitivity study in Chapter 5.

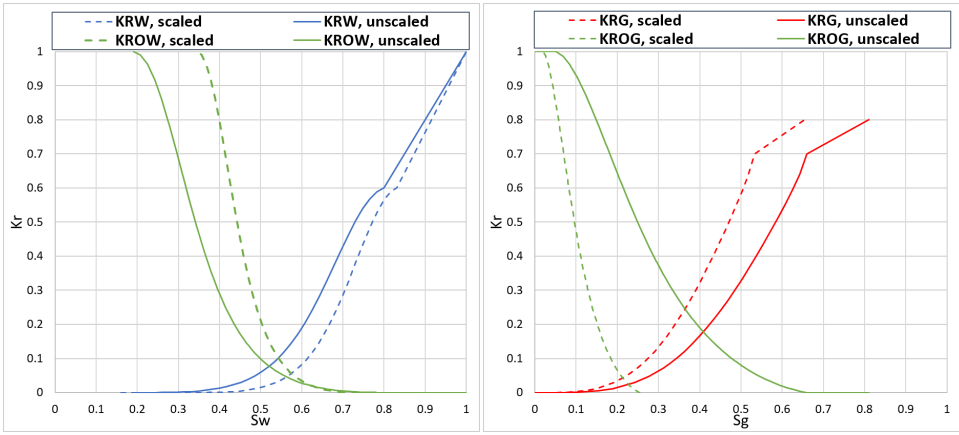

Figure 3.2: An example of scaled and unscaled oil-water (left) and gas-oil (right) relative permeability curves with respect to their scaled and unscaled grid cells' end-point saturations.

The capillary pressure curves are scaled by the grid cells' connate water (SWL)and maximum water (SWU) saturations for an oil-water system and connate gas (SGL) and maximum gas (SGU) saturations for a gas-oil system. Figure 3.3 is an example showing how an oil-water capillary pressure curve is scaled by the SWL and SWU end-points (Schlumberger, 2015b).

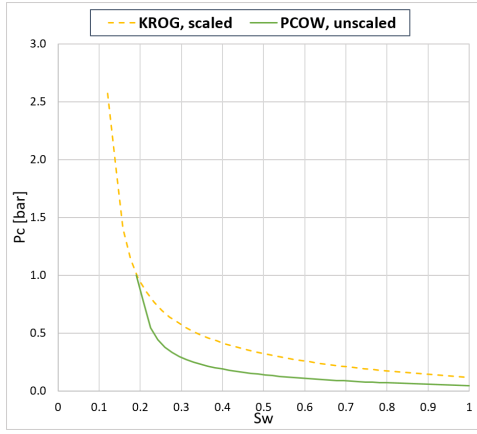

Figure 3.3: An example of scaled and unscaled oil-water capillary pressure curves with respect to their scaled and unscaled grid cells's end-point saturations.

There are several consistency requirements related to end-point scaling. In addition to make sure the requirements are fulfilled, the degree of scaling must not exceed what is

reasonable. If the saturation end-points are scaled substantially to the left or right at the x-axis, the shape of the curves may become steep, making the curves unphysical. To avoid unreasonable curves, a cut-off to the end-points can be set. Incorrect scaling may result in an un-equilibrated static model that has no physical meaning.

3.2 Leverett J-Function

A common practice to specify initial water saturation and capillary pressure curves for reservoir simulation is by using the Leverett J-Function. Before the description of how the J-function are used in Eclipse modeling, the origin of the function will be described.

Leverett (1941) suggested the following definition from evaluations of gas-water capillary pressure for drainage and imbibition in unconsolidated sands:

$$J(S_w) = \frac{P_c}{\sigma \cdot cos(\theta)} \cdot \sqrt{\frac{K}{\phi}} \tag{3.1}$$

where

P_c = capillary pressure

σ = surface tension between oil/water

K = rock permeability

ϕ = rock porosity

θ = contact angle between oil and water

Equation 3.1 is known as the Leverett J-Function. It is a dimensionless group that allows capillary pressure function to be correlated with rock properties. The function is obtained from experimental data by plotting $\frac{P_c}{\sigma} \cdot \sqrt{\frac{K}{\phi}}$ vs S_w. Notice that the $cos(\theta)$-term is excluded. However, the term is occasionally used in the definition of the J-function, although Leverett did not use it. Leverett (1941) evaluated four plots from height-saturation experiments on clean unconsolidated sands. He observed that the four plots fell satisfactorily near two curves, one for imbibition of water and the other for drainage. Figure 3.4 shows the results from the experiments and the two corresponding J-function curves.

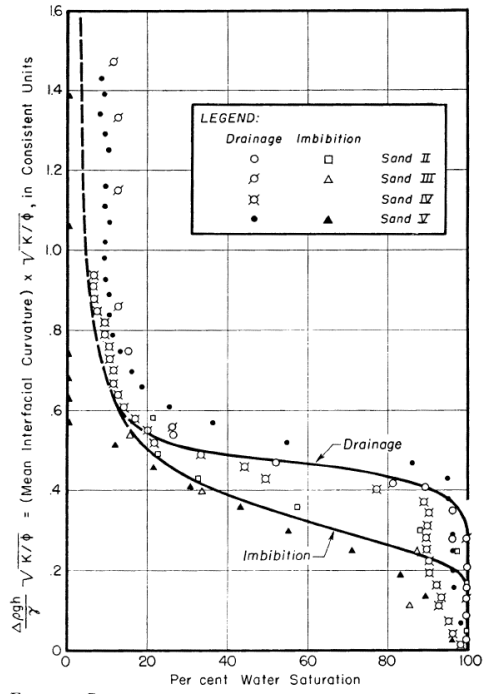

Figure 3.4: Correlation of data from height-saturation experiments on clean unconsolidated sands conducted by Leverett (1941).

The J-function is a capillary pressure curve normalized by porosity and permeability. It is used to merge capillary pressure data for rocks with similar pore types and wettability, but with different permeabilities into one single equation.

There are different methods to measure capillary pressure as a function of water saturation. Some common methods are the porous plate method, centrifuge method and the mercury injection method (MICP). The method used on core plugs from the Alta West Discovery is the MICP method. The method involves injecting mercury into an evacuated and dry core sample under controlled pressures (capillary pressure). Mercury is the non-wetting phase, which forces air to be the wetting phase. The large density difference between mercury and air allows better definition of the capillary pressure curves compared with air/brine or oil/brine. The volume of mercury injected into the core at each pressure step determines the non-wetting saturation (S_{hg}). The corresponding wetting phase becomes 1-S_{hg} (McPhee et al., 2015).

The core plugs are placed in a penetrometer. As the pressure on the penetrometer increases, mercury starts to fill the pores, beginning with the pores with largest diameter. Figure 3.5 represents an example of MICP curves for a range of permeabilities and rock qualities. The y-axis is the lab original air-mercury capillary pressure defined by P_c=P_{Hg}-P_{air} and the x-axis is the wetting phase (mercury) saturation.

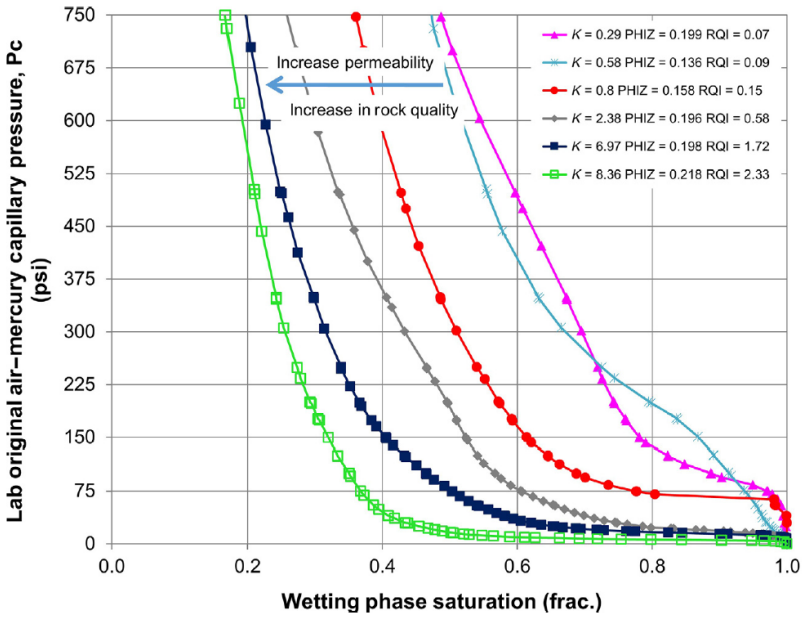

Figure 3.5: Example of mercury injection method (MICP) curves for samples of increasing permeability/rock quality. Figure from McPhee et al. (2015).

When the permeability and porosity of each core is known (determined by preferred methods), the P_c-curves can be normalized by the term $\frac{1}{\sigma \cdot cos(\theta)} \cdot \sqrt{\frac{K}{\phi}}$, yielding the j-function defined in equation 3.7. A composite plot of the J-function curves can be plotted as a function of water saturation. Figure 3.6 and 3.7 are MICP data curves from sidetrack well 2A from the Alta West Sands, illustrating how the mercury capillary pressure curves are converted into j-function curves. The equivalent water saturation on the x-axis in Figure 3.7 corresponds to 1-S_{hg}.

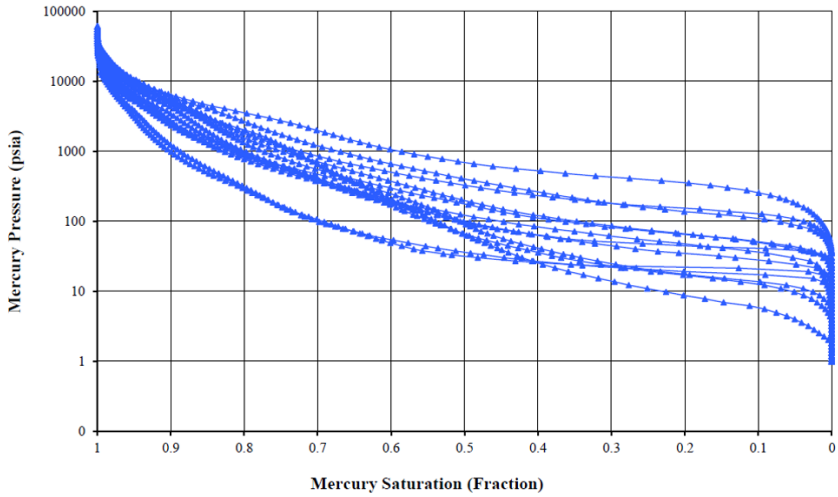

Figure 3.6: Mercury Capillary Pressure vs. Mercury Saturation from Alta West sidetrack 2A. Figure from Fazlija (2016).

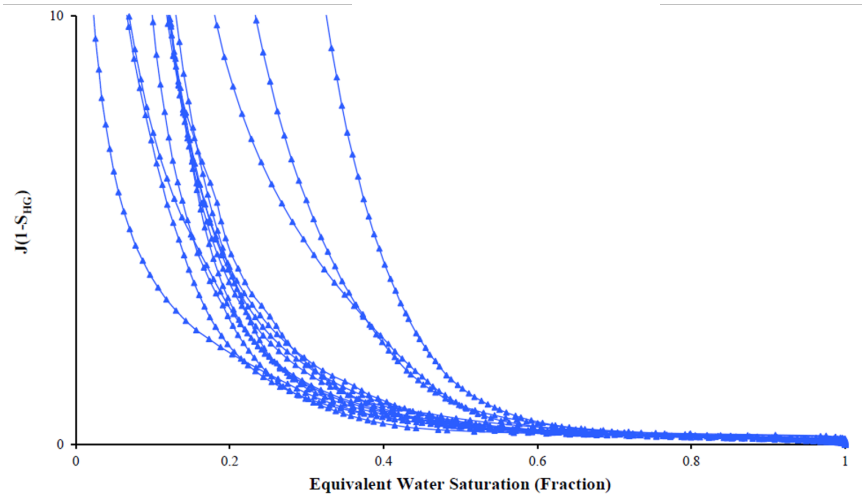

Figure 3.7: J-Leveret function vs. equivalent water saturation. MICP porosity and gas permeability is used to calculate the J-function from Alta West sidetrack 2A. Figure from Fazlija (2016).

A common practice for reservoir simulation is to select representative J-functions for each reservoir facies as input for capillary pressure data. According to Eclipse Technical Description Schlumberger (2015b), when the Leverett J-function option is activated by either the JFUNC or the JFUNCR keyword in the GRID section, the capillary pressure is

calculated as follows:

$$P_c = F \cdot J(S)$$

where J(S) is the J-function entered in place of the capillary pressure column, specified using SWOF or SGOF keyword. F is a scaling factor given by:

$$F = \sigma \cdot cos(\theta) \cdot \sqrt{\frac{\phi}{K}} \cdot U$$

where

σ = surface tension between oil/water

K = rock permeability

ϕ = rock porosity

U = constant depending on the unit system employed

θ = contact angle between oil and water

In the following section, a description of how the Leverett J-function can be used to model initial water saturation and how the oil-water capillary pressure are scaled to match the water distribution will be given.

3.3 Water Saturation Modelling

There are four initialization methods for water saturation and capillary pressure modeling depending on the available input data. Figure 3.8 is a schematic representation of the four methods. The figure illustrates which input data are necessary for the different methods and the calculated outputs from the simulator. The initial water saturation can be implemented in two ways; as an input property by using the keyword SWATINIT (method 1 and 2) or by letting the simulator calculate the water saturation for each cell by either a $P_c(S_w)$-curve (method 3) or a J(S_w)-function-curve (method 4). In this thesis, method 1 is applied for implementing the water saturation and method 2, 3, and 4 will therefore not be discussed any further.

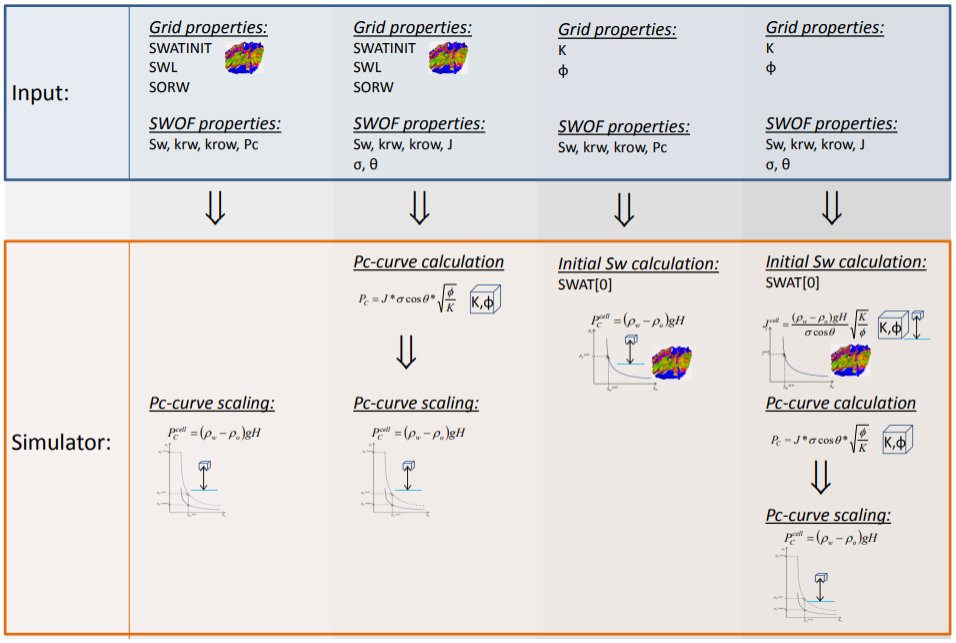

Figure 3.8: The four methods for water saturation and capillary pressure modeling. Illustration by Tijink (2018).

Method 1 is perhaps the most common method. The necessary input properties are initial water saturation for capillary pressure scaling (SWATINIT), connate water saturation (SWL) and residual oil saturation in water (SORW). In addition, oil-water relative permeability and capillary pressure as a function of water saturation is required in the saturation function table, SWOF.

SWATINIT can be calculated by a power function regression by using a representative J-function and experimental capillary pressure curves. A number of selected capillary pressure curves plotted against height above free water level is used to run the regression and to generate the following equation:

$$S_w^{init} = a \cdot J^{-\lambda} + b \tag{3.2}$$

where a, b and λ are coefficients from the regression and J is the J-function defined by equation 3.1 in the previous section 3.2. The capillary pressure in each grid cell, P_c^{cell}, from equation 3.1 is calculated from its height above free water level and densities of

the fluids:

$$P_c^{cell} = \Delta\rho_{ow} \cdot g \cdot H \tag{3.3}$$

where

$\Delta\rho_{ow}$ = difference in densities between oil and water

g = the gravitational constant

H = height above free water level

When P_c^{cell} is calculated by equation 3.3, the only unknown parameter in equation 3.2 is the initial water saturation (S_w^{init}). This implementation of SWATINIT makes S_w^{init} dependent on the grid cell's height above free water level, permeability and porosity. Figure 3.9 shows the set of selected capillary pressure curves (and J-function curves) used to generate equation 3.2 to the Alta West Sands. The dotted lines are the PC-curves and the solid lines are the Leverett J-function curves.

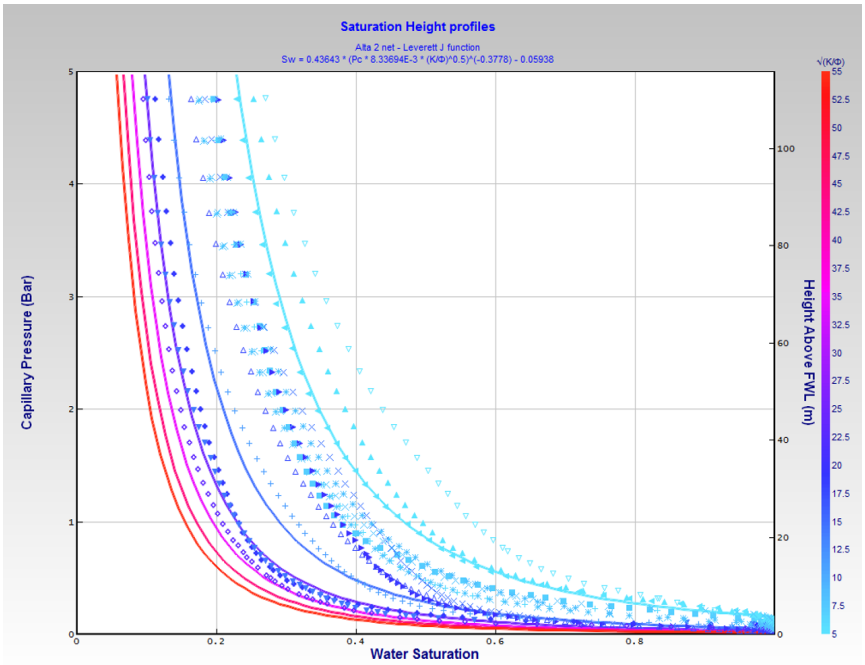

Figure 3.9: Selected capillary pressure and Leverett J-function curves vs. height used to model initial water saturation in the Alta West reservoir model.

When SWATINIT is used, the input P_c-curve is scaled to be consistent with the initial water saturation. The input-curve is scaled such that the scaled curve becomes equal to P_c^{cell} at S_w^{init}. This ensures equilibrium between gravity- and capillary forces in all grid cells. The simulator automatically calculate P_c^{cell}=P_{oil}-P_{wat} where P_{oil} is the oil phase pressure and P_{wat} is the water phase pressure. The input value will be scaled if P_{oil}-P_{wat}<0. This results in a re-scaled maximum P_c value for each cell. Figure 3.10 is an illustration of how the input P_c-curve is scaled due to SWATINIT and shows how the scaled P_c-curve results in a new P_c^{max} due to the automatically calculated P_c^{cell}.

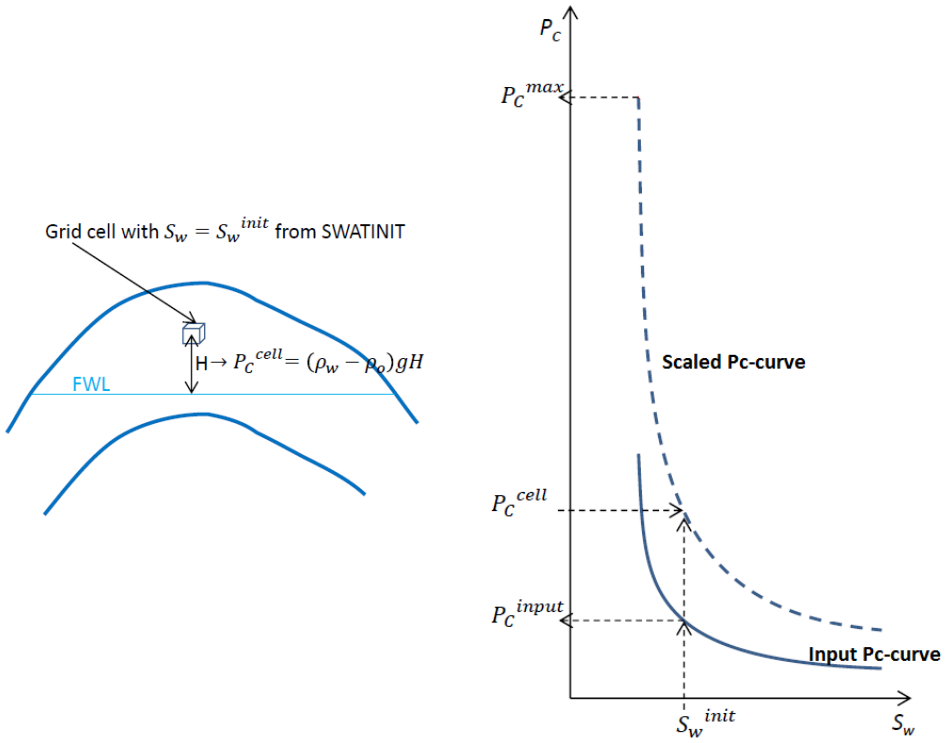

Figure 3.10: Pc-curve scaling due to SWATINIT. Illustration by Tijink (2018).

3.4 Numerical Aquifer

Aquifer modeling is a method of simulating large amounts of water connected to the reservoir for better understanding of how an aquifer affects the reservoir. There are several aquifer models such as numerical, Carter-Tracy and Fetkovich. A numerical aquifer

is applied in this study.

A numerical aquifer is modeled by a one-dimensional row of cells. The keyword AQUCON connects the first cell of the aquifer to specified grid cells (one or more) of the reservoir by non-neighbor connections. The set of cells defining the aquifer are connected together.

The keyword AQUNUM in the GRID section explicitly specifies the properties of the aquifer. The required specified properties are aquifer length, cross-sectional area, porosity, permeability, initial pressure, depth, and PVT and saturation table numbers. If the properties of the aquifer cells are defaulted, the properties are taken from the connected reservoir grid block values using data entered in the GRID and EDIT sections.

The aquifer pore volume for each cell is given by the data entered in the AQUNUM keyword (if not defaulted): $PV_i = \phi_i * L_i * A_i$, where PV_i=pore volume of cell i, ϕ_i=porosity of cell i, L_i=length of cell i and A_i=cross section area of cell i.

Chapter 4

Model Description and Deterministic Properties

The simulation model is a full-scale reservoir model supplied by Lundin Norway's Petroleum Technology department. An element model in Figure 4.1 is carved out from the complete Alta full field model. The grid is generated using Schlumberger's Petrel E&P Software and exported for dynamic simulation with Eclipse Simulator. Notice that the vertical scale is 5:1. The element model is divided into i · j · k = 50 · 21 · 120 number of grid blocks. Figure 4.2 with view from above illustrates the variations in grid size. The largest outer grid blocks have dimensions of $40 \cdot 77 \cdot 1$ m^3 and the finer grids in the middle of the model have dimensions of $40 \cdot 15 \cdot 1$ m^3. All production wells are located in the finer grids to enhance the significance of production performance and reduce numerical dispersion.

Table 4.1 lists the rock and fluid properties of the reservoir model. A numerical aquifer in Figure 4.3 is connected to the element model from west and below the water zone by non-neighbor connections. The fluid properties and the saturation functions are identical to the properties of the element model. The size of the aquifer and the average permeability and porosity are listed in Table 4.2.

Three development strategies are to be studied; gas injection, water injection and pressure depletion. Two wells are included in the development strategies for gas and water injection; one horizontal producer and one injector. The locations of the wells change in accordance with the secondary recovery method chosen, with gas injector in the gas zone and water injector in the water zone. The production wells are constrained to the same limits in the three development strategies, given in Table 4.3 and the injection wells are constrained to the limits listed in Table 4.4.

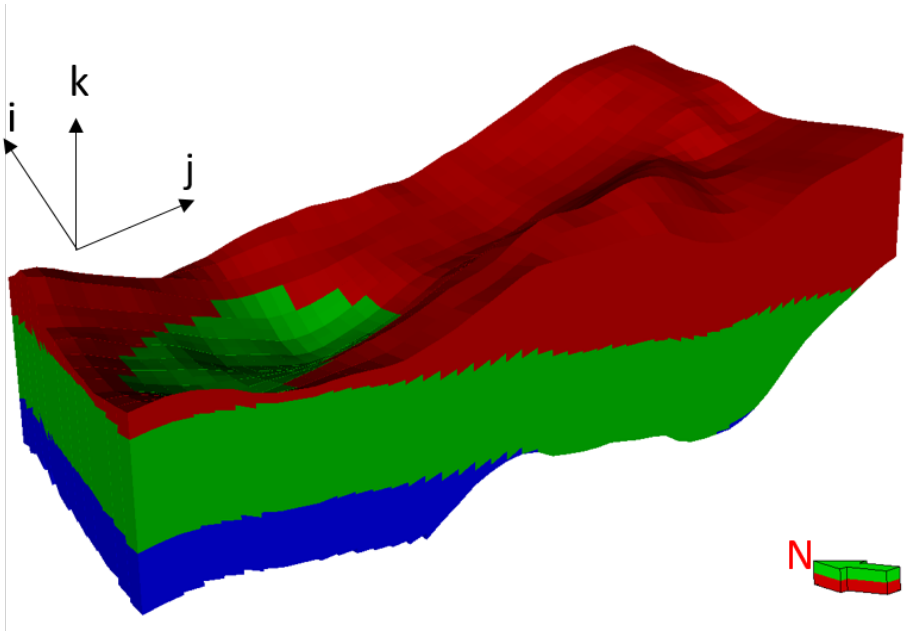

Figure 4.1: The element model carved out from the complete Alta full-field model, illustrating the water, oil and gas phases. Vertical scale: 5:1.

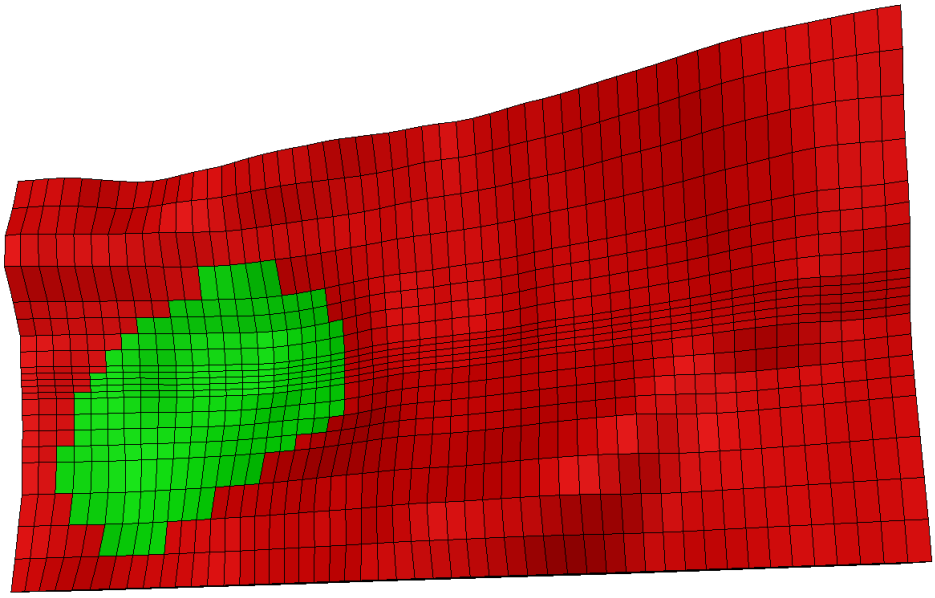

Figure 4.2: Top view of the element model illustrating the finer grids in the middle of the model.

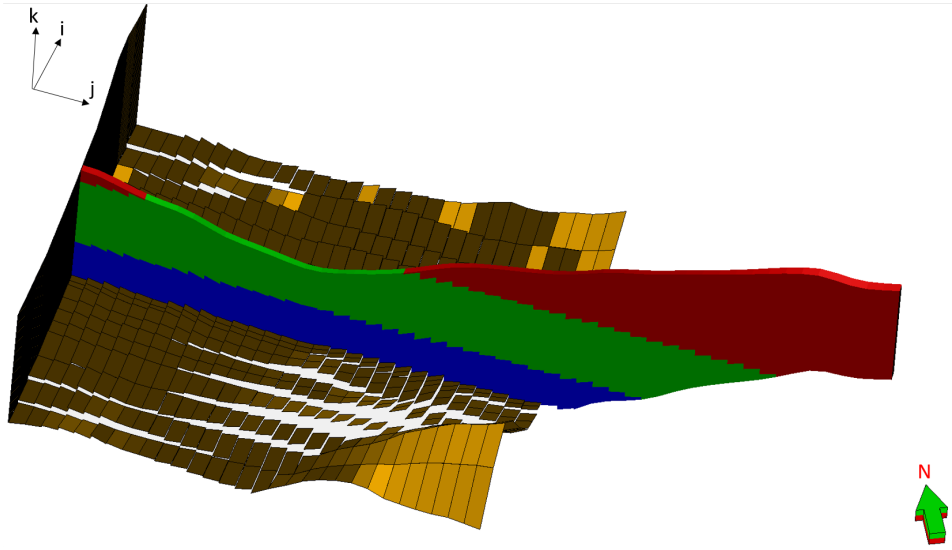

Figure 4.3: Numerical aquifer in the j-i plane and the k-i plane connected to the reservoir model from west and below the water zone. A cross sectional area in the j-k plane is sectioned out from the element model. The numerical aquifer is illustrated as the grid blocks not colored red, green or blue. Vertical scale: 5:1.

Table 4.1: Rock and fluid properties.

Values given at P_{ref}		
Property	**Value**	**Unit**
P_{ref} @ GOR	196.6	$barsa$
μ_w	0,686	cP
μ_o	0,444	cP
μ_g	0,020	cp
ρ_w	1168,7	kg/m^3
ρ_o	826,3	kg/m^3
ρ_g	0.939	kg/m^3
B_w	1,018	rm^3/Sm^3
B_{oi}	1,352	rm^3/Sm^3
B_g	0,006	rm^3/Sm^3
R_{soi}	114,24	Sm^3/Sm^3
S_{wcr}	0.19	fraction

Table 4.2: Aquifer size and rock properties.

Property	**Value**	**Unit**
Number of cells	1	-
Permeability	30	mD
Porosity	0.1	-
Cross sectional area	10	km^2
Length	4	km

Table 4.3: Production well limits.

Production Well Control Data					**Economic limits**		
Oil Rate	BHP	Gas Rate	Water Rate	Liq. Rate	Min. Oil Rate	Water Cut*	GOR*
(Sm^3/d)	($barsa$)	(Sm^3/d)	(Sm^3/d)	(Sm^3/d)	(Sm^3/d)	(%)	(Sm^3/Sm^3)
400	100	1 000 000	No Limit	800	70	95	3000
**Close well*							
BHP=Bottom Hole Pressure							
GOR=Gas Oil Ratio							

Table 4.4: Injection well limits.

Water Injector, Well Control Data		
BHP	Voidage Rate*	Max. Surface Rate
$(barsa)$	$(fraction)$	(Sm^3/d)
400	1*	2000
Gas Injector, Well Control Data		
BHP	*Re-injection Rate***	
$(barsa)$	$(fraction)$	
300	1**	
*The field reservoir volume injection is controlled so that it equals the field production voidage rate, with maximum limit set to 2000 $Sm^3/day		
**The field gas production rate is re-injected to the reservoir		

Three reference cases, one for each development strategy, are defined to analyze which recovery method is most efficient. The three reference cases are deterministic cases initiated with the most likely reservoir properties and saturation functions. The only factor separating the strategies are the location of the injector and producer. Their locations are optimized by an operational sensitivity study described in the next chapter. The results from the operational study are tested against the optimized reference case with the properties and strategies described in the following sections.

Facies sectioning

The reservoir model is divided into five facies reflecting the actual Alta West reservoir. Figure 4.4 illustrates the reservoir zonation for which porosity vs. permeability correlations are assign. The porosity-permeability correlation for each facies is given in Figure 4.5. The reservoir quality is poor with low deterministic average horizontal permeability and with vertical permeability only 5% of the horizontal. The deterministic average porosity is also low with a value of 13%. Figure 4.6 demonstrates the horizontal permeability distribution for the cross sectional area in J-direction where the production wells are located. Notice that the color legend only ranges from zero mD to 10 mD to highlight the high permeability layer in the middle of the section.

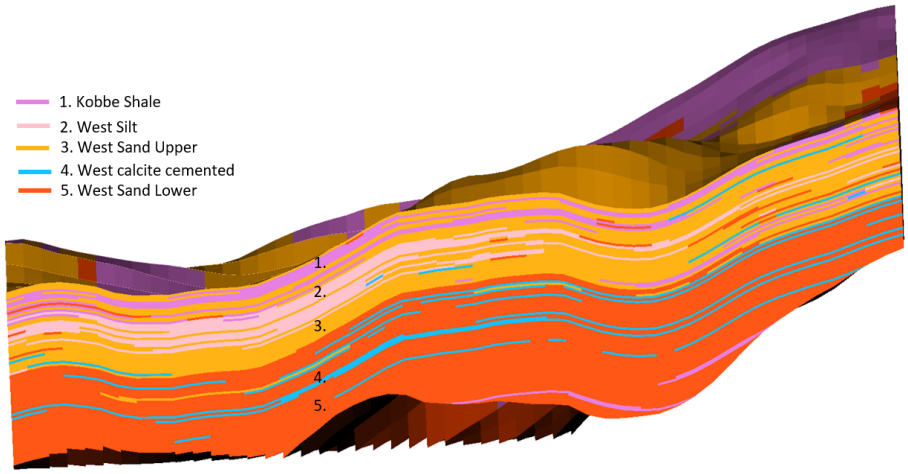

Figure 4.4: Schematic figure illustrating the facies in the reservoir model. The porosity vs. perm of the 5 facies are given in Figure 4.5.

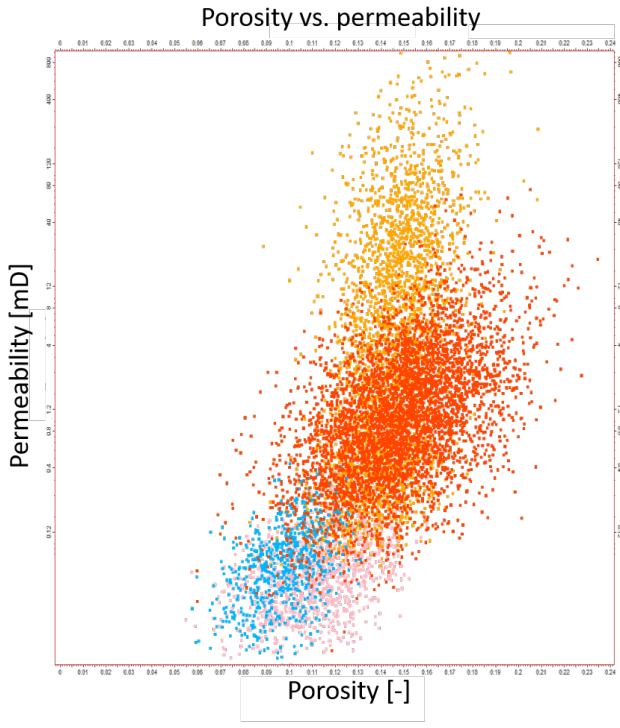

Figure 4.5: porosity-permeability correlations of the facies given in Figure 4.4, excluding the Kobbe Shale.

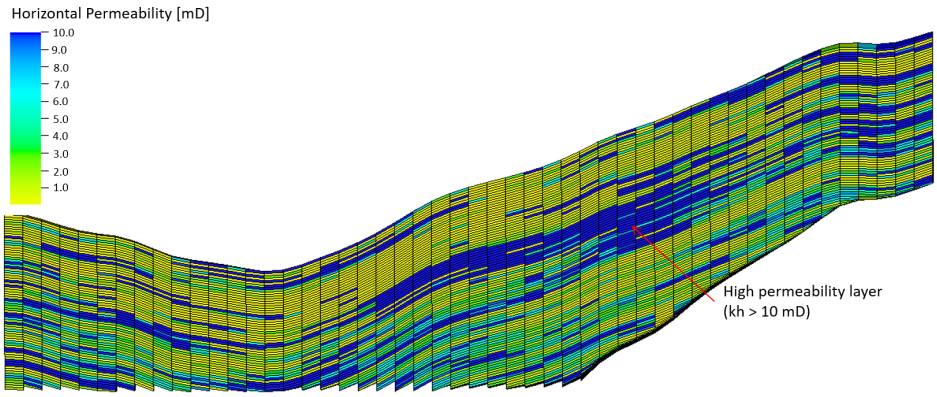

Figure 4.6: Deterministic horizontal permeability distribution for a cross sectional area in J=11. Average permeability is 40 mD, but the color legend ranges from zero mD to 10 mD.

Deterministic Saturation Functions

All test systems are initiated with identical saturation functions. The deterministic relative permeability curves are derived by the LET-correlation, described in section 2.3.1, with the end-points and LET parameters given in Table 4.5. A comparison between simulation runs with Modified Brooks and Corey and LET relative permeability curves is conducted and proves minor effects on oil recovery. The resulting LET-curves are illustrated in linear scale in Figure 4.7 and 4.8. The point of intersection on the water saturation axis of the two permeability curves indicates that the wetting preference of the rock surface is slightly more water-wet. If the curves cross at $S_w > 0,5$, the point of intersection implies water-wet system (Fanchi, 2000).

The gas-oil capillary pressure (P_{cog}) is set to zero, and the deterministic oil-water capillary pressure (P_{cow}) is given in Figure 4.9. The saturation model presented by Brooks and Corey (1996) derives the curve, which correlates normalized oil saturation to capillary pressure and entry pressure. The entry pressure is 0.05 bar and the maximum capillary pressure is 1 bar. Hysteresis is not included in neither of the simulation cases in this study, meaning that drainage and imbibition processes follow the same path of saturation change for both capillary pressure and relative permeability curves.

Table 4.5: Saturation function end-points and LET parameters.

Oil-water system									
L_w^o	E_w^o	T_w^o	L_o^w	E_o^w	T_o^w	$S_{wcr} = S_{wir}$	S_{orw}	$K_{rw}(S_{orw})$	$K_{row}(S_{wir})$
3,0	3,5	1,5	2,0	8,0	1,9	0,19	0,2	0,6	1
Gas-oil system									
L_g^o	E_g^o	T_g^o	L_o^g	E_o^g	T_o^g	S_{gcr}	S_{org}	$K_{rg}(S_{org})$	$K_{rg}(S_{wir})$
2,6	1,6	0,8	1,2	3,4	1,6	0,05	0,15	0,7	1,0

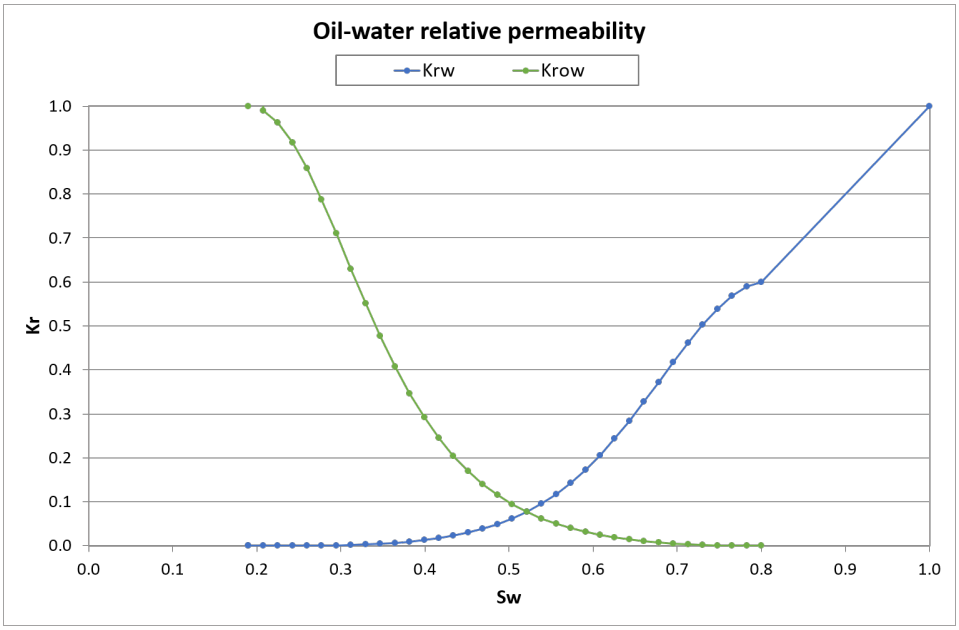

Figure 4.7: Imbibition oil-water relative permeability vs. water saturation applied in the deterministic reference cases.

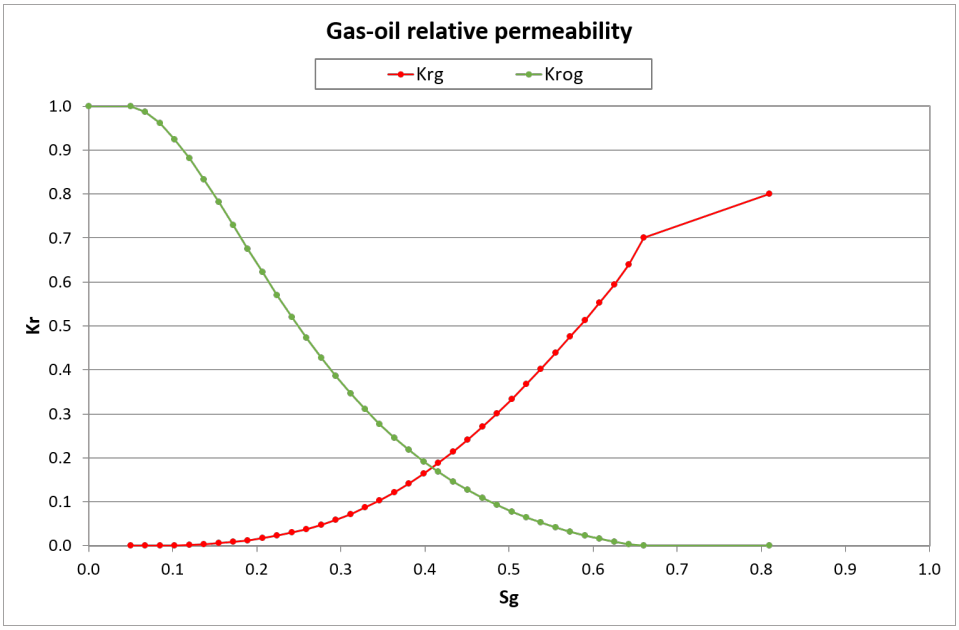

Figure 4.8: Imbibition gas-oil relative permeability vs. gas saturation applied in the deterministic reference cases.

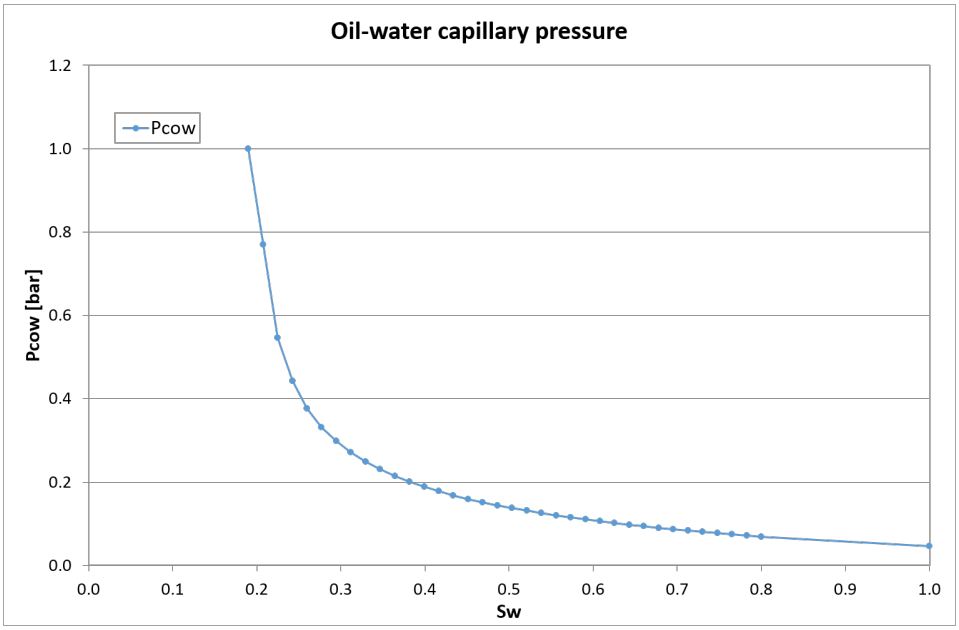

Figure 4.9: Drainage oil-water capillary pressure curve vs. water saturation.

The Leverett J-function method described in Section 3.3 estimates the resulting initial water saturation (SWATINIT) in Figure 4.10. It is calculated by a Petrel workflow based on look-up functions with tabulated values of the J-function and equivalent water saturation. The J-function is calculated based on the porosity, permeability and height above water contact for each grid block. Figure 4.11 is a quality check of initial water saturation and saturation well log.

To make the saturation function curves consistent with the initial water saturation, the ENDSCALE option is applied. The required connate water saturation is calculated with the same J-function based on a fixed height of 80 meters above water contact. Figure B.1 in Appendix B represents the Petrel workflow to generate the initial water saturation, connate water saturation and the required saturation end-points.

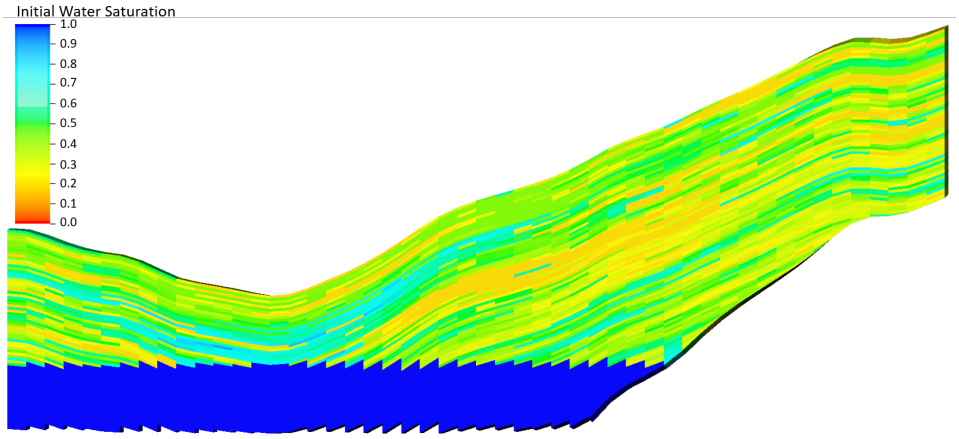

Figure 4.10: Deterministic initial water saturation distribution in cross sectional area J=11.

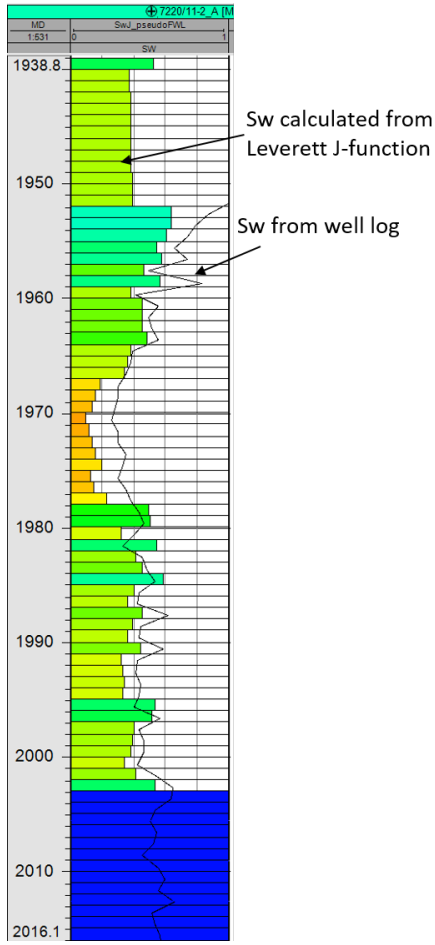

Figure 4.11: Deterministic up-scaled initial water saturation (S_{wi}) in the well bore compared with water saturation from well log. S_{wi} is derived from the Leverett J-function. Notice that well log has measured S_{wi} less than 100% below the oil-water contact. It is believed to be due to reservoir uplift and resulting residual oil saturation.

Development Strategies

Figure 4.12 illustrates the horizontal production wells "PO_HIGH" and "PO_LOW". Described in the next chapter, the optimal well location for the gas injection strategy is "PO_LOW". Well "PO_HIGH" is optimal for the water- and pressure depletion strategy. The wells have perforations through the entire horizontal interval. The vertical distance between the wells are 10 meter and the optimization reduces the effects of coning.

The injection wells in Figure 4.13 are located in the cross sectional area J=1, in the outer grid blocks of the reservoir model. The chosen location is an attempt to delay water- and gas breakthrough and to maintain reservoir pressure. The water injector, "WI_J1", has perforations in the water zone and the gas injector, "GI_J1", has perforations in the gas zone. The wells start to inject water/gas from start of production.

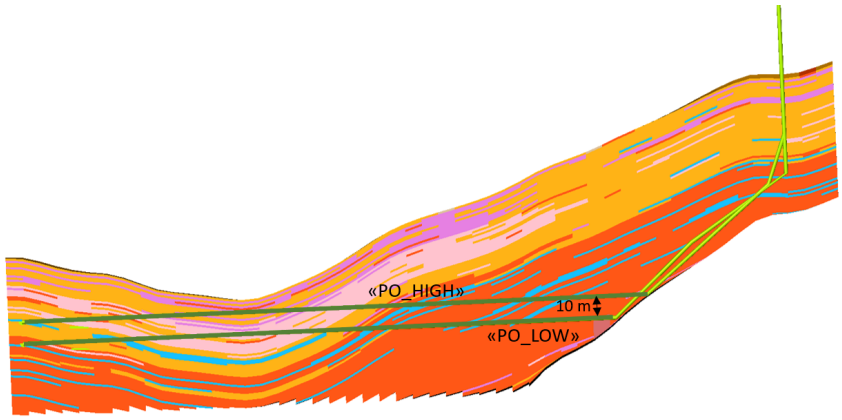

Figure 4.12: Production wells and perforated zones (dark green) located in cross sectional area J=11. Both wells are perforated through the entire horizontal interval. Well "PO_HIGH" and its perforations are optimal for water injection and pressure depletion strategies. Well "PO_LOW" and its perforations are optimal for the gas injection strategy.

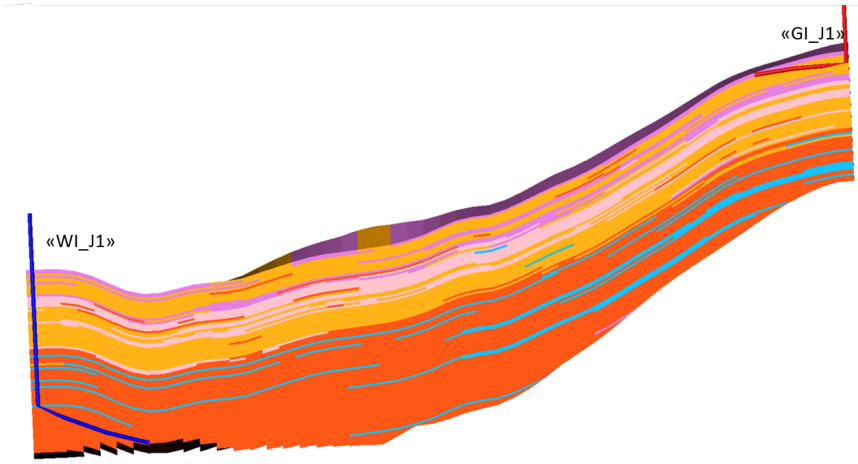

Figure 4.13: Injection wells located in cross sectional area J=1. "WI_J1" is the water injector and "GI_J1" is the gas injector.

Chapter 5

Results

Figure 5.1 illustrates the workflow for the complete uncertainty risk analysis to provide a recommendation of best recovery method. A deterministic simulation case with the most likely grid properties, one for each development strategy, are carried out by an operational sensitivity study, and represents the reference case in the sensitivity study. All properties included in the sensitivity study are divided into high, mid and low values where the mid values represent the most likely properties in the reference case. The results from the sensitivity study are illustrated in tornado charts, which present the cumulative oil production relative to the reference case. The most critical parameters from the tornado charts are carried forward to the uncertainty analysis to generate P90, P50 and P10 models in order to give a recommendation of best recovery method.

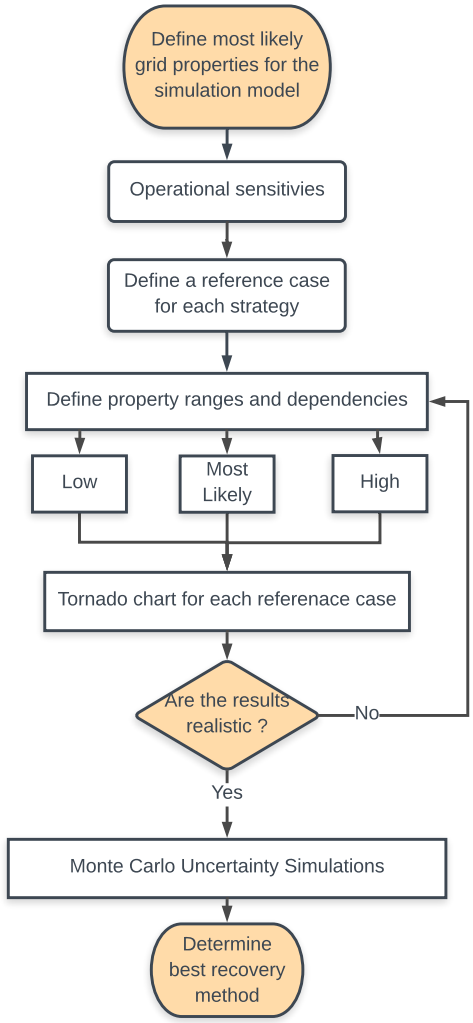

Figure 5.1: The workflow for the sensitivity and uncertainty analysis.

5.1 Operational Sensitivities and Reference Case Results

The three development strategies are simulated 30 years. However, the oil production economic limit is considered 70 Sm^3/day and the final results from the reference cases summarized in Table 5.4 are according to this limit. Notice that the discounted oil production is present value in oil [MSm^3] and not a currency, with a discount rate of 10%. The reference cases are tested against the operational sensitivities including:

- Vertical well
- High/low horizontal well
- Perforation intervals
- High/low oil production rates
- Injection well shut

The various oil production rates are 200, 400 and 1500 Sm^3/day where 400 Sm^3/day is used in the reference cases. Two perforation scenarios are carried out. Scenario #1 is perforations through the entire horizontal interval and scenario #2 is perforations in the entire horizontal interval except the high permeable layer illustrated in Figure 4.6 in the previous chapter. Scenario #1 is applied in the reference case. Four different production wells are included in the operational sensitivity study. Each development strategy compares the effects from one vertical well and one horizontal well, named "PO_MID", located between the two wells described in Figure 4.12. The well locations in the different strategies are also described in Figure 4.12.

Gas Injection Strategy

Table 5.1: Simulation results from the reference case to the gas injection strategy after economic oil rate limit is reached.

Reference Case Results - Gas Injection Strategy		
Time(oil rate <70 Sm^3/d)	16,2	years
STOOIP	3,7	MSm^3
Produced oil	0,86	MSm^3
Produced gas	1141	MSm^3
Solution gas	0,015	MSm^3
Produced water	0,64	MSm^3
Discounted oil production	0,52	MSm^3
Recovery factor	23	%

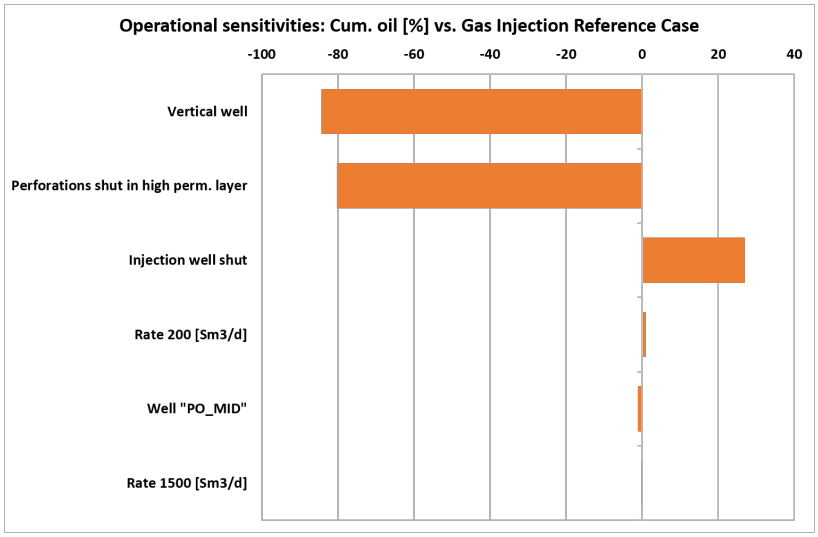

Figure 5.2: Tornado chart illustrating deviation (%) in cumulative oil production at time when oil production is below 70 Sm^3/day between the operational sensitivities and gas injection reference case.

Table 5.1 presents the final results from the reference case for the gas injection strategy. The time at shut in is according to the oil production economic limit of 70 Sm^3/day. Figure 5.2 presents the tornado chart for the gas injection strategy illustrating the operational sensitivities relative to the reference case.

The sensitivities with greatest influence on cumulative oil production are vertical well and perforation intervals. The sensitivity with vertical well has -80% influence on cumulative oil production. As illustrated in the chart, the sensitivity without gas injection is the only sensitivity with significant positive influence on cumulative oil production.

Figure 5.3 and Figure 5.4 show results for gas-oil ratio and oil production rate after 12 years of production from simulations with various oil rates and well "PO_MID". Well "PO_MID" (higher horizontal well) has only minor effects on cumulative oil production, but the effects on gas rate are significant. The resulting gas-oil ratio (GOR) at time when oil production is below 70 Sm^3/day is 5250 Sm^3/Sm^3 compared to the reference case with 3440 Sm^3/Sm^3. Similarly, oil production rates have minor effects on cumulative oil production, but there are other factors contributing to less efficient scenarios relative to

the reference case. Oil rate with 1500 Sm^3/day has only -0,3 % influence on cumulative oil production, but it has no production plateau indicating that the gas front is unstable. The consequence is viscous fingering and early gas break-through. Oil rate with 200 Sm^3/day is +1% compared to the reference case. However, the discounted oil rate is 0,49 MSm^3 compared to the reference case with 0,52 Sm^3/day which indicates that the reference case is favorable.

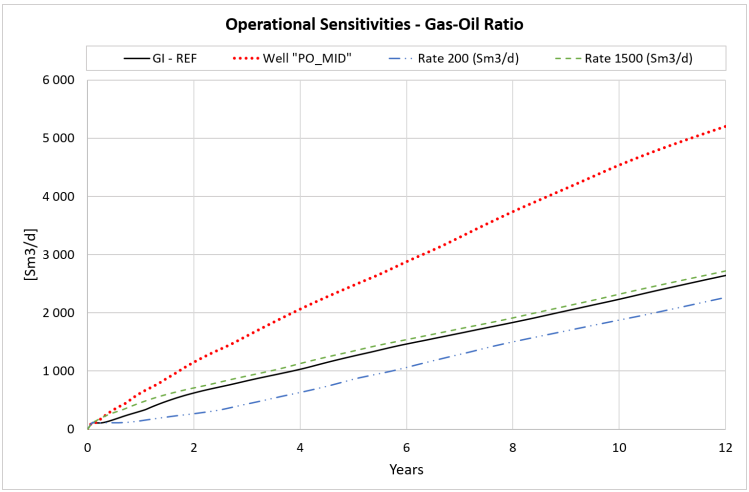

Figure 5.3: Gas injection sensitivity study: comparison of gas-oil ratio from production rates 1500, 400 (GI-REF) and 200 Sm^3/day and well "PO_MID".

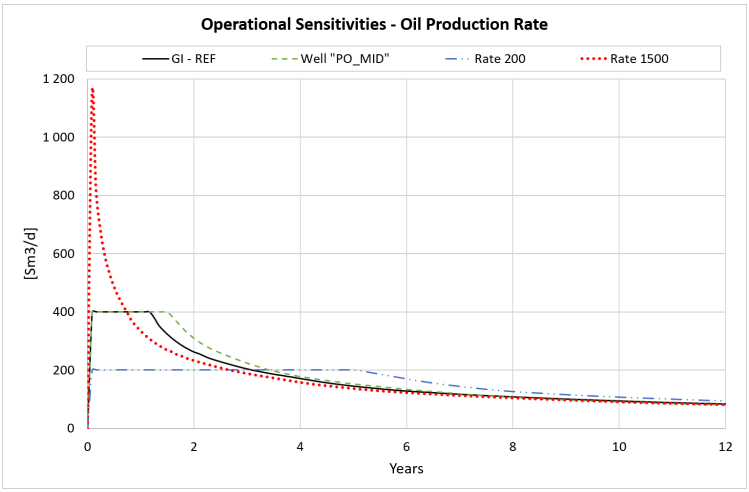

Figure 5.4: Gas injection sensitivity study: comparison of oil production rate from simulations with production rates 1500, 400 (GI-REF) and 200 Sm^3/day and well "PO_MID".

Water Injection Strategy

Table 5.2: Simulation results from the water injection reference case after economic oil rate limit is reached.

Reference Case Results - Water Injection Strategy		
Time(oil rate <70 Sm^3/d)	15,1	years
STOOIP	3,7	MSm^3
Oil produced	1,1	MSm^3
Gas produced	2721	MSm^3
Solution gas	0,27	MSm^3
Water produced	1,2	MSm^3
Discounted oil production	0,70	MSm^3
Recovery factor	30	%

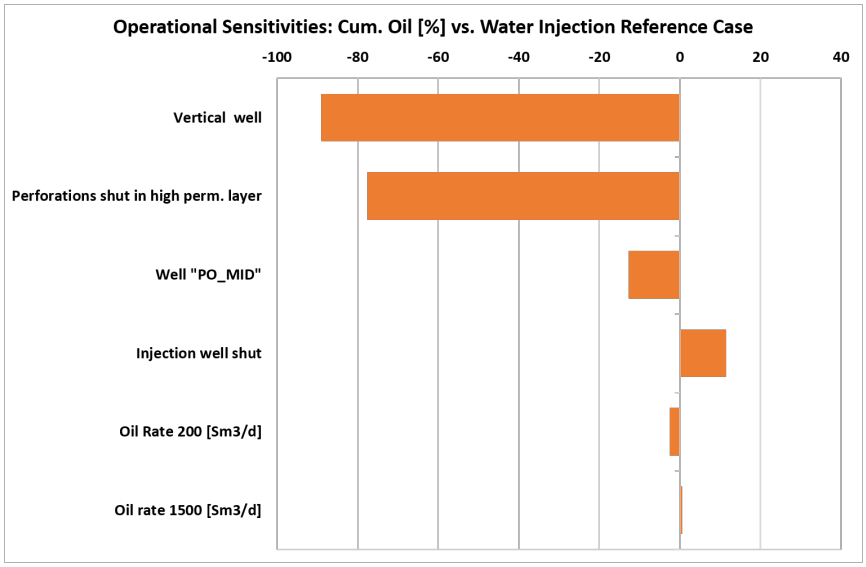

Figure 5.5: Tornado chart illustrating deviation (%) in cumulative oil production at time when oil production is below 70 Sm^3/day between the operational sensitivities and water injection reference case.

Table 5.1 presents the final results from the reference case for the water injection strategy. Similar to the gas injection strategy, the time at shut in is according to the oil pro-

duction economic limit of 70 Sm^3/day. Figure 5.2 presents the tornado chart for the gas injection strategy illustrating the operational sensitivities relative to the reference case.

The influence on cumulative oil production from the operational sensitivities relative to the reference case are similar to the gas injection strategy. Vertical well and perforated intervals are the most influential sensitivities while oil rates and height of the horizontal well has only minor influence on the cumulative oil production. Also similar to the gas injection strategy, the case without an injector yields greater cumulative oil production.

Pressure Depletion Strategy

Table 5.3: Simulation results from the pressure depletion reference case after economic oil rate limit is reached.

Reference Case Results - Pressure Depletion Strategy		
Time @ oil rate <70 Sm^3/d	15,1	years
STOOIP	3,7	MSm^3
Oil produced	1,22	MSm^3
Gas produced	3223	MSm^3
Solution gas	0,32	MSm^3
Water produced	1,4	MSm^3
Discounted oil production	0,70	MSm^3
Recovery factor	33	%

Table 5.3 summarizes the results from the final reference case for the pressure depletion strategy according to the oil production economic limit and Figure 5.5 illustrates the operational sensitivities relative to the reference case. Notice that the operational sensitivities differ from the two other strategies. Instead of running a case with the injector shut, two cases with well "PO_LOW" and "PO_MID" are included. The effects of the two wells on cumulative oil production are almost identical.

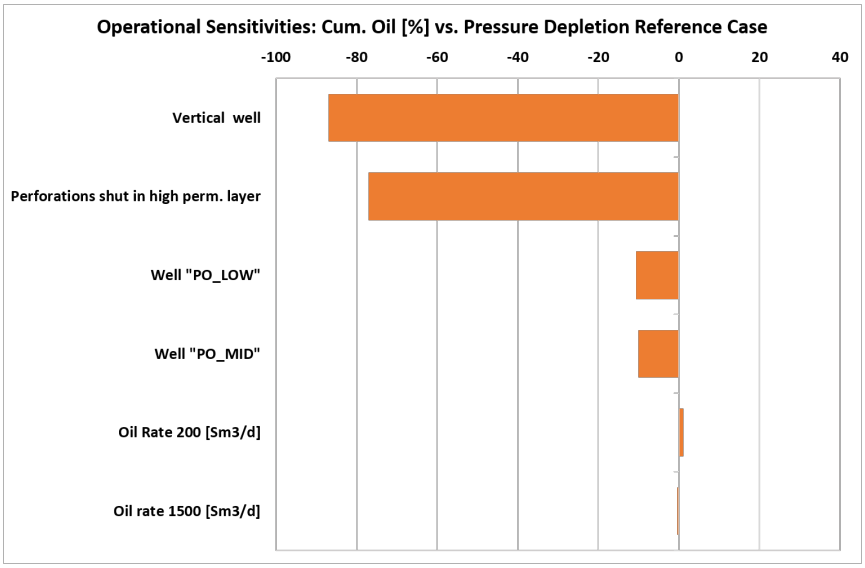

Figure 5.6: Tornado chart illustrating deviation (%) in cumulative oil production at time when oil production is below 70 Sm^3/day between the operational sensitivities and pressure depletion reference case.

Similar to the other development strategies, the most influential operational sensitivities are vertical well and perforated intervals. The case with oil rate at 200 Sm^3/day has slightly higher cumulative oil production. However, the low production rate yields low discounted oil production of 0,57 MSm^3 which is -19% relative to the reference case.

Comparison of the Development Strategies

Table 5.4 compares the simulation results from the three development strategies when economic oil rate is included. Figure 5.7, 5.8 and 5.9 are simulation results after 30 years of production. The water injection strategy shuts in after 28 years when the water cut (WC) exceeds 95%.

The results indicate that the most efficient recovery method is the pressure depletion strategy. This assumption is solely based on best recovery factor and operational sensitivities.

Table 5.4: Comparison of the three reference cases. The results are from the time when oil production reach economic limit of 70 Sm^3/day.

Reference Case:	Gas Injection	Water Injection	Pressure Depletion
Time at shut in (years)	16,2	15,1	15,1
STOOIP (MSm^3)	3,7	3,7	3,7
Oil produced (MSm^3)	0,86	1,1	1,22
Gas produced (MSm^3)	1141	2721	3223
Solution gas (MSm^3)	0,015	0,27	0,32
Water produced (MSm^3)	0,64	1,2	1,4
Discounted oil production (MSm^3)	0,52	0,70	0,70
Recovery factor (%)	23	30	33

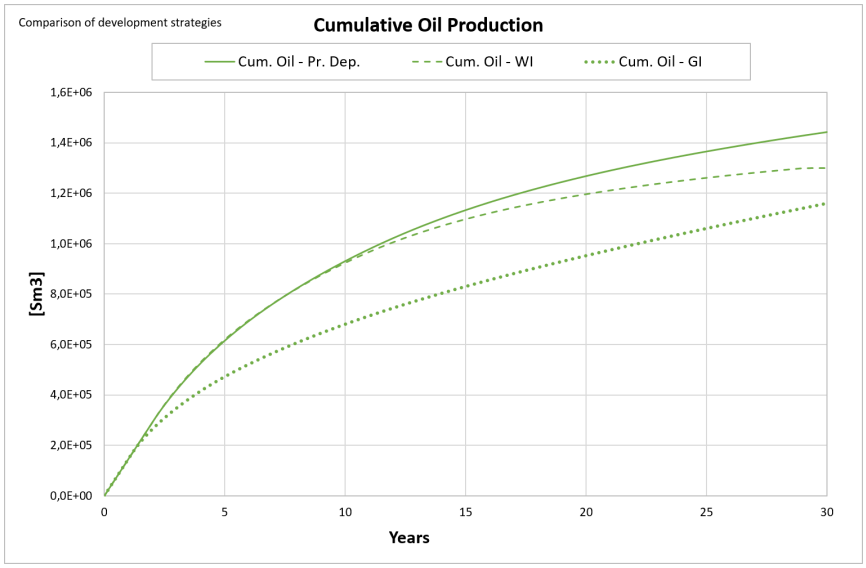

Figure 5.7: Comparison of cumulative oil production between the gas injection (GI), water injection (WI), and pressure depletion (Pr. Dep.) reference case after 30 years of production.

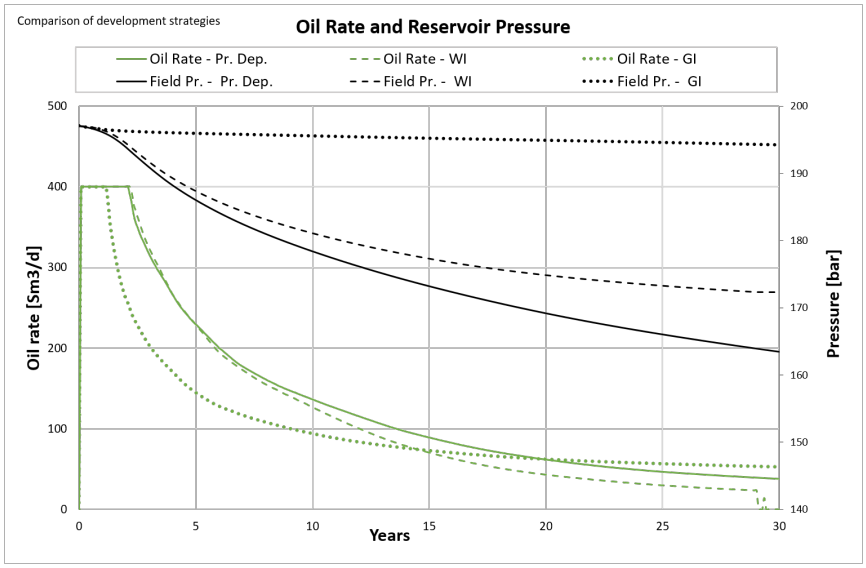

Figure 5.8: Comparison of oil rate and reservoir pressure between the gas injection (GI), water injection (WI), and pressure depletion (Pr. Dep.) reference case after 30 years of production.

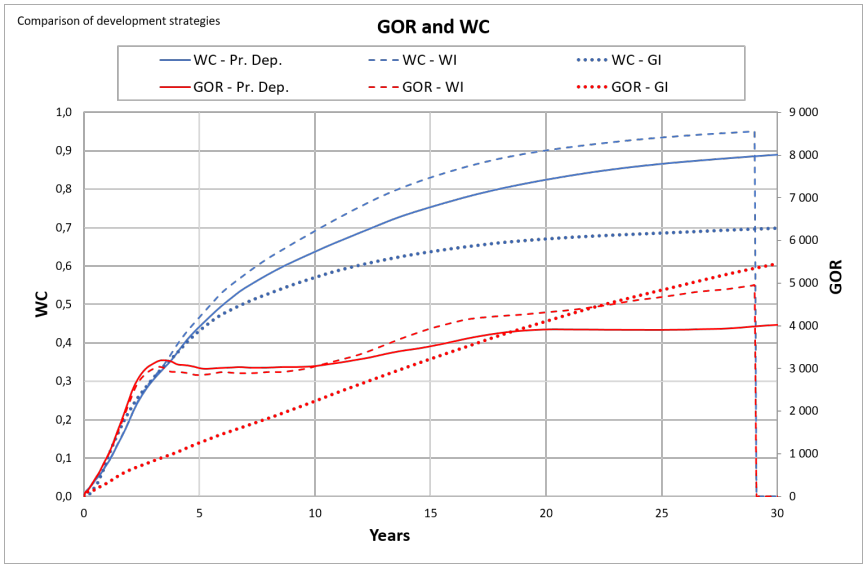

Figure 5.9: Comparison of gas-oil ratio and water-cut between the gas injection (GI), water injection (WI), and pressure depletion (Pr. Dep.) reference case after 30 years of production.

5.2 Sensitivity Study and Results

Chosen Sensitivities and Their Range

In this section, the parameter variations and its influence on reservoir behavior within each sensitivity are analyzed. The chosen sensitivities are assumed most uncertain for the Alta West reservoir and the main focus for the sensitivity study is to analyze the dominating drive mechanisms.

Regardless the number of sensitivities included in the sensitivity study, some essential parameters are neglected. For simplicity, the initial water saturation, which is a function of porosity and permeability, is assumed constant throughout the whole sensitivity study. Even though the initial water saturation alters with variations in rock properties, the assumption is considered reasonable because the quality check against water saturation well log proved good match.

Capillary pressure uncertainties are also neglected in this sensitivity study. However, capillary pressure influences the wettability preference of the surface rock and is a direct input of the Leverett J-function, and hence affects the in-situ fluids. The capillary pressure curve is assumed insignificant for this sensitivity study since the initial water saturation is assumed constant and will not be influenced by capillary pressure variations.

Another essential sensitivity that is not included is reservoir faults. Even though the influence from faults may be critical to the field development, it is neglected because it was not the main focus in this thesis. The following sections will describe the chosen sensitivities, their range and the resulting influence relative to the deterministic reference case for each development strategy.

Permeability, k_v/k_h-ratio and Porosity

The porosity and permeability range are based on core measurements and well tests. The two parameters show great correlation in the poro-perm plot in Figure 4.5 and a

dependency in the uncertainty study should therefore be included. However, an independent analysis of each parameter will enhance the influence of each parameter on production performance.

The productivity and injectivity of the wells are linear functions of the permeability (Dake, 1978) and the permeability is therefore critical for the length of the plateau and pressure support from the water injector. In addition, the permeability distribution influences the vertical sweep efficiency, which makes permeability critical for the water and gas drive efficiency. Therefore, the full range from the core measurements and the well test range has been included in order to cover all possible scenarios.

Porosity and Permeability are one of the most critical uncertainty parameters as they are direct input parameters to the water saturation calculations using the Leverett J-function. Consequently, they are critical factors for the STOOIP uncertainty range. However, since initial water saturation uncertainty is neglected, porosity is the only parameter affecting the STOOIP, as it is a direct input to the reservoir pore volume calculations.

The k_v/k_h-ratio is highly uncertain as there are no vertical permeability measurements conducted on the Alta West reservoir. The vertical permeability distribution influence the vertical sweep efficiency, which makes the k_v/k_h-ratio critical to the production plateau.

Table 5.5 lists the porosity, k_v/k_h-ratio and permeability range. The middle value represents the most likely value from the reference case. The horizontal permeability is multiplied by a factor of 3 while the porosity range is set to -2% to +2 % relative to the reference case. The k_v/k_h-ratio multiplication factor is 10%, which yields a range of 0,005 to 0,5.

Table 5.5: Permeability, porosity and k_v/k_h-ratio sensitivity range.

Parameter	**Low**	**Mid**	**High**
Avg. Permeability (mD) $(\div 3, *3)$	13	39	117
Avg. Porosity (%) (-2%, +2%)	10,9	12,9	14,9
k_v/k_h-ratio (-) $(*0,1, \div 0,1)$	0,005	0,05	0,5

Relative Permeability

The relative permeability parameter has great influence on the displacement efficiency and is a great uncertainty since directly measurements of the parameter is not conducted. The uncertainty range is based on a literature study on relative permeability dependencies by McPhee et al. (2015) and Schön (2015).

The relative permeability parameter range is defined by three curves, representing high case, reference case and low case. Figure 5.10 illustrates the range for oil-water relative permeability and Figure 5.12 for gas-oil relative permeability. The oil-water curves represent wettability uncertainty, where the controlling factors are: 1) the intersection point on the water saturation axis of the permeability curves, 2) residual oil saturation (S_{or}) and 3) the value of relative permeability at the end-point saturations ($k_r^{'}$) (Fanchi, 2000). There are dependencies between S_{or} and $k_{rw}^{'}(S_{or})$. In general, high S_{or} indicates oil-wet system and results in high $k_{rw}^{'}(S_{or})$. Table 5.6 shows the LET-parameters and the end-point dependencies for the three cases.

The fractional flow curves in Figure 5.11 illustrate the effects on oil recovery by changing the relative permeability curves. The calculated recovery factors at water breakthrough is shown in Table 5.6.

Table 5.6: Saturation function end points and LET-parameters for low, mid and high relative permeability curves.

Oil-Water System									
	L_w^o	E_w^o	T_w^o	L_o^w	E_o^w	T_o^w	S_{orw}	$K_{rw}(S_{orw})$	RF @ BT*
Low	2,4	3,5	1,7	3,0	7,0	1,5	0,25	0,7	0,48
BC	3,0	3,5	1,5	2,0	8,0	1,9	0,20	0,6	0,6
High	4,0	3,5	1,3	1,0	9,0	2,3	0,15	0,5	0,77
*) RF @ BT=Recovery factor at water breaktrough estimated from fw-curves in Figure 5.11									
Gas-Oil System									
	L_g^o	E_g^o	T_g^o	L_o^g	E_o^g	T_o^g	S_{org}	$K_{rg}(S_{orw})$	
Low	2,2	1,3	0,7	1,8	3,8	1,5	0,20	0,7	
BC	2,6	1,6	0,8	1,2	3,4	1,6	0,15	0,7	
High	3,2	2,0	0,9	1,0	3,0	1,8	0,10	0,7	

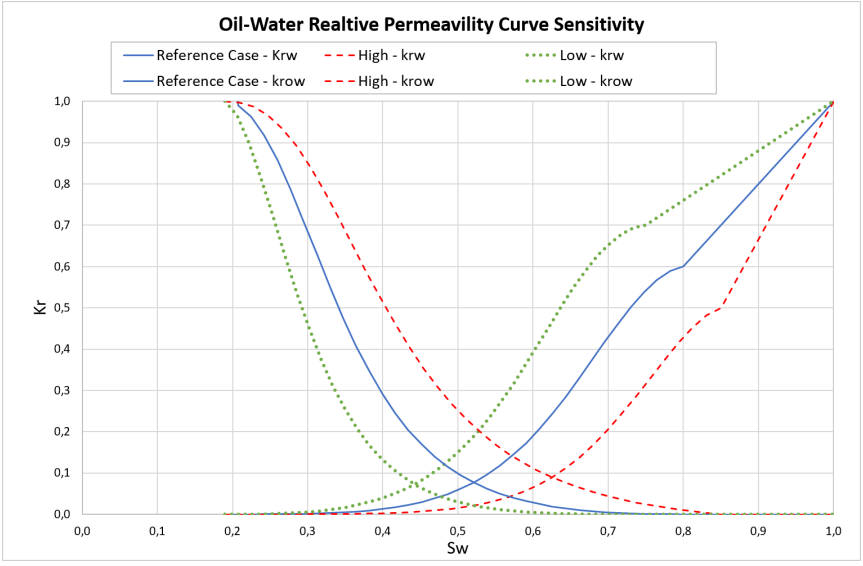

Figure 5.10: Oil-water relative permeability curves for low/oil-wet case, reference case and high/water-wet case.

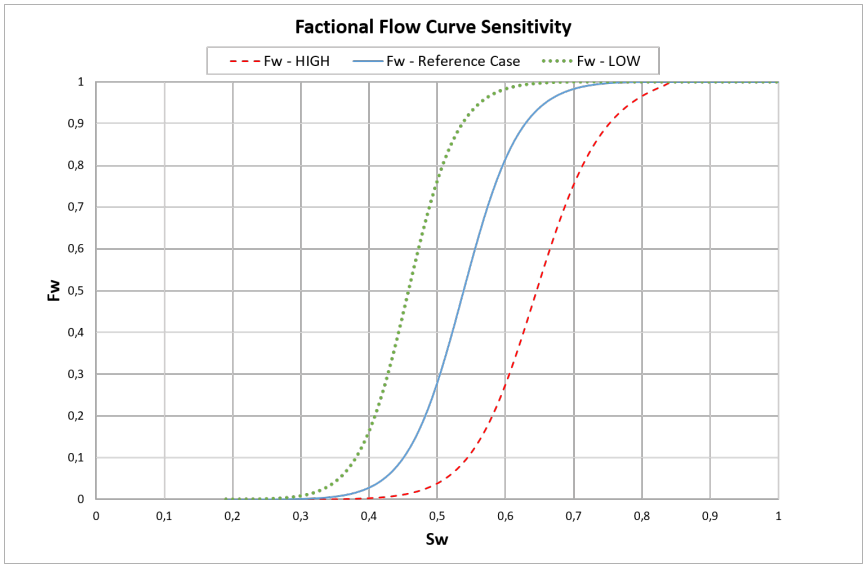

Figure 5.11: Fractional flow curves for low/oil-wet case, reference case and high/water-wet case.

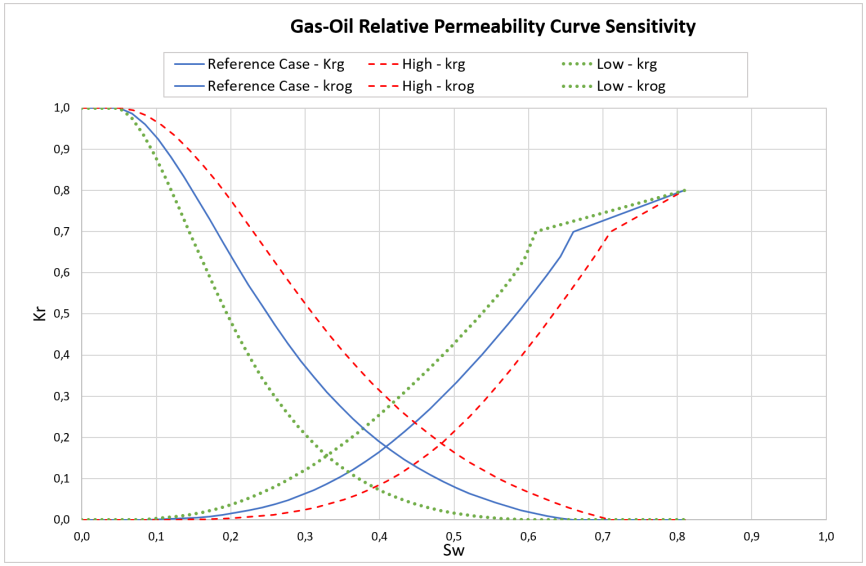

Figure 5.12: Gas-oil relative permeability curves for low, reference case and high case.

Oil Viscosity and Oil Formation Volume Factor

The oil formation volume factor (B_o) affects the STOOIP. A reduction in B_o increases the STOOIP, while an increase in B_o reduces the STOOIP. The oil viscosity parameter is

a critical parameter for the mobility ratio and influence the time at water breakthrough and length of production plateau.

The multiplication factor for the oil viscosity is 10%. In contrast, the B_o uncertainty range is defined by adding -5% to +5% to the most likely value. A plot of B_o vs. reservoir pressure explains why the range of Bo requires a different definition. Oil compressibility is dependent on the angle between $B_o(P_{res} > P_{bp})$ and the horizontal axis. By subtracting or adding a percent to B_o relative to the reference case, the angle remains constant and yields an unchanged oil compressibility. Table 5.7 shows the range of B_o, oil viscosity and the equivalent mobility ratio. Figure 5.13 illustrates the effect of changing the mobility on fractional flow curves.

Table 5.7: Sensitivity range of oil viscosity and oil formation volume factor (B_o) at P_{bp}=196,6 bar and equivalent mobility ratio due to oil viscosity change.

Parameter	**Low**	**Mid**	**High**
Oil Viscosity (μ) ($*10\%$, $\div 10\%$)	0,49	0,44	0,40
Equivalent Mobility Ratio (-)	0,029	0,026	0,023
Bo (Rm^3/Sm^3) (+5%, -5%)	1,378	1,328	1,428

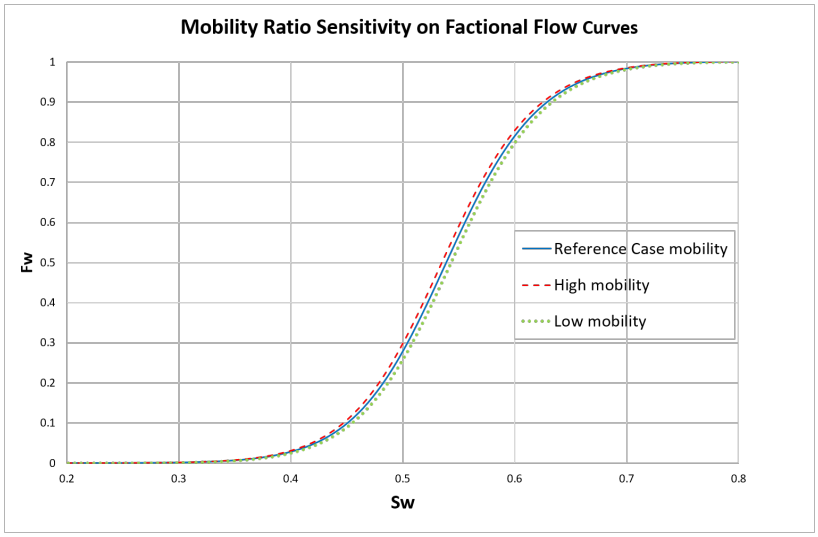

Figure 5.13: Resulting fractional flow curves from low case, reference case and high case mobility ratio.

Aquifer

The size and the properties of the numerical aquifer influences the pressure support from the aquifer. The aquifer sensitivity study includes one scenario without an aquifer and one scenario with a large aquifer relative to the reference aquifer. The factors controlling the aquifer are porosity and permeability. The scenario without an aquifer is controlled by zero porosity and the scenario with a large aquifer is controlled by average porosity of 25% and permeability of 100 mD. The change of porosity from 10% in the deterministic aquifer to 25% in the large aquifer increases the in-situ aquifer water volume with 150%. The next chapter contains a discussion about the selected sensitivity range for the aquifer.

Heterogeneity

The reservoir simulation model assumes that the measured permeability vs depth from well logs and core plugs extends throughout the reservoir. However, in the Alta west reservoir, the extent of parallel layers are highly uncertain since there are only two reservoir penetrations drilled 350 meters apart. In fact, the two well logs indicate variation in lamination as described in the introduction chapter.

Two sensitivity parameters are defined to reduce the influence from heterogeneities in the reservoir model: 1) constant horizontal permeability of 3, 10, 30 and 100 mD with k_v/k_h=0,01 and 2) Constant net permeability with 30 and 100 mD with k_v/k_h-ratio=0,05. The Constant net permeability parameter means that all grid cells with permeability above 3 mD is set to 30 mD in the Low case and 100 mD in the High Case.

Sensitivity Study Results

Gas Injection Strategy

The tornado chart in Figure 5.14 presents the cumulative oil production from the sensitivity study relative to reference case. There are clearly three factors dominating the influence on cumulative oil production when gas injection is applied. On top is the constant permeability, second is the constant net permeability and third is the perme-

ability multiplication factor. The tornado chart has a large spread of results; from the top with +180% when using constant permeability of 100 mD to the bottom of the chart with less than +/-10% when changing the values of either oil viscosity, relative permeability or B_o. The sensitivity study performed on the gas injection strategy indicates that permeability and heterogeneity are the most critical factors.

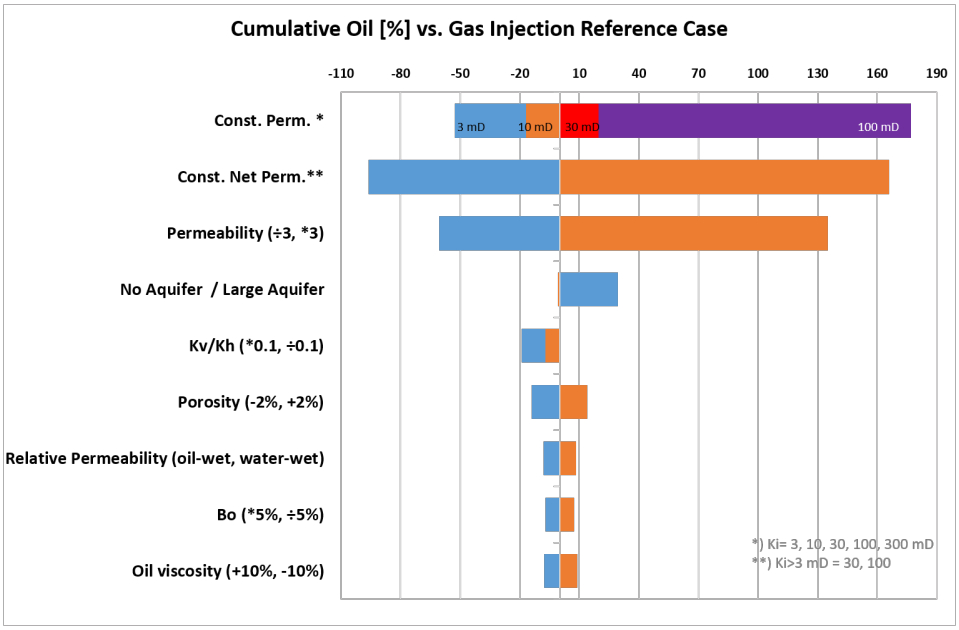

Figure 5.14: Tornado chart illustrating cumulative oil production sensitivities relative to the gas injection reference case at time when oil production is below 70 Sm^3/day.

Aquifer Support on Gas Injection

The tornado chart illustrates that the influence on cumulative oil production from simulations without aquifer and with large aquifer are +29% and -0.75% respectively. The results from aquifer modifications are illustrated in Figure 5.22 and 5.23. The results show that there is a small pressure drop when there is no aquifer connected to the reservoir. It can also be seen that the oil production rate is higher compared to the reference case (REF). The water-cut is also much lower, but the well shuts in after approximately 17 years because the liquid-gas rate exceeds the maximum ratio of 3000 Sm^3/Sm^3.

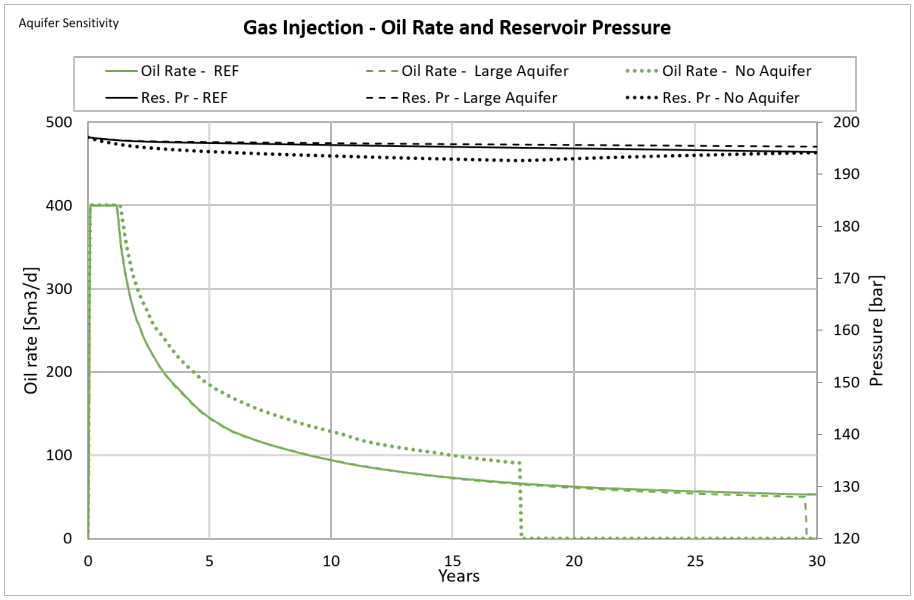

Figure 5.15: Gas injection sensitivity study: Illustrating aquifer support from reference aquifer (REF) large aquifer and no aquifer on oil production rate and reservoir pressure.

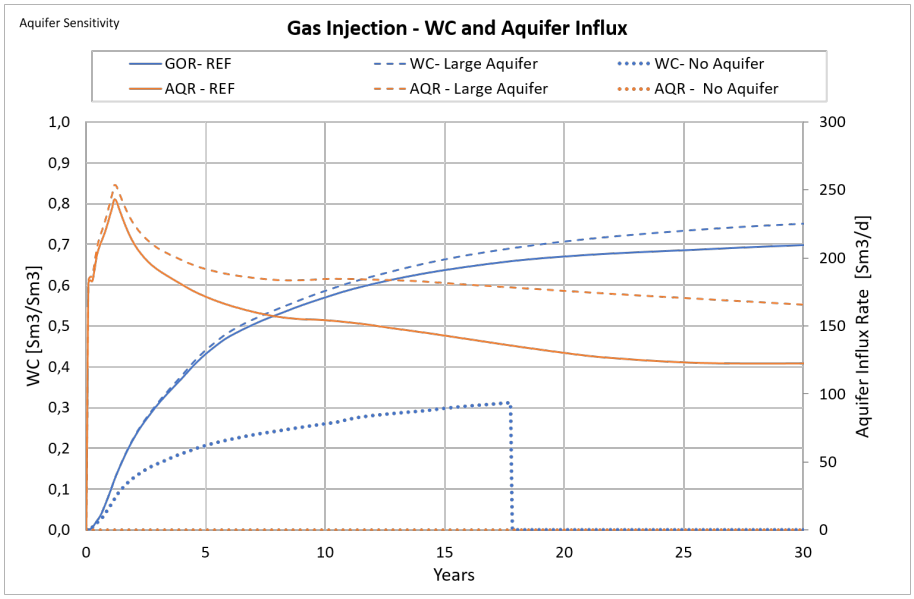

Figure 5.16: Gas injection sensitivity study: Illustrating aquifer support from reference aquifer (REF) large aquifer and no aquifer on water cut (WC) and aquifer influx rate (AQR).

Water Injection Strategy

Similar to the gas injection strategy, the two most influential parameters from the tornado chart in Figure 5.17 are constant net permeability and constant permeability. However, the influence is less significant with the greatest influence of -90% from constant net permeability of 30 mD. Notice that the scenario with constant permeability of 30 mD has positive influence relative to reference case in the gas injection strategy, but negative influence in the water injection strategy.

An interesting result is the effect of varying the permeability with the multiplication factor of 3. Both reducing the permeability and increasing the permeability by the factor of 3 results in negative effect on cumulative oil production. Figure 5.18 illustrates the results from permeability variations including water-cut and oil rate. The oil production plateau when using the high case permeability lasts longer compared to the reference case, but a rapid decrease in oil rate yields low cumulative oil production at time when economic oil rate is reached. Another observation from the simulation with high permeability is after 14 years of production when oil rate is 40 Sm^3/day, the production well is shut in because the water-cut exceeds the limit of 95%.

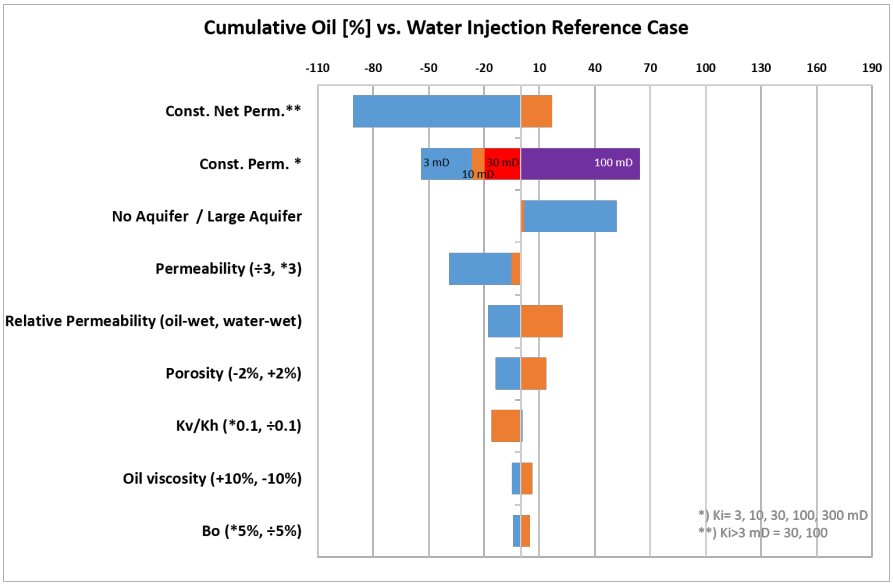

Figure 5.17: Tornado chart illustrating cumulative oil production sensitivities relative to the water injection reference case at time when oil production is below 70 Sm^3/day.

The sensitivity study performed on the water injection strategy supports the results from the gas injection sensitivity study that permeability and heterogeneity are critical factors. The study also indicates that the size of the aquifer and relative permeability are influential sensitivities.

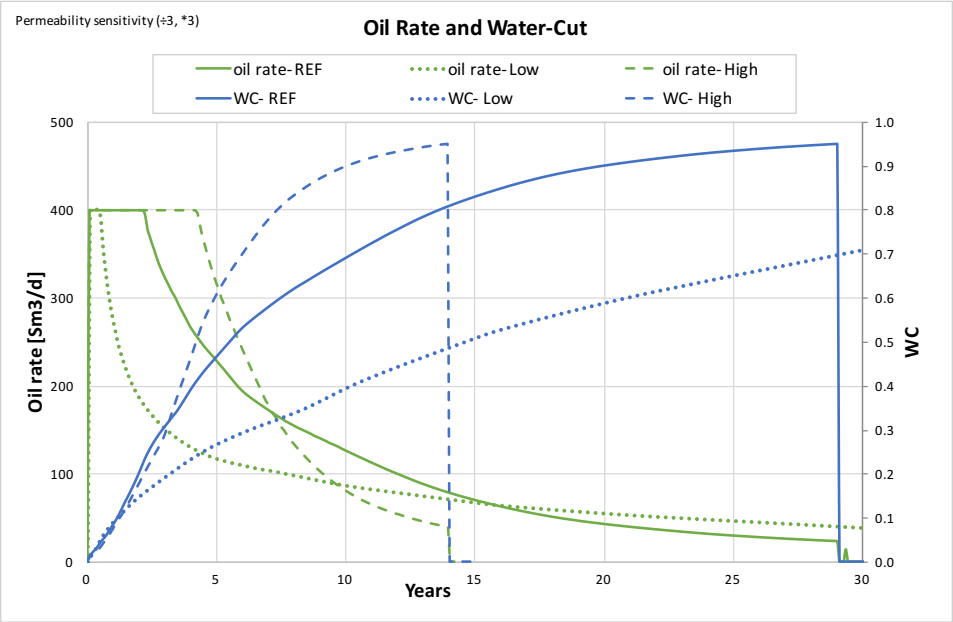

Figure 5.18: Water injection sensitivity study: Water Cut (WC) and oil production rate for high-, reference case- and low permeability.

Aquifer Support on Water Injection

The tornado chart in Figure 5.17 illustrates that the influence on cumulative oil production from simulations without aquifer and with large aquifer are +52% and +2% respectively. Figure 5.19 and 5.20 illustrate the simulation results from 30 years of production from modifications of the aquifer. The aquifer influx rate (AQR) is negative when there are an aquifer connected to the reservoir model indicating that the injected water is flowing to the aquifer pore volumes. The results from the simulation without aquifer shows that the production plateau last longer compared to the deterministic reference case and the resulting water-cut is significant lower.

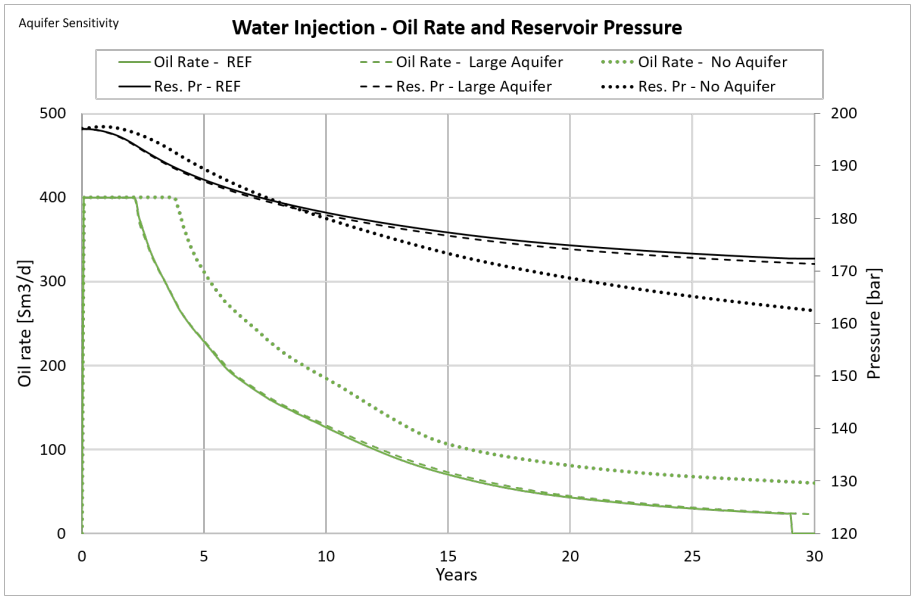

Figure 5.19: Water injection sensitivity study: Illustrating aquifer support from reference aquifer (REF), large aquifer and no aquifer on oil production rate and reservoir pressure.

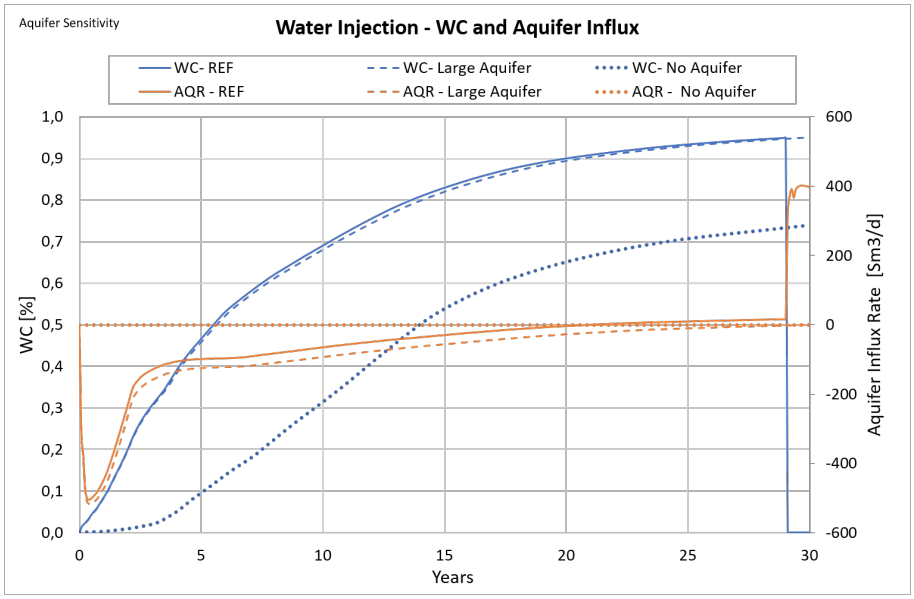

Figure 5.20: Water injection sensitivity study: Illustrating aquifer support from reference aquifer (REF), large aquifer and no aquifer on water cut (WC) and aquifer influx rate (AQR).

Pressure Depletion Strategy

The tornado chart in Figure 5.21 has similar influential parameters in the upper part of the chart, except the aquifer sensitivity. The scenario without an aquifer has +103% influence on cumulative oil production relative to the reference case and highlight the significance of the aquifer. Similar to the two other strategies, oil viscosity and B_o is at the bottom 3 least influential parameters.

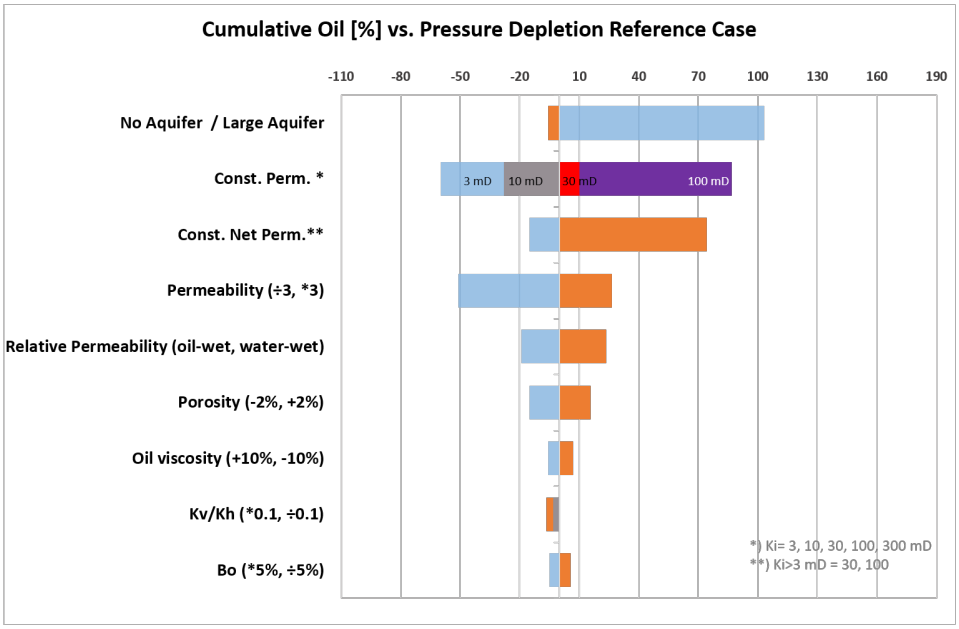

Figure 5.21: Tornado chart illustrating cumulative oil production sensitivities relative to pressure depletion reference case at time when oil production is below 70 Sm^3/day.

Aquifer Support on Pressure Depletion

The tornado chart in Figure 5.21 from pressure depletion illustrates that simulation without aquifer increases the cumulative oil production while simulation with larger aquifer results in reduced cumulative oil production. Without aquifer, the coning effects is reduced and the resulting water-cut (WC) is lower. The oil production plateau last longer, and the economic oil rate limit of 70 Sm^3/day is not reached after 30 years of production.

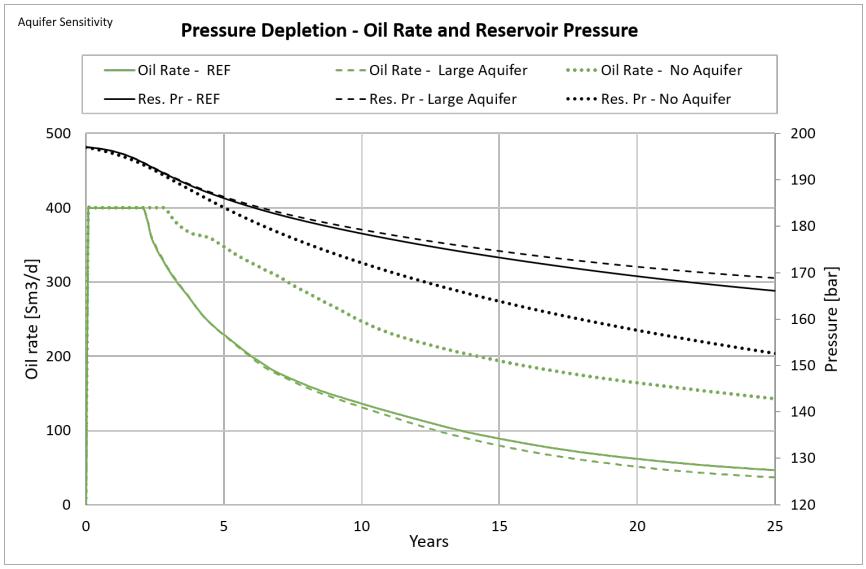

Figure 5.22: Pressure depletion sensitivity study: Illustrating aquifer support from reference aquifer (REF) large aquifer and no aquifer on oil production rate and reservoir pressure.

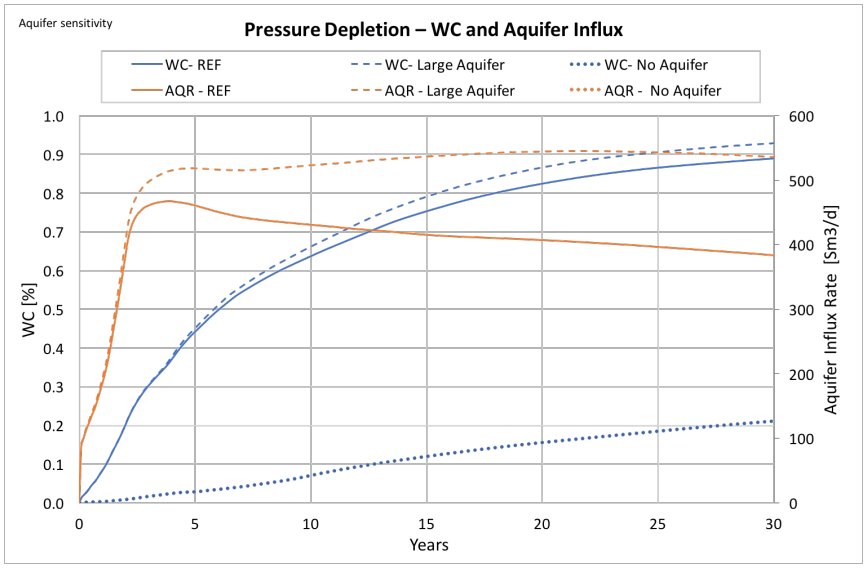

Figure 5.23: Pressure depletion sensitivity study: Illustrating aquifer support from reference aquifer (REF) large aquifer and no aquifer on water cut (WC) and aquifer influx rate (AQR).

5.3 Monte Carlo Uncertainty Risk Analysis

The Monte Carlo Simulation with the use of Latin Hypercube sampling performs the risk uncertainty analysis. The Monte Carlo Simulation consists of building a model of possible results by substituting a range of values from a probability distribution for any of the parameters that has an inherent uncertainty. Different sets of random values from each probability distribution are used to calculate the results and the user specifies the number of iterations. The Latin Hypercube sampling samples more accurately from the entire range of distributions compared to the Monte Carlo sampling (Palisade, 2018).

There are several common probability distributions and the Monte Carlo Simulation in this study includes three different distributions (Palisade, 2018):

- Uniform distribution where all values have an equal chance of occurring, and the user simply defines the minimum and maximum value
- Pert distribution where the user defines the minimum, most likely and maximum values. The values around the most likely are more likely to occur
- Discrete distribution where the user defines a number of specific values that may occur and the likelihood of each

100 different combinations of input values are sampled by using the @Risk function in Excel. The sampled values from @Risk are included in Petrel where the simulation cases are defined and simulated by Eclipse. Seven parameters listed in Table 5.8 are considered to have inherent uncertainty based on the sensitivity study in the previous section. Figure 5.24 illustrates the probability distributions defined by Table 5.8 for each of the seven parameters. Since B_o and oil viscosity have minor influence on the oil recovery, they are not included in the uncertainty risk analysis. The constant permeability is also excluded because a complete homogeneous reservoir is considered unrealistic.

The relative permeability distribution is discrete and each value is assigned a likelihood to occur. The discrete value represent the relative permeability curves from Figure 5.10

and 5.12 in Section 4 where 1 is the low/oil-wet curve, 2 is the reference case curve and 3 is the high/water-wet curve.

The constant net permeable is divided into 4 discrete numbers; 10, 30, 100 and 0. The first three numbers is the constant net permeability value for the grid blocks with permeability higher than 3 mD. The last number, 0, means that constant net permeability option is not included in the reservoir model, and the grid block permeability is determined by the permeability multiplier. It is 70% probability that the constant net permeability parameter is not included.

Table 5.8: Parameters included in the uncertainty risk analysis performed by using Monte Carlo Simulations.

Uncertainty Parameters	**Min/Low**	**Most Likely**	**Max/High**		**Distribution Type**
Permeability Multilpier	0,33	1	3		Pert
Porosity	-0,02		0,02		Uniform
Relative Permeability*	1	2	3		Discrete
Rel. Perm. Probability	0,25	0,5	0,25		
Kv/Kh Multiplier	0,1	1	10		Pert
Aquifer Porosity Range	0	0,13	0,15		Pert
Aquifer Permeability Range	10	40	300		Pert
Constant Net Permeability**	10	30	100	0	Discrete
Const. Net Perm. Probability	0,01	0,14	0,15	0,7	
*) Sampling of curves from Figure 5.10 and 5.12. 1= oil-wet, 2=reference case, 3=water-wet					
**) 10, 40, 300 = Grid block permeability (mD) for grid blocks with mD>3. 0=No cons. net perm.					

Table 5.9 shows the dependencies of the parameters were 0 is no dependency and 1 is full positive dependency. Negative dependencies ranging from 0 to -1 can also be defined, but was not applied for any of the parameters in this thesis. In general, parameter dependency of 0.9 is strong dependency and 0,6 is weak dependency. For example, if a high value from the porosity range is randomly picked, it is 90% probability that the value from the permeability range is equally high. The resulting sampled values generated from @Risk is dependent on the sensitivity ranges listed Table 5.8 and their dependencies in Table 5.9.

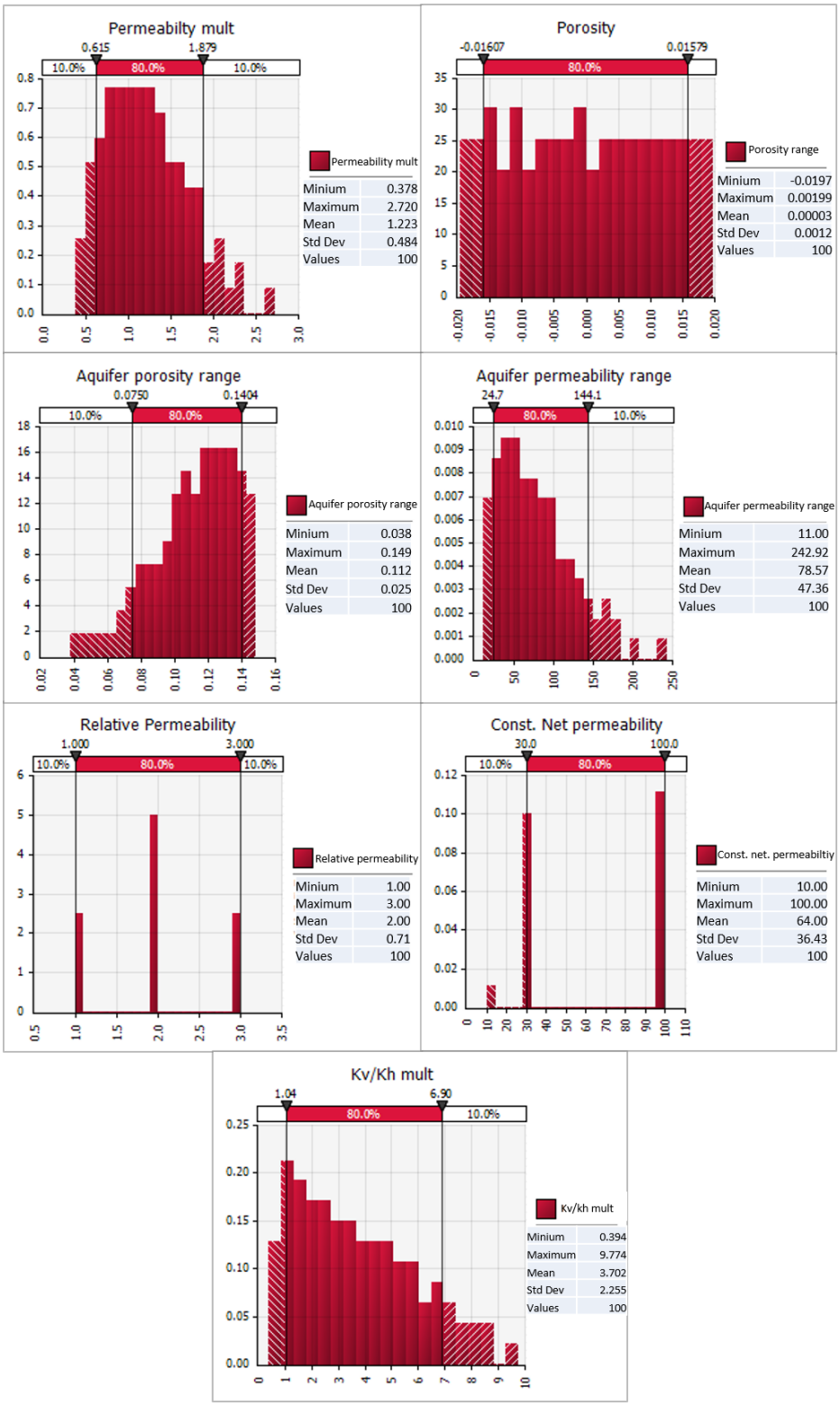

Figure 5.24: Probability distributions for the seven parameters included in the Monte Carlo Simulation.

Table 5.9: Parameter dependencies for the parameters included in the Monte Carlo Simulations.

@Risk Correlctions	Perm. Mult	Poro.	Rel. Perm.	Kv/Kh Mult	Aquifer Poro.	Aquifer Perm.	Const. Net Perm.
Perm. Mult	1						
Poro.	0,9	1					
Rel. Perm.	0	0	1				
Kv/Kh Mult	0	0,6	0	1			
Aquifer Poro	0	0	0	0	1		
Aquifer Perm.	0,9	0	0	0	0,9	1	
Const. Net Perm.	0	0	0	0	0	0	1

5.4 Petrel Uncertainty Simulation Results

The results from the 100 simulations per development strategy after 30 years of production are presented in the following figures. All simulations are constrained by the same well control limits applied in the sensitivity study, except that the production well shuts in after oil rate is below 70 Sm^3/day. The range of uncertainty of the potentially recoverable volumes are provided a low, best, and high estimate such that:

- P90 (low case) means that 90% of the calculated estimates will be equal or exceed the P90 estimate
- P50 (median case) means that 50% of the calculated estimates will be equal or exceed the P50 estimate
- P10 (high case) means that 10% of the calculated estimates will be equal or exceed the P10 estimate

A mean case is also included in the results representing the mean potentially recoverable volume from the 100 simulations.

Cumulative Oil Production Uncertainty Range

Figure 5.25, 5.26 and 5.27 represent the uncertainty span of cumulative oil production from the three development strategies. The gas injection strategy has the largest uncertainty span with highest P10 case and lowest P90 case. The significant deviation between P50 and reference case is affected by the optimistic P90 case and its influence

makes P50 higher in the gas injection strategy compared to the water injection strategy even though the reference case for the water injection strategy is higher.

The water injection strategy has the smallest uncertainty span. The cumulative oil production curves of P10, P50 and P90 stabilize in an early stage of the production and indicate that the oil production rates approach 70 Sm^3/day.

The pressure depletion strategy has the highest P50 model. Table 5.10 shows the final oil recovery factors and discounted oil rates after 30 years of production for the different models.

Table 5.10: Final oil recovery and discounted oil rate from the Monte Carlo Uncertainty Simulations.

Strategy:	**Gas Injection**	**Water Injection**	**Pressure Depletion**
	Recovery Factor (%)		
P90	0,17	0,21	0,25
P50	0,29	0,28	0,35
P10	0,54	0,38	0,50
Reference Case	0,23	0,30	0,33
	Discounted Oil Rate (MSm^3)		
P90	0,42	0,54	0,59
P50	0,61	0,68	0,73
P10	0,86	0,83	0,92
Reference Case	0,52	0,70	0,70

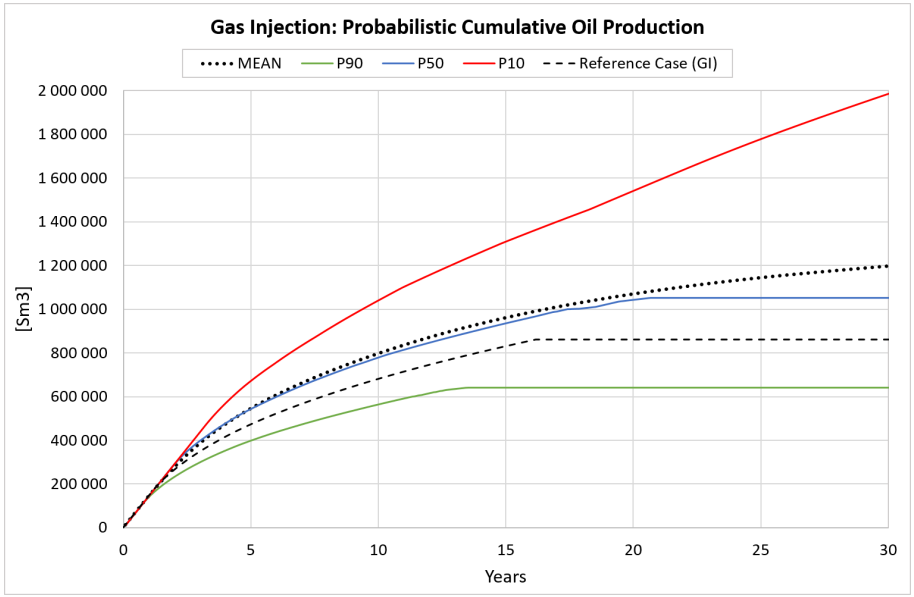

Figure 5.25: Probabilistic uncertainty study - cumulative oil production. Illustrating P10, P50, P90, Mean and reference case to the gas injection strategy.

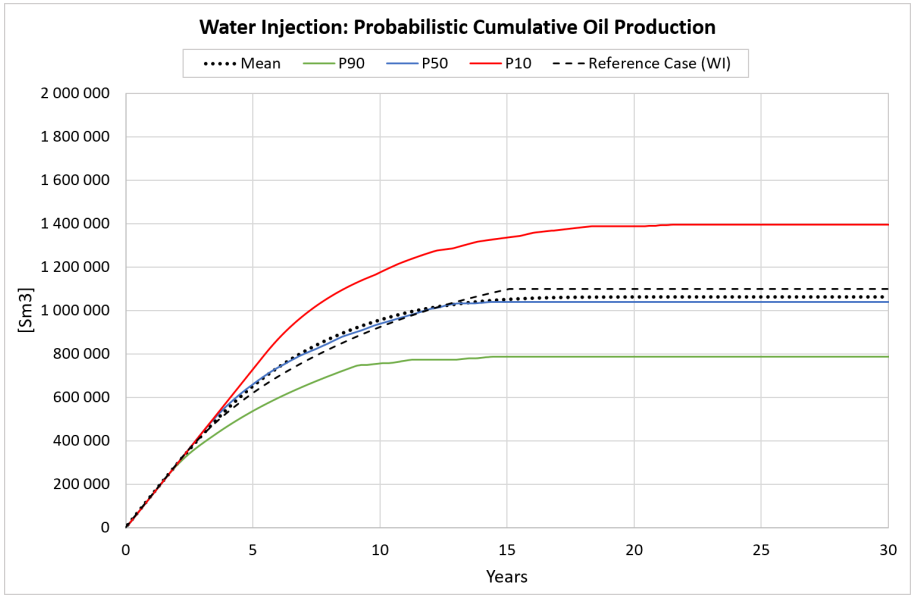

Figure 5.26: Probabilistic uncertainty study - cumulative oil production. Illustrating P10, P50, P90, Mean and reference case to the water injection strategy.

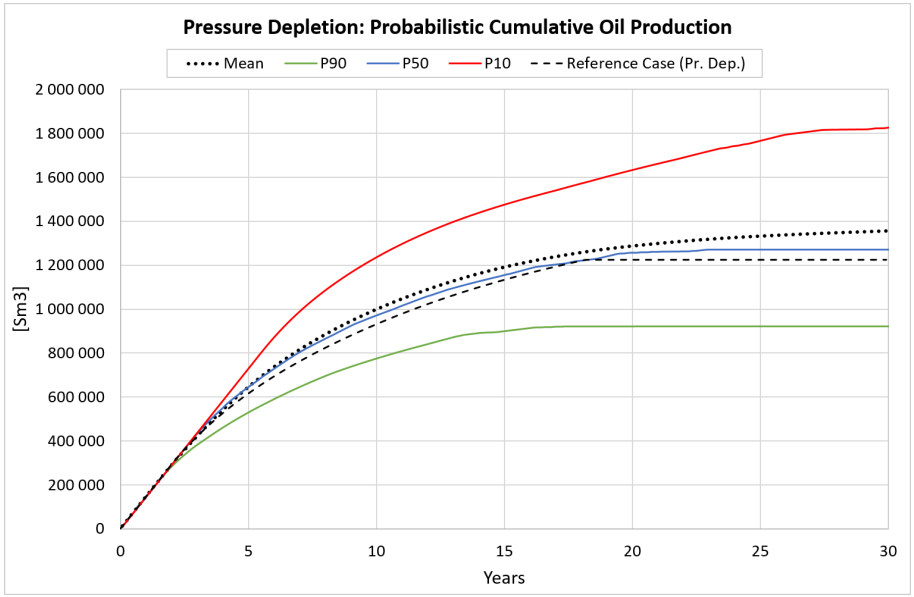

Figure 5.27: Probabilistic uncertainty study - cumulative oil production. Illustrating P10, P50, P90, Mean and reference case to the pressure depletion strategy.

Oil Production Rate Uncertainty Range.

Figure 5.28, 5.29 and 5.30 illustrate the uncertainty range in oil production rate from the different development strategies. The results clearly show that the oil production plateau in the P10, P50 and P90 models are shortest in the gas injection strategy. The length of the plateaus are more similar for the two other strategies.

On the other hand, the slope of the oil production rates from the water injection models in Figure 5.29 are steeper and results in shorter production periods. Consequently, the oil recovery for P50 and P10 models are lowest in the water injection strategy. However, the longer oil production plateau when using water injection results in higher discounted oil rate compared to gas injection.

Notice that the P90 models from gas injection and pressure depletion do not reach the economic limit of 70 Sm^3/day. The high oil production rate toward the end of production for the P90 model for the gas injection is the reason why this model has the highest oil recovery of 54 %. Again, the long oil production plateau from the pressure depletion

strategy, as illustrated in Figure 5.30, has great influence on the discounted oil production. It makes pressure depletion strategy favorable based on this parameter.

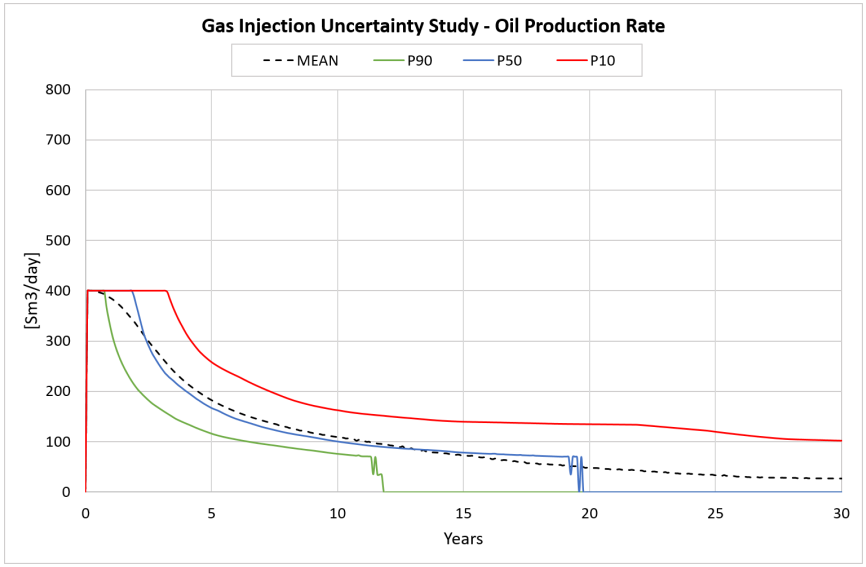

Figure 5.28: Probabilistic uncertainty study - oil production rate. Illustrating P10, P50 and P90 for the gas injection strategy.

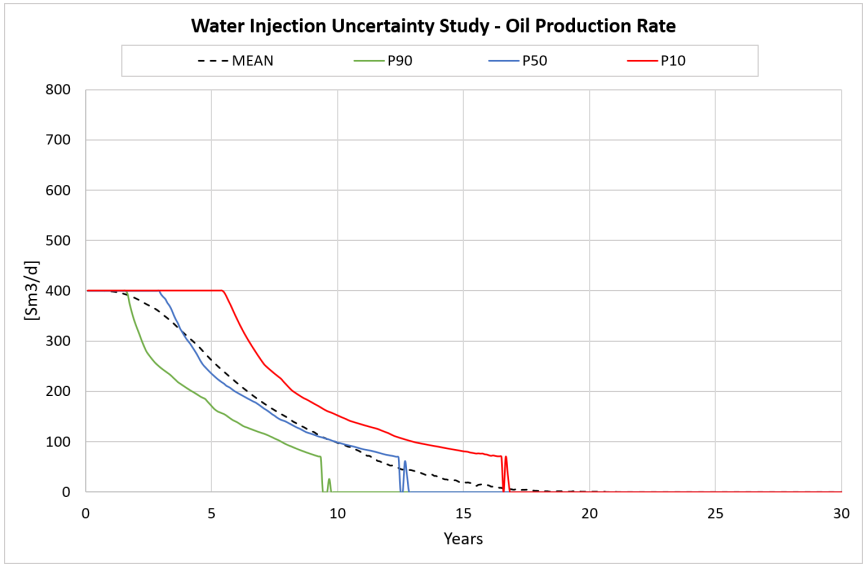

Figure 5.29: Probabilistic uncertainty study - oil production rate. Illustrating P10, P50 and P90 for the water injection strategy.

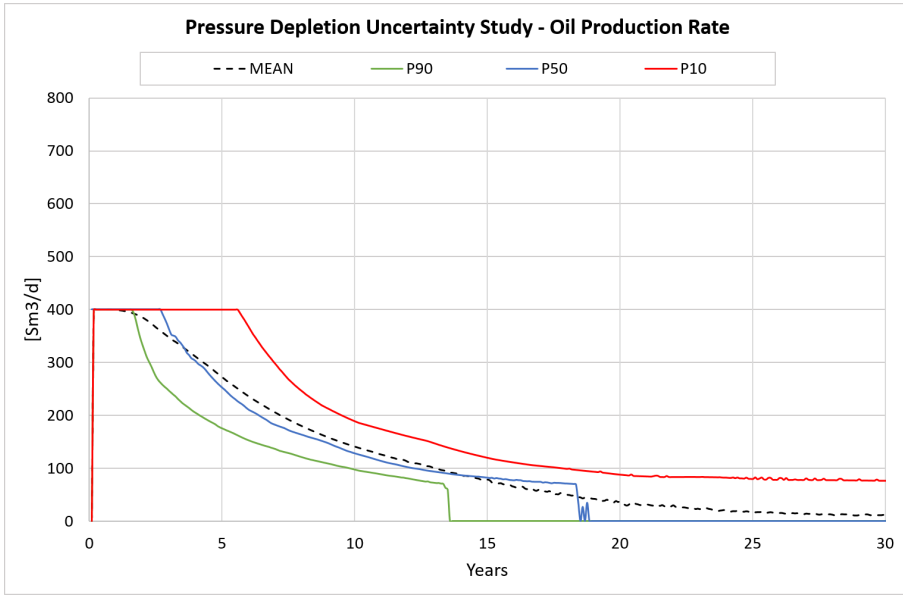

Figure 5.30: Probabilistic uncertainty study - oil production rate. Illustrating P10, P50 and P90 for the pressure depletion strategy.

Water Production Rate Uncertainty Range

The liquid rate production limit is set to 800 Sm^3/day with maximum water cut of 95%. The water production profiles illustrated in Figure 5.31, 5.32 and 5.33 from the uncertainty simulations do not have significant variations. The P50 model for the water injection strategy has maximum water rate slightly higher than 400 Sm^3/day while gas injection and pressure depletion have maximum water rate between 300 and 400 Sm^3/day. The P10 model for water injection illustrates that the water injection strategy is occasionally limited by maximum water-cut. The increasing slope of the water production rate is somewhat steeper for the water injection models, but approach zero in early production due to well control and economic limits.

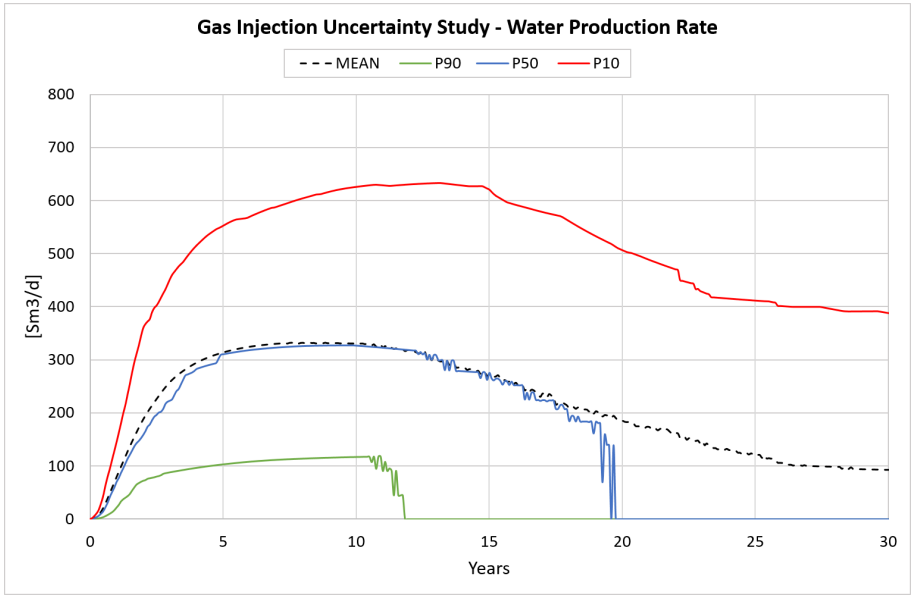

Figure 5.31: Probabilistic uncertainty study - water production rate. Illustrating P10, P50 and P90 for the gas injection strategy.

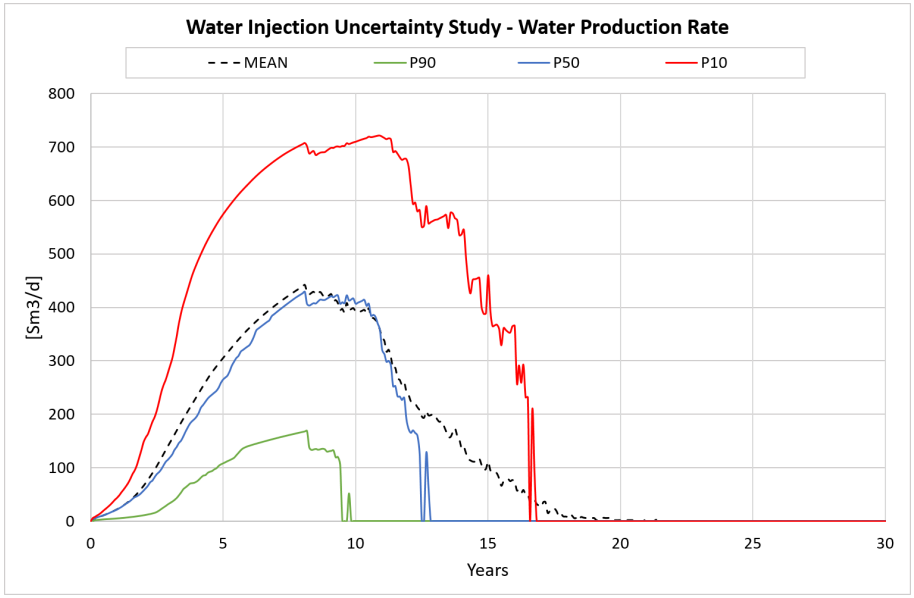

Figure 5.32: Probabilistic uncertainty study - water production rate. Illustrating P10, P50 and P90 for the water injection strategy.

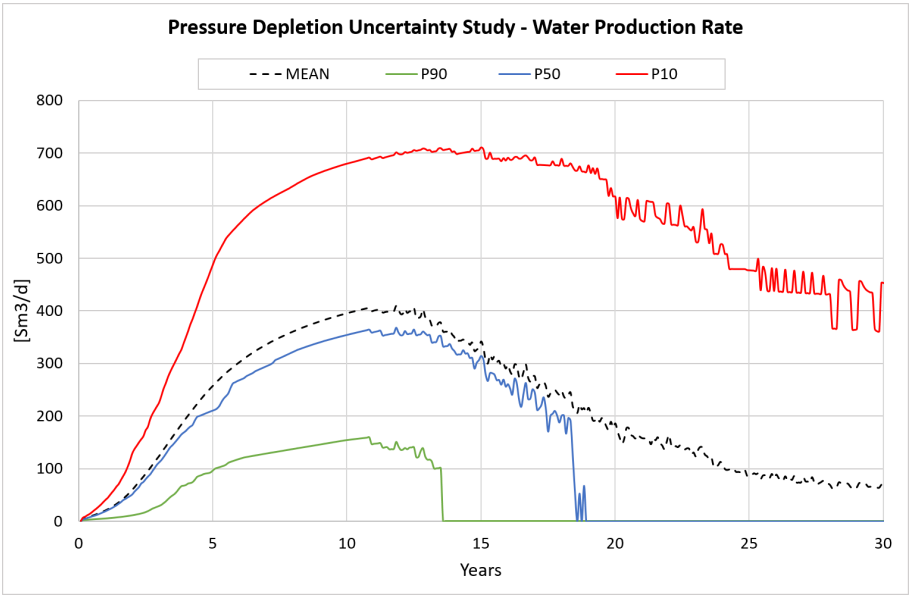

Figure 5.33: Probabilistic uncertainty study - water production rate. Illustrating P10, P50 and P90 for the pressure depletion strategy.

Gas Production Rate Uncertainty Range

Figure 5.34, 5.35 and 5.36 illustrate the uncertainty range in gas production rate. There are great differences in gas production rates between the development strategies. Water injection and pressure depletion has a rapid increase from start of production with maximum gas rate in early production before it drops and decrease until end of production. The uncertainty models for the gas injection strategy do not have a steep slope in the beginning of the production. Instead, a stable increase with time is observed. However, neither of the gas production profiles for the gas injection strategy reach the maximum gas rate of 1 000 000 Sm^3/day.

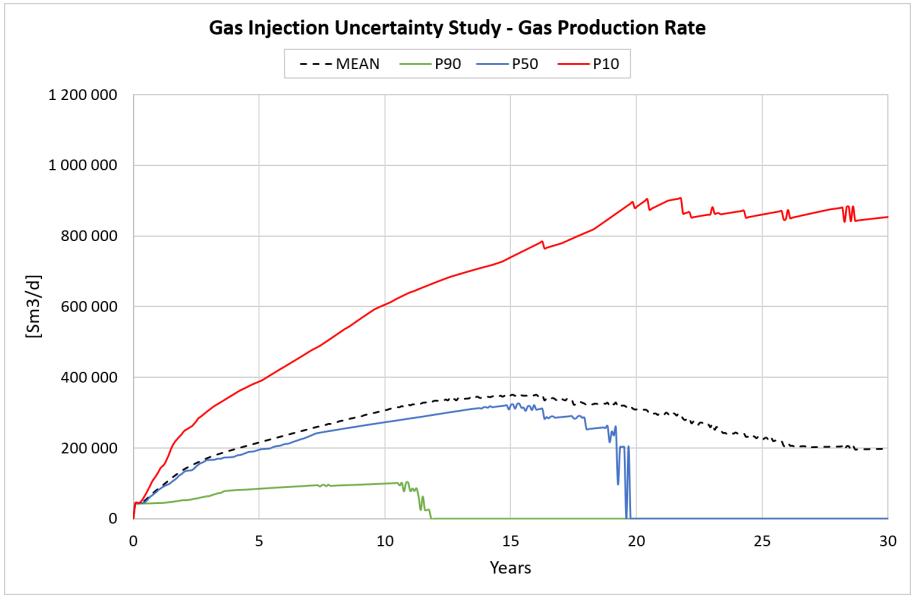

Figure 5.34: Probabilistic uncertainty study - gas production rate. Illustrating P10, P50 and P90 for the gas injection strategy.

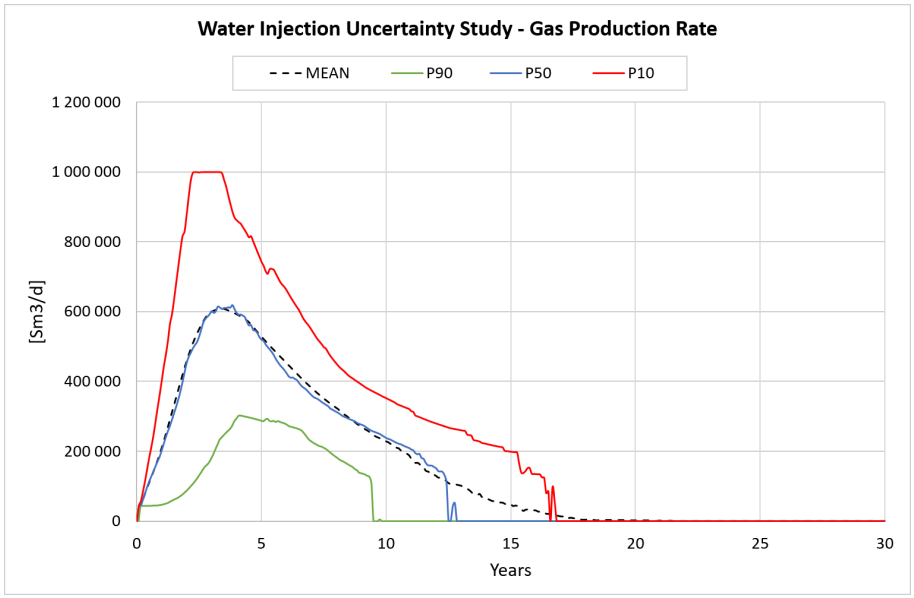

Figure 5.35: Probabilistic uncertainty study - gas production rate. Illustrating P10, P50 and P90 for the water injection strategy.

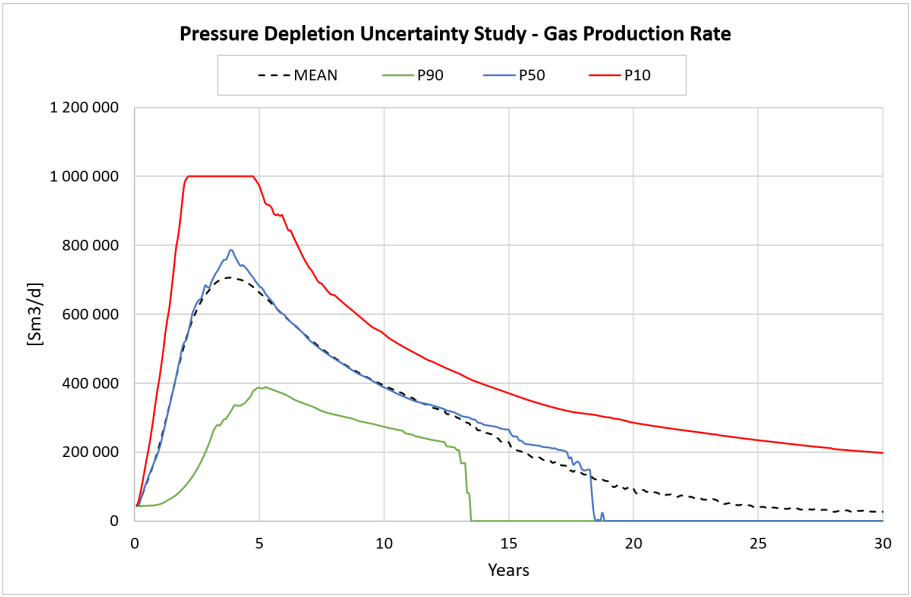

Figure 5.36: Probabilistic uncertainty study - gas production rate. Illustrating P10, P50 and P90 for the pressure depletion strategy.

Chapter 6

Discussion

Prior to the uncertainty risk analysis conducted in this study, gas injection was predicted to be the most efficient recovery method for the Alta West reservoir. In general, gas injection is applied to improve the vertical sweep efficiency and consequently increase the oil recovery. However, the simulation results from the uncertainty analysis imply the opposite effect. Surprisingly, when either gas injection or water injection is applied to the reservoir model, less oil is produced. In the following chapter, the reason for why the pressure depletion strategy provides best recovery are discussed and whether other factors such as gas handling and economic aspects support the results from the uncertainty risk analysis.

6.1 Main Observations

Sensitivity Study:

- The most influential parameters are permeability and the degree of reservoir heterogeneity, studied by constant and constant net permeability
- Aquifer sensitivities has greatest influence on the pressure depletion strategy
- Porosity, relative permeability and kv/kh-ratio have minor effects on cumulative oil production and is not the main focus in the uncertainty evaluation

- Formation volume factor (B_o) has insignificant influence on cumulative oil production for the three development strategies. They are therefore not included in the Monte Carlo uncertainty simulations

Monte Carlo Uncertainty Simulations

- The pressure depletion strategy has, according to the uncertainty analysis, the highest P50 oil recovery
- The gas injection strategy has the largest uncertainty span in cumulative oil production. The great influence from the high permeability case provides a better P50 model relative to the deterministic reference case
- The gas injection strategy has the best P10 model with highest oil recovery factor. On the other hand, the long oil production plateau for the pressure depletion strategy, makes the discounted oil rate higher relative to the gas injection strategy
- The water injection strategy is sensitive to water-cut well control limit. In addition, the water injection uncertainty models have the shortest production periods mainly because of the economic oil production limit

Stability of the Gas Front

A critical factor contributing to less efficient displacement by gas injection can be explained by the stability of the gas front. Because of the low permeability and great vertical permeability variations in the Alta West reservoir, the stability of the gas (and water) front is sensitive to production and injection rates.

It has been illustrated that variations in oil rate has great influence on the oil production plateau when gas injection is applied. Almost identical production plateaus are also observed when various oil rates are tested on water injection and pressure depletion. The resulting P50 models from the uncertainty simulations illustrate that the length of the oil production plateau for gas, water and pressure depletion last for only 1.9, 3.1 and 2.7 years respectively. When oil rates exceed 400 Sm^3 the oil production plateaus are not present, indicating unstable gas front displacement. "High" oil rates lead to viscous

fingering in the high permeability layer. In addition, the high permeability layer has a small pore volume, which enhances the significance of fingering. Gravity segregation will not occur when viscous forces dominates, which results in poor sweep efficiency.

The gas injection strategy has shorter oil production plateau compared to the other strategies partly because of the gas injection rate and partly because of the low pressure drop. The pressure plot in Figure 5.8 illustrates that the highest reduction in reservoir pressure occurs in the pressure depletion strategy and lowest in the gas injection strategy. The volume of injected gas prevent the pressure to decline and it reduces the displacement of oil by solution gas drive and gas-cap drive. The short oil production plateau and the fact that gas production rate increases with time indicates that a significant amount of free gas is produced. These factors support the evaluation in this thesis that gas injection contributes to viscous instabilities.

There are factors suggesting that solution gas drive and gas-cap drive are dominating drive mechanisms in the water injection and pressure depletion strategies. This can be illustrated by their gas production rates, gas-oil ratios and reservoir pressure. The rapid increase in oil rate after start of production, when reservoir pressure decreases, indicates solution gas drive. This type of reservoir behavior contributes to longer oil production plateau. The stabilized gas-oil ratio, compared to the increasing gas-oil ratio for the gas injection strategy, indicates an expanding gas-cap due to gravity segregation. Gravity segregation contribute to higher oil rates and extends the lifetime of the production well. Figure 6.1 illustrates the distinct gas rates and gas-oil ratios from the three strategies. The simulation results are from the deterministic reference cases. The pressure drop can be seen in the previous chapter in Figure 5.8.

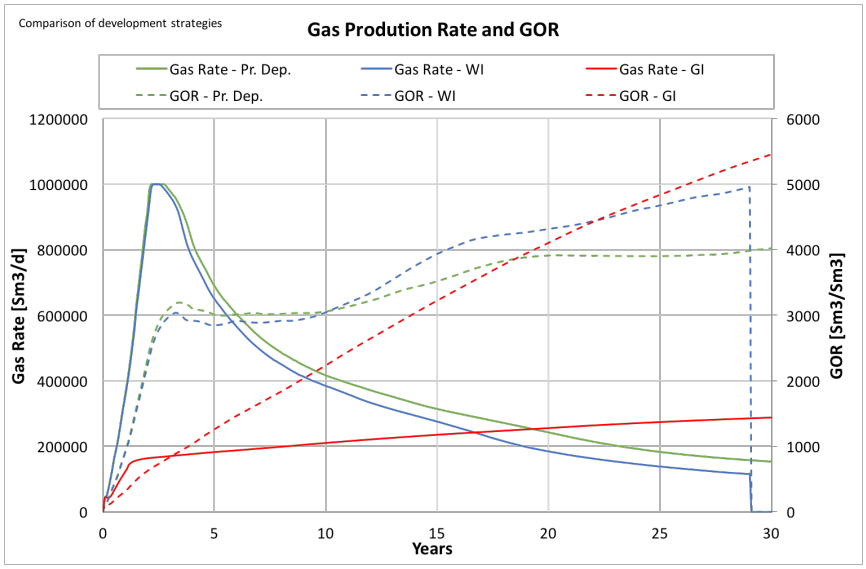

Figure 6.1: Comparing gas production rates and gas-oil ratios (GOR) between the gas injection (GI.), water injection (WI) and pressure depletion (Pr. Dep.) strategies. The results are from the reference cases

The sudden increase in gas rate can also be related to operational sensitivities. The location of the production well when using water injection and pressure depletion are closer to the gas-cap. See the well locations in Figure 4.12 in Chapter 4. Earlier gas breakthrough may occur when the well is closer to the gas zone. An investigation on gas inflow rate for each well connection is therefore conducted. It was observed that inflow rate for both production wells was clearly dominated by a few well connections, all located in the high permeability layer. Because of this observation, the significant difference between the production rates at start of production is most likely not dominated by operational sensitivity.

Table 5.4 from the previous chapter shows that the cumulative solution gas production is greatest in the water injection and pressure depletion strategies. The solution gas-oil ratio (R_{so}) decreases and more oil is liberated at the same time as GOR stabilizes. It is therefore reasonable to believe that solution gas drive and gas-cap drive are dominating drive mechanisms. In contrast, the increasing GOR and nearly constant R_{so} when gas injection is applied indicate that the majority of the produced gas is free gas.

The evaluation from the uncertainty risk analysis may indicate that the initial gas-cap has sufficient energy to produce oil for a long period without additional gas injection. The results suggest that the application of gas injection may reduce oil displacement by gas-cap drive. On the other hand, if reservoir heterogeneties are less severe and permeability higher than the most likely value, gas injection may be the optimal development strategy with greatest displacement efficiency.

Water Coning and Aquifer Support

An interesting observation is the variations in aquifer influx rate and the effects of the aquifers on cumulative oil production. The aquifer influx rate in Figure 5.20 when using water injection is negative when an aquifer is connected to the reservoir model. This is because a numerical aquifer has a defined volume and compressibility. Water can flow from the injector to the aquifer if the pressure in the injector is higher than the aquifer pressure. The aquifer pressure will increase according to the material balance.

Table 6.1 summarizes the results from the aquifer sensitivity and presents the influence on cumulative oil production relative to the reference cases for each development strategy.

Table 6.1: Aquifer sensitivity results: Illustrating influence on cumulative oil production relative to the reference case for each development strategy

	Gas Injection	**Water Injection**	**Pressure Depletion**
No Aquifer	28%	52%	103%
Large Aquifer	-0.75%	2%	-6%

Table 6.1 illustrates that the effects from no aquifer are less significant for the gas injection strategy. It is related to the reservoir pressure drop and fluid compressibility. Gas compressibility is much larger relative to oil and water compressibilities. High reservoir pressure is achieved when the reservoir contains a great amount of gas, which can occur when gas is injected in the reservoir. The expansion of the aquifer, and hence the aquifer influx, starts once the pressure decline has travelled to the entire or partially

throughout the aquifer's volume. Low pressure drop caused by high gas compressibility is therefore one reason why the gas injection strategy is less affected by the aquifer sensitivity.

In theory, water injection is applied to increase the oil recovery. Nevertheless, it is not the case for the reservoir model studied in this thesis. One factor contributing to less efficient oil recovery by water injection is water coning.

The water-cut is considerable reduced for the three development strategies when there are no aquifer connected to the reservoir model. It implies that the oil production is sensitive to water coning. However, the effect of coning increases when additional water is injected into the water zone. Water injection contributes to higher water saturation near the wellbore and consequently reduces the oil relative permeability near the wellbore. These factors support the evaluation from the uncertainty study that the pressure depletion strategy has better sweep efficiency than the water injection strategy.

Operational sensitivities can also contribute to water coning. In general, water breakthrough occurs earlier in a production well closer to the water zone. However, the production well for the gas injection strategy is placed 10 meter closer to the water zone compared to production well for the two other strategies. Consequently, operational sensitivities are not likely the reason why the oil production for the gas injection strategy is less affected by water coning.

The influence from larger aquifer on cumulative oil production relative to the deterministic aquifer are almost insignificant. The porosity was increased from 10% to 25%, which increases the water volume in the aquifer with 150%. However, the bulk volume was not increased in the sensitivity study and since aquifer compressibility is the sum of water and rock compressibility, this may be the reason why there are only minor effects from the larger aquifer.

6.2 Field Development

In the previous section main focus were given to the effect on oil recovery due to parameters uncertainty and various recovery methods of the Alta West reservoir. However, for the Alta West and Alta East reservoirs to have economic viability, other factors of the production must be considered. The focus in this section is given to water and gas handling that is produced, and implications this might have for the chosen development strategy or other aspects of the field development process.

It is important to consider the whole lifetime production-behavior of a reservoir in planning phase, as the project will be profitable during the production decline period. Figure 6.2 illustrates the cumulative cash flow and the oil production vs. time. Development planning and production are usually based on the expected production profile, which is highly dependent on the drive mechanisms in the reservoir. The production profile will determine the required facilities and number of wells to be drilled (Fanchi et al., 2008).

It is important to include the Alta East reservoir behavior in the decision of optimal recovery method, as Alta East is the reservoir with highest potential and best reservoir quality. At present time, the work on the Alta Discovery is still at the development phase and a decision to continue the project is not yet decided. However, the main focus in this study was not to include the Alta East reservoir in the recommendation of optimal recovery method in Alta West. Therefore, only a brief summary of the influence from Alta East will be included in the evaluation.

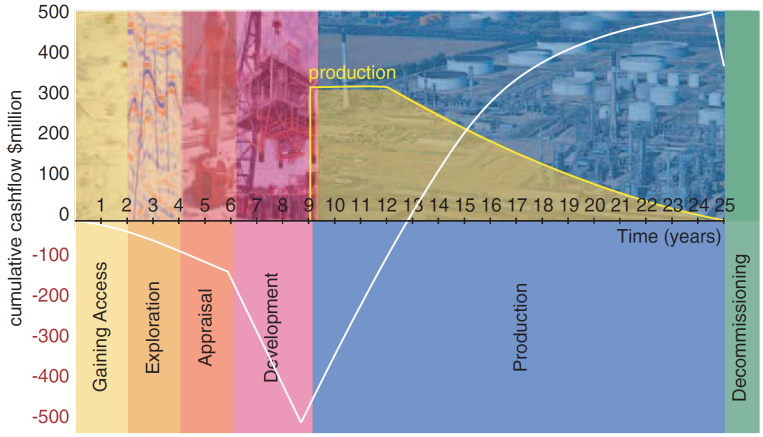

Figure 6.2: The field life cycle and cumulative cash flow. Figure from Fanchi et al. (2008)

Gas Handling

Considerable high gas rates are produced in the evaluated reservoir model. The gas rate limit is set to 1 million Sm^3/day and several of the simulated cases is constrained by this limit. High producing gas-oil ratios will increase the size and cost of gas-handling equipment, in particular compression (Bothamley, 2004). Either the produced gas can be transported through pipelines to shore, where it can be sold, or it can be injected into another reservoir, or re-injected into the Alta West reservoir.

Additional revenue to the Alta project is possible if the produced gas are to be sold. However, this is dependent on the infrastructure in the Barents Sea. The Snøhvit Field, located 35 km south of the Alta Discovery, is the first major development on the Norwegian continental shelf with no surface installations. The subsea installation transports gas to land through a 143-kilometre pipeline (Equinor, 2018). To connect the pipelines from the Alta Discovery via the Snøhvit Field may be an option.

The work done on the Alta East by Lundin Norway AS suggests that gas injection is the optimal recovery method. This is also supported by Bjerga (2017) in her master thesis about the Alta East fractured carbonates. If gas injection is applied to the Alta East, a potential for re-injection of the produced gas from the Alta West is possible.

For the development strategies studied, maximum gas rates varies from start of production to end of production. The gas injection strategies has an increasing gas rate almost until end of production, meaning operational costs related to gas handling increases with time. In contrast, the gas production rates in the water injection and pressure depletion strategy reach maximum rate at an early stage of production and experience a rapid decreases after end of oil production plateau, indicating that operational costs related to gas handling may decrease with time.

The pressure communication between Alta East and Alta West must be included in the discussion of gas handling. The simulation results from the uncertainty study indicates that the reservoir is sensitive to viscous instabilities and gas coning. If the development strategy on Alta East reservoir includes gas injection, there is a possibility that the injected gas contribute to viscous fingering and increased gas production to the Alta West reservoir.

Water Handling

For the three development strategies studied, water handling is not a significant part of the planning phase. The maximum liquid rate for the production well is 800 Sm^3/day, which is low relative to other production rates on the Norwegian continental shelf. In the sensitivity study conducted on the Alta East reservoir by Bjerga (2017), water production rates differ from 9000 to 21000 Sm^3/day when water injection was applied in the simulation model.

The water production profiles for the different development strategies, illustrated in Figure 5.31, 5.32 and 5.33, imply that the water rates have minor variations. Problems to water production are closer related to water coning, described in section 6.1. Water coning is mainly influenced by water injection and aquifer support for the Alta West simulation model. The size of the aquifer and its pressure support is highly uncertain, but there is no doubt that there is an underlying aquifer in the Alta West reservoir. It means that water coning due to aquifer influx should be considered.

In addition, well injectors are expensive to drill. Water injection, based on the uncertainty risk analysis, may lead to poor sweep efficiency and evaluation of this study suggests that water injection may not be the optimal recovery method for the Alta West reservoir.

6.3 Recommendations for Further Work

Some comments about further work are discussed in this chapter. This section is a brief summary of suggested improvements to the evaluation of recovery mechanisms in the Alta West reservoir:

- The aquifer size and its influence as a drive mechanism should be studied closer. The aquifer sensitivity study illustrates minor effects between the reference aquifer and the large aquifer. A question should be raised whether the numerical reference aquifer is modeled too large, or if the large aquifer's change in pore volume and/or aquifer bulk volume is too small
- Investigate initial water saturation and capillary pressure sensitivities. If water salutation is made dependent on change in capillary pressure curve, permeability and porosity, the simulation model will be more realistic. Since initial water saturation and capillary pressure are assumed constant, the only parameter affecting the STOOIP is porosity
- Investigate the behavior and sensitivities of the different reservoir facies. This can provide better understanding of reservoir heterogeneity and its influence on recovery mechanisms
- Hysteresis is not included in simulations, meaning that drainage and imbibition processes follow the same path of saturation change for both capillary pressure and relative permeability curves. Its effect on oil production should be studied
- Wettability variations should also be considered through capillary pressure curves, and not only through relative permeability curves

Chapter 7

Conclusions

Typical drive mechanisms in clastic oil reservoirs have been studied in literature and tested with the Eclipse Black Oil Simulator. Primary focus is given to characterize the dominating drive mechanisms in the reservoir and evaluate three development strategies: gas injection, water injection and pressure depletion. An evaluation of optimal recovery method is based on an uncertainty risk analysis performed by using Monte Carlo Simulations. The main discoveries of this study are:

- Horizontal production well is optimal compared to vertical well. The optimal depth of the horizontal well depends on the chosen displacement method
- Water coning and gas coning are not influenced by the horizontal well depth (within the range of depth studied in this thesis)
- The two most influential parameters are permeability and degree of reservoir heterogeneity, in particular on the gas injection strategy. If the permeability is low and there are great contrasts in vertical permeability, gas front instabilities are severe and the sweep efficiency is poor
- The size of the aquifer is the third most influential parameter. Aquifer influx, together with water injection, enhance the significance of water coning
- The oil production is sensitive to water coning. Negative effects on cumulative oil production are observed when an aquifer is connected to the reservoir model

and when using water injection

- The dominating drive mechanisms are considered gas solution drive and gas-cap drive. The effects of these drive mechanisms are reduced when gas injection is applied to the model
- The optimal recovery method, solely based on the uncertainty risk analyses, is the pressure depletion strategy. The gas-cap displacement efficiency shows potential for high oil recovery without additional water- or gas injection
- If future work on the Alta West discovery identify higher permeability and minor lateral extension of tight reservoir layers, gas injection may provide better displacement efficiency
- Investigations regarding pressure communication between Alta East and Alta West should be included in further work to obtain better understanding of the gas handling implications

References

Abdallah, W., Buckley, J. S., Carnegie, A., Edwards, J., Herold, B., Fordham, E., Graue, A., Habashy, T., and Selznev, N. (2007). Fundamentals of wettability. *Oilfield Review*, 19(2):44–61.

Ayan, C., Colley, N., Cowan, G., Ezekwe, E., Wannell, M., Goode, P., Halford, F., Joseph, J., Mongini, A., Obondoko, G., and Pop, J. (1994). Measuring permeability anisotropy: The latest approach. *Oilfield Review*, 6(4):24–35.

Behrenbruch, P. and Goda, H. M. (2005). Two-phase relative permeability prediction: A comparison of the modified brooks- corey methodology with a new carman-kozeny based flow formulation. *SPE Asia Pacific Oil Gas Conference and Exhibition*.

Bjerga, T. (2017). Recovery Mechanisms in Naturally Fractured Carbonate Reservoirs: A Case Study of the Barents Sea Alta Discovery using Dual Porosity Model Simulations. Master's thesis, Norwegian University of Science and Technology, Trondheim.

Bothamley, M. (2004). Offshore processing options vary widely. *Oil and Gas Journal*.

Braun, E. and Holland, R. (1995). Relative permeability hysteresis: Laboratory measurements and a conceptual model. *SPE Reservoir Engineering*, 10(3):222 – 228.

Brooks, R. H. and Corey, A. T. (1996). Properrties of porous media affecting fluid flow. *Irrigation and Drainage Division*.

Buckley, J. S. (1998). Wetting alteration of solid surfaces by crude oils and their asphaltenes. *Oil Gas Science and Technology*, 53(2):303–312.

Dake, L. P. (1978). Fundamentals of reservoir engineering. In *Developments in petroleum science*, volume 8. Elsevier, Amsterdam, 1 edition.

Dake, L. P. (1994). The practice of reservoir engineering. In *Developments in petroleum science*, volume 36. Elsevier, Amsterdam, 1 edition.

Dunlap, H., Garrouch, A., and Sharma, M. M. (1991). Effects of wettability, pore geometry, and stress on electrical conduction in fluid-saturated rocks. *The Log Analyst*, 32(5):511–526.

Equinor (2018). Snøhvit. `https://www.equinor.com/en/what-we-do/norwegian-continental-shelf-platforms/snohvit.html`.

Fanchi, J. (2000). Integrated flow modeling. In *Developments in Petroleum Science*, volume 49. Elsevier, Amsterdam, 1 edition.

Fanchi, J., Cook, M., and Graham, M. (2008). Hydrocarbon exploration and production. In *Developments in Petroleum Science*, volume 55. Elsevier, Amsterdam, 2 edition.

Fazlija, M. (2016). Petrophysical properties on core plugs from alta ii, wells 7220/11-2 and 7220/11-2a. Confidential report, Weatherford Laboratories.

Henriksen, E., bjørnseth, H. M., Hals, T. K., Heide, T., Kiryukhina, T., Kløvjan, O. S., Larsen, G. B., Ryseth, A. E., Rønning, K., Sollid, K., and Stoupakova, A. (2011). Uplift and erosion of the greater barents sea: impact on prospectivity and petroleum systems. In *Arctic Petroleum Geology (Memoirs)*, volume 35, page 271–281. Geological Society, London.

King, H. M. (2018). Fluorescent minerals. `https://geology.com/articles/fluorescent-minerals/`.

Kleppe, J. (2017a). Lecture notes tpg4150 - buckley-leverett analysis (hand-out note no. 4). Retrieved from http://www.ipt.ntnu.no/ kleppe/TPG4150/BL.pdf.

Kleppe, J. (2017b). Lecture notes tpg4150 - material balance equations (hand-out note no. 1). Retrieved from http://www.ipt.ntnu.no/ kleppe/TPG4150/matbal.pdf.

Lander, R. H. and Bonnell, L. M. (2010). A model for fibrous illite nucleation and growth in sandstones. *AAPG Bulletin*, 94,(8):1161–1187.

Leverett, M. (1941). Capillary behavior in porous solids. *Transactions of the AIME*, 142(01):152 – 169.

Lomeland, F., Ebeltoft, E., and Thomas, W. H. (2005). A new versatile relative permeability correlation. *SPE Asia Pacific Oil Gas Conference and Exhibition*.

McPhee, C., Reed, J., and Zubizarreta, I. (2015). Core analysis a best practice guide. In *Developments in petroleum science*, volume 64. Elsevier, Amsterdam, 2 edition.

Palisade (2018). Monte carlo simulation. `http://www.palisade.com/risk/monte_carlo_simulation.asp`.

Petrowiki (2015a). Displacement efficiency of immiscible gas injection. `http://petrowiki.org/Displacement_efficiency_of_immiscible_gas_injection`.

Petrowiki (2015b). Solution gas drive reservoirs. `http://petrowiki.org/Solution_gas_drive_reservoirs`.

Schlumberger (2015a). *Eclipse Reference Manual*, 2015.2 edition.

Schlumberger (2015b). *Eclipse Technical Description*, 2015.2 edition.

Schlumberger (2018a). Mdt modular formation dynamics tester. `https://www.slb.com/services/characterization/reservoir/wireline/modular_formation_dynamics_tester.aspx`.

Schlumberger (2018b). Petrel reservoir engineering. `https://www.software.slb.com/products/petrel/petrel-reservoir-engineering`.

Schön, J. (2015). Physical properties of rocks. In *Developments in petroleum science*, volume 65. Elsevier, Amsterdam, 2 edition.

Tijink, P. (2018). Saturation modeling and endpoint scaling. MMbbls Limited AS presentation.

Yuan, Y. and Lee, T. R. (2013). Contact angle and wetting properties. In *Surface Science Techniques*, volume 51. Springer-Verlag Berlin Heidelberg, Berlin, 1 edition.

Appendix A

Symbols Used in Material Balance Equation

B_g Formation volume factor for gas (res.vol./st.vol.)

B_o Formation volume factor for oil (res.vol./st.vol.)

B_w Formation volume factor for water (res.vol./st.vol.)

C_r Pore compressibility (pressure^{-1})

C_w Water compressibility (pressure^{-1})

ΔP $P_2 - P_1$

G_i Cumulative gas injected (st.vol.)

m Initial gas cap size (res.vol. of gas cap)/(res.vol. of oil zone)

N Original oil in place (st.vol.)

N_p Cumulative oil produced (st.vol.)

P Pressure

R_{so} Solution gas-oil ratio (st.vol. gas/st.vol. oil)

R_p Cumulative producing gas-oil ratio (st.vol./st.vol)

S_g Gas saturation

S_w Water saturation

S_o Oil Saturation

W_e Cumulative aquifer influx (st.vol.)

W_i Cumulative water injected (st.vol.)

W_p Cumulative water produced (st.vol.)

ρ density

ϕ Porosity

Appendix B

Petrel Work-Flow for Water Saturation Modelling

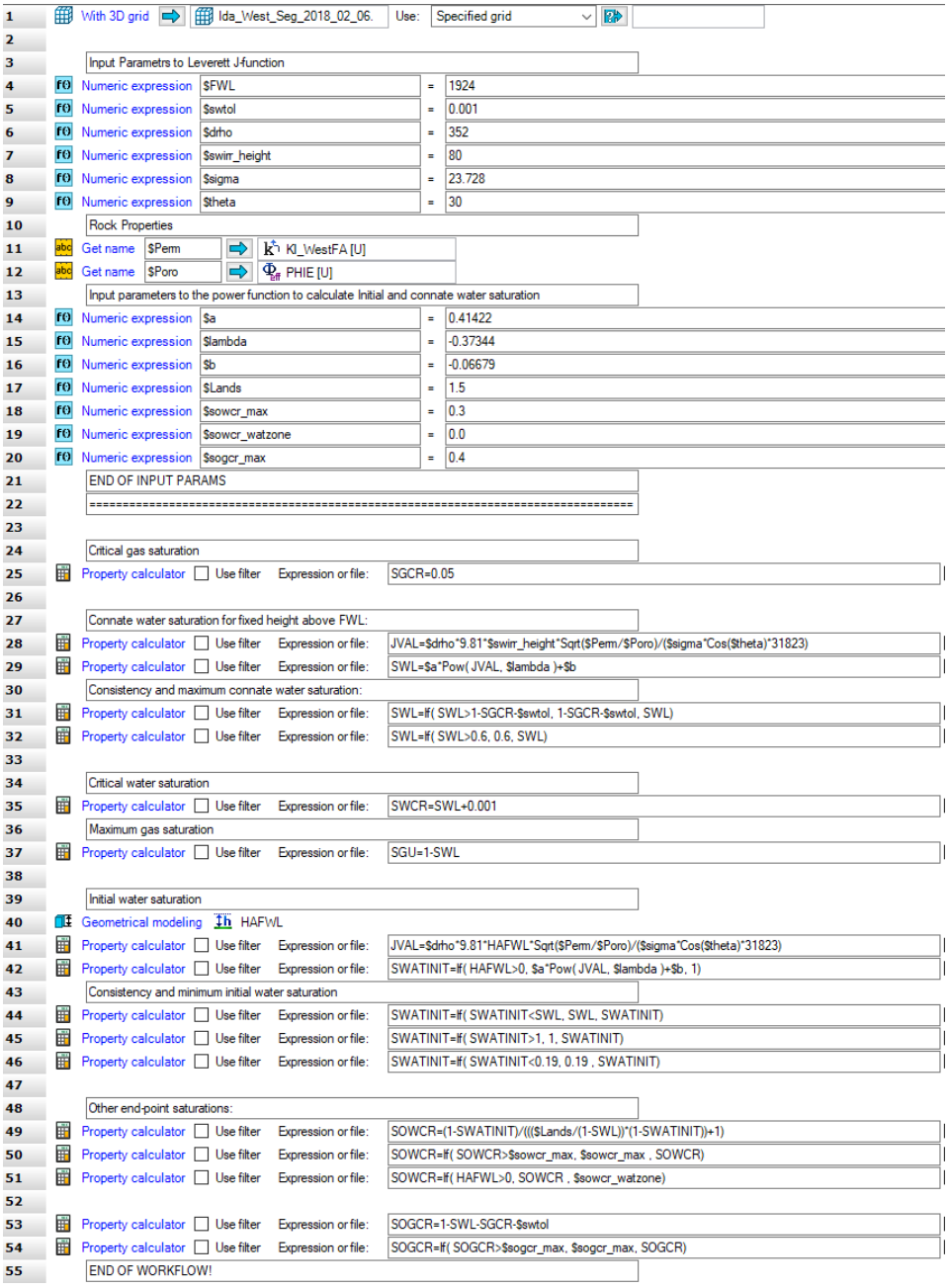

Figure B.1: Petrel water saturation modelling